National Library of Canada
Canadian Theses Service
Ottawa, Canada
K1A 0N4

Bibliothèque nationale du Canada
Services des thèses canadiennes

CANADIAN THESES

THÈSES CANADIENNES

NOTICE

The quality of this microfiche is heavily dependent upon the quality of the original thesis submitted for microfilming. Every effort has been made to ensure the highest quality of reproduction possible.

If pages are missing, contact the university which granted the degree.

Some pages may have indistinct print especially if the original pages were typed with a poor typewriter ribbon or if the university sent us an inferior photocopy.

Previously copyrighted materials (journal articles, published tests, etc.) are not filmed.

Reproduction in full or in part of this film is governed by the Canadian Copyright Act, R.S.C. 1970, c. C-30.

AVIS

La qualité de cette microfiche dépend grandement de la qualité de la thèse soumise au microfilmage. Nous avons tout fait pour assurer une qualité supérieure de reproduction.

S'il manque des pages, veuillez communiquer avec l'université qui a conféré le grade.

La qualité d'impression de certaines pages peut laisser à désirer, surtout si les pages originales ont été dactylographiées à l'aide d'un ruban usé ou si l'université nous a fait parvenir une photocopie de qualité inférieure.

Les documents qui font déjà l'objet d'un droit d'auteur (articles de revue, examens publiés, etc.) ne sont pas microfilmés.

La reproduction, même partielle, de ce microfilm est soumise à la Loi canadienne sur le droit d'auteur, SRC 1970, c. C-30.

THIS DISSERTATION
HAS BEEN MICROFILMED
EXACTLY AS RECEIVED

LA THÈSE A ÉTÉ
MICROFILMÉE TELLE QUE
NOUS L'AVONS REÇUE

Canada

NL-339 (r.86/06)

THE UNIVERSITY OF ALBERTA

THEORY OF PHOTODESORPTION BY RESONANT LASER-VIBRATIONAL COUPLING

BY

PETER PIERCY

©

A THESIS

SUBMITTED TO THE FACULTY OF GRADUATE STUDIES AND RESEARCH

IN PARTIAL FULFILMENT OF THE REQUIREMENTS FOR THE DEGREE

OF DOCTOR OF PHILOSOPHY

IN THEORETICAL PHYSICS

DEPARTMENT OF PHYSICS

EDMONTON, ALBERTA

(Fall, 1986)

Permission has been granted to the National Library of Canada to microfilm this thesis and to lend or sell copies of the film.

The author (copyright owner) has reserved other publication rights, and neither the thesis nor extensive extracts from it may be printed or otherwise reproduced without his/her written permission.

L'autorisation a été accordée à la Bibliothèque nationale du Canada de microfilmer cette thèse et de prêter ou de vendre des exemplaires du film.

L'auteur (titulaire du droit d'auteur) se réserve les autres droits de publication; ni la thèse ni de longs extraits de celle-ci ne doivent être imprimés ou autrement reproduits sans son autorisation écrite.

ISBN 0-315-32454-6

THE UNIVERSITY OF ALBERTA

RELEASE FORM

NAME OF AUTHOR: Peter Piercy

TITLE OF THESIS: Theory of Photodesorption by Resonant Laser-Vibrational Coupling

DEGREE: Ph. D.

YEAR THIS DEGREE GRANTED: 1986

Permission is hereby granted to THE UNIVERSITY OF ALBERTA LIBRARY to reproduce single copies of this thesis and to lend or sell such copies for private, scholarly or scientific research purposes only.

The author reserves other publication rights, and neither the thesis nor extensive extracts from it may be printed or otherwise reproduced without the author's written permission.

Peter Piercy

PERMANENT ADDRESS:

14 Kaymar Dr.

Ottawa, Ontario

K1J 7C9

Date: April 23, 1986

THE UNIVERSITY OF ALBERTA

FACULTY OF GRADUATE STUDIES AND RESEARCH

The undersigned certify that they have read, and recommend to the Faculty of Graduate Studies and Research for acceptance, a thesis entitled "THEORY OF PHOTODESORPTION BY RESONANT LASER-VIBRATIONAL COUPLING" submitted by PETER PIERCY in partial fulfilment of the requirements for the degree of Doctor of Philosophy.

.....
(Supervisor)

.....

.....

.....

.....

.....

Date: April 23, 1986

Abstract

Photodesorption may be initiated by resonant, laser-induced excitation of an internal vibrational mode of an adsorbed molecule. Via molecule-selective couplings and/or resonant surface heating, desorption may then proceed. The photodesorption kinetics are predicted from a quantum statistical theory based on a master equation describing incoherent phonon- and photon-assisted molecular transitions as well as elastic tunnelling processes. Explicit contributions to desorption by coherent two phonon/photon absorption and emission, lateral vibrational energy transfer between adsorbed molecules, and by the resonant heat flux at the surface, are derived.

Photodesorption rates are calculated for the adsorption systems CH_3F on NaCℓ, pyridine on KCℓ, NH_3 on Cu, CO on Cu, and CO on NaCℓ, and are found in general to depend non-linearly on both laser intensity and on initial substrate temperature. The predicted lineshape of the photodesorption yield can differ from the corresponding infrared absorption spectrum due to nonlinear intensity effects, vibrational anharmonicity, and surface heterogeneity.

Qualitative agreement with experimental trends is found. Finally, selective and non-selective photodesorption mechanisms are compared, and implications for further experiments and theories are discussed.

Acknowledgments

This thesis would certainly have been inconceivable without the direction and assistance of my supervisors, Drs. H. J. Kreuzer and Z. W. Gortel. Specifically, Dr. Kreuzer is thanked for suggesting the main problems and providing the theoretical model on which this thesis is based, and for his assistance in the final preparation of the manuscript. Dr. Gortel's instruction throughout the course of this project, and his calculations which form the basis of Sections 2 and 3, I gratefully acknowledge. In addition, the numerics were done expertly by Bob Teshima.

I wish to thank Dr. B. L. Clarke for pointing out to me the methods used in Section 2.5.2, and Drs. H. Umezawa and H. Matsumoto for discussion of their theory of Thermo Field Dynamics which is applied in Section 5.

The hospitality of the Physics Department at Dalhousie University, Halifax, I have greatly appreciated during my visits there.

Finally, the financial (scholarship) support of the Natural Sciences and Engineering Research Council and the Alberta Heritage Scholarship fund is acknowledged.

Table of Contents

	Page
1. Introduction	1
2. Theory of Basic Photodesorption Model	11
2.1 Introduction	11
2.2 The Hamiltonian of the Gas-Solid-Laser System	15
2.2.1 The static Hamiltonian	16
2.2.2 The electromagnetic field	19
2.2.3 Dynamics of the solid - phonons	27
2.2.4 The complete Hamiltonian	29
2.3 The Master Equation	31
2.4 The Transition Rates in Lowest Order Perturbation Theory	36
2.4.1 Laser-assisted vibrational transitions	38
2.4.2 The phonon interaction	40
2.4.3 Tunneling to the gas phase	45
2.5 Solution of the Master Equation	47
2.5.1 Direct numerical solution	47
2.5.2 Approximate analytic solution	50
2.6 Early Results - Theory and Experiment	62
2.6.1 Theoretical model results	62
2.6.2 Comparison with experimental results	68
3. Resonant Heating	70
3.1 Introduction	70
3.2 Theory	73
3.2.1 Exact solution	76
3.2.2 Approximate solution	82
3.3 Comparison with Experimental Results	90
4. Lateral Vibrational Energy Transfer	101
4.1 Introduction	101
4.2 Resonant V-V Transitions	108
4.3 Macroscopic Energy Flow	111
4.4 Microscopic V-V Transfer in Photodesorption	115
4.4.1 Harmonic vibrational mode	121

4.4.2 Anharmonic vibrational mode 122
4.5 Discussion 126
5. Coherent Two-Quanta Processes 128
5.1 Introduction 128
5.2 Formulation of the Transition Rate Calculation 130
5.2.1 Transition rate formula 131
5.2.2 Description of the reservoirs by the theory of Thermo Field Dynamics 134
5.2.3 Perturbation expansion of the transition rates 139
5.2.4 Bound state resonances in the two-quanta transition rates 153
5.3 Coherent Two-Phonon Transitions 156
5.4 Coherent Two-Photon Transitions 167
5.5 Coherent One-Photon Plus One-Phonon Transitions 172
5.6 Effect of Coherent Two-Quanta Processes on the Desorption Kinetics 175
6. Theory of the Photodesorption Line Shapes 182
6.1 Introduction 182
6.2 Homogeneous Adsorbate 183
6.3 Effect of Vibrational Anharmonicity 187
6.4 Inhomogeneous Adsorbate 193
6.5 Discussion 198
7. Discussion and Outlook 201
7.1 Selective Photodesorption versus Resonant Heating 201
7.2 Conclusions 208
References 213
Appendix A - Normal Modes of the Radiation Field 220
Appendix B - Morse Potential Matrix Elements 222
Appendix C - V-V Coupling Rate Matrix Elements 224
Appendix D - Diagram Rules and Derivation of (5.38) 226
Appendix E - Components of Equation (5.73) 231

List of Tables

Table		Page
4.1	Resonant V-V transfer and vibrational decay constants, and V-V diffusion length	110
7.1	Adsorption system parameters	204
7.2	Selective photodesorption versus resonant heating	207
D.1	Interaction Hamiltonian	228
D.2	Vertex functions	229

List of Figures

Figure		Page
1.1	Possible channels to desorption.	3
1.2	Resonant photodesorption yields for CH_3F/NaCℓ at 77K, from reference 22.	6
2.1	The interaction process.	12
2.2	(a) Energy diagram of gas molecule states.	13
	(b) Two possible paths to desorption.	
2.3	Adsorbate molecule configuration.	16
2.4	Electromagnetic fields at a metal surface.	23
2.5	(a) Some direction diagrams for the ground state	55
	(b) Diagrams for (j, v_{max})	55
	(c) Relating n_j^v to $n_{j'}^{v+1}$	56
2.6	Energy level diagram for CH_3F/NaCℓ.	64
2.7	Desorption rate versus laser intensity for CH_3F/NaCℓ.	65
2.8	Desorption rate versus inverse temperature for CH_3F/NaCℓ.	66
3.1	Resonant surface heating pathways.	72
3.2	Resonant heating cycle.	73
3.3	Time dependence of coverage for CH_3F/NaCℓ.	80
3.4	Relative change in surface temperature with time.	81
3.5	Temperature profile into the solid at high intensity.	82
3.6	Photodesorption yields of NH_3 adsorbed on Cu(100) as a function of laser frequency.	91
3.7	Photodesorption yields of NH_3/Cu(100) as a function of laser fluence.	92
3.8	Selective photodesorption rates for NH_3/Cu(100) as a function of laser intensity for T = 90 and 150K.	93
3.9	Desorption rate versus laser fluence for NH_3/Cu(100).	95
3.10	Maximum surface temperature rise.	96
4.1	Possible vibrational transfer processes between molecules.	102
4.2	Comparison of molecule in matrix and at surface.	104
4.3	The photodesorption mechanism of Fain and Lin.	106
4.4	Photodesorption rate as a function of V-V transfer rate.	124
5.1	Interaction processes due to H_{int}	142

5.2 Transition amplitudes containing one or two real phonons or photons..... 144
5.3 Irreducible vertices and the self energy correction..... 146
5.4 Green's functions for adsorbed molecule..... 149
5.5 Approximate transition amplitudes..... 154
5.6 Photodesorption rate versus laser intensity for CH_3F/NaCℓ for different adsorption energies..... 178
5.7 Bound state energy levels for adsorbed CH_3F/NaCℓ..... 180
5.8 Photodesorption rate as a function of laser intensity for reduced surface potential range..... 181
6.1 Photodesorption rate as a function of laser frequency for CH_3F on NaCℓ at sub-saturation intensity..... 185
6.2 Photodesorption lineshape calculated with coherent two-quanta processes included..... 187
6.3 Desorption rate versus laser intensity for CH_3F/NaCℓ, including vibrational anharmonicity..... 190
6.4 Photodesorption lineshape for CH_3F/NaCℓ, including vibrational anharmonicity..... 191
6.5 Photodesorption lineshape for modified CH_3F/NaCℓ model system. 192
6.6 Photodesorption rate versus laser frequency for CH_3F/NaCℓ in inhomogeneous case..... 195
6.7 Photodesorption lineshape as for Fig. 6.6, but with slightly deeper surface potential..... 197
7.1 Desorption rate versus laser intensity for pyridine on KCℓ... 203
7.2 Desorption rate versus laser intensity for CO on Cu(100)..... 205
7.3 Desorption rate versus laser intensity for CO on NaCℓ..... 206

1. Introduction

The physics of heterogeneous systems, such as the gas-solid interface, is currently a subject of considerable interest. The industrial importance of heterogeneous catalytic reactions provides impetus for understanding the fundamental aspects of gas-solid interactions.[1] Furthermore, photochemical reactions at surfaces, stimulated by intense laser radiation, have been observed in a variety of situations.[2] These processes are made up of basic steps such as adsorption, surface migration and reaction, and desorption.[3,4] We will concentrate in this paper on the desorption process.

A gas molecule is said to be adsorbed when it becomes localized at the (solid) surface in an energetically favourable configuration. Two classes of adsorption are noted. As a gas molecule approaches a solid, it first experiences an attraction due to long range van der Waals forces arising from the correlation of the fluctuating dipole moments in the gas molecule and solid. This interaction alone can lead to adsorption, termed physisorption.[5] The binding energy of a physisorbed molecule is generally less than a few tenths of an electron volt. In addition, the adsorbed molecule may form a stronger, chemical bond with solid atoms leading to chemisorption.[6] In this case the binding energy can be of the order of electron volts. While it is this latter process that is important in chemical processes, we limit ourselves here to considering physisorbed molecules.

In the reverse process, when an adsorbed molecule leaves the surface to the gas phase, desorption occurs. For this endothermic process to take place, energy must be supplied to the adsorbate to break the surface bond. In thermal desorption, the energy is obtained from the thermal (phonon) reservoir of the solid (see Fig. 1.1(a)). This process can be initiated by either (i) reducing the gas pressure in front of the solid (isothermal desorption), or (ii) increasing the temperature of the solid (flash desorption). In either case, the gas-solid system evolves in response to these non-equilibrium stimuli. The thermal desorption rate is found experimentally[7] to typically follow a Frenkel-Arrhenius formula

$$r_{des} = \nu\, e^{-E_d/k_B T} \tag{1.1}$$

Here E_d is the adsorption energy and ν is a kinetic prefactor. While this formula can be understood within the context of Eyring's transition state theory[8] using quasi-equilibrium considerations, nonequilibrium theories of thermal desorption have also been advanced.[9] Quantum mechanical models, beginning with the work of Lennard-Jones et al.,[10] have been studied extensively in recent years.[11-14] From such microscopic models, it is possible to explicitly calculate the prefactor ν in (1.1) in terms of the forces experienced by an adsorbed molecule.

Desorption can also be stimulated by external energy sources. For example, the chemisorption bond can be broken by using an electron or a photon beam to cause an appropriate electronic transition within the adsorbate-solid system.[15] For physisorbed molecules desorption can

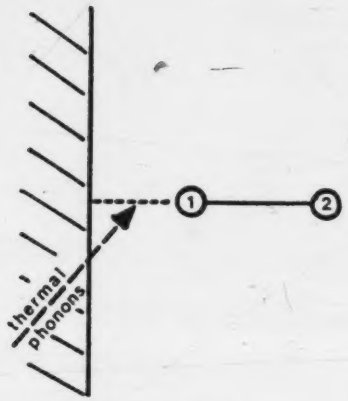

a) thermal desorption

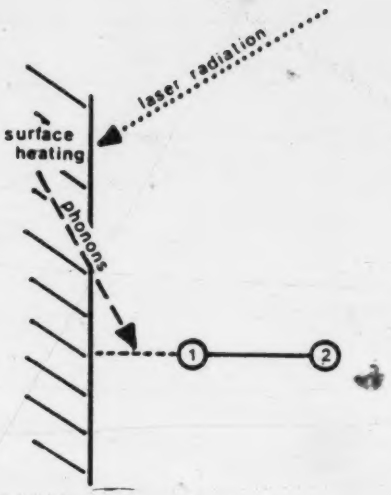

b) laser-induced
thermal desorption

c) laser excites
surface bond directly

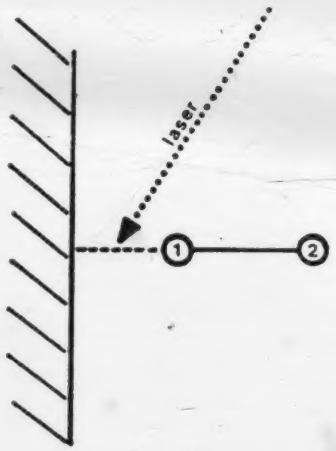

d) laser excites
molecular vibrations

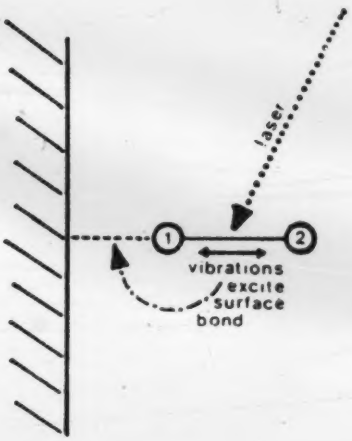

Fig.1.1. Possible channels to desorption.

also be initiated by infrared laser radiation. In this case, low energy photons can excite vibrational modes of the adsorbate and solid, while leaving the electronic state of the adsorbate unaltered. It is this method of stimulating desorption that we address.

Infrared radiation can be absorbed by the gas-solid system in several ways to initiate desorption. Direct absorption by the substrate, generally a non-resonant process, leads to localized heating of the surface region. This process is particularly important on a metal substrate. Enhanced thermal desorption may then proceed from an elevated surface temperature,[16] as shown in Fig.1.1(b). This laser-induced thermal desorption process has been used experimentally.[17]

The laser photons can also deposit their energy directly into the surface bond, exciting frustrated translational motion of the adsorbed molecule, as in Fig.1.1(c). The possibility of stimulating desorption by this selective absorption process has been investigated theoretically by George et al.[18] Explicit microscopic calculations by Jedrzejek et al.[19] predict desorption rates via this mechanism to be negligibly slow except at very high laser intensities. This can be understood by noting that the strongly anharmonic surface potential (for physisorption) has unevenly spaced energy levels, representing the frustrated translational states of an adsorbed molecule. Stepwise excitation by photon absorption quickly becomes a non-resonant process as higher states are reached. In analogy with the theory of gas-phase photodissociation processes,[20] splitting of the energy levels, due to rotational/librational motion, may compensate for the anharmonicity somewhat. This photodesorption process has not yet been

experimentally observed.

Alternatively, the laser may be tuned to excite an internal vibrational mode of an adsorbed molecule, as in Fig.1.1(d). This selective and resonant infrared absorption process has been found experimentally to lead to desorption, as discussed below. Whether the desorption process is also molecule-selective depends on the underlying interaction mechanisms involved. The possibility of selectively desorbing isotopes will be discussed. The coupling between the vibrational and translational motion of an adsorbed molecule, and between the molecule, the substrate, and the rest of the adsorbate, leads to different paths via which desorption may occur. In this paper, microscopic models of these processes are presented, from which the desorption kinetics is calculated.

The process of photodesorption initiated by resonant vibrational excitation has been observed for a number of adsorption systems to date.[2] In the initial work by Heidberg and co-workers,[21,22] desorption of CH_3F from an NaCl substrate was studied. The initial adsorbate coverage was several monolayers, at a temperature of 64-77K - well below the thermal desorption regime. A high intensity pulsed CO_2 laser was tuned to excite the ν_3 (C-F stretch) mode of the adsorbed CH_3F, and desorbing molecules were detected in a mass spectrometer. The resulting desorption yield per laser pulse depends resonantly on laser frequency, as shown in Fig.1.2(a).[22] The peaks of the photodesorption and infrared absorption lineshapes are seen to coincide. In Fig.1.2(b), the desorption yield is found to increase nonlinearly with laser fluence . (Fluence - laser intensity x pulse time) This is suggestive of multiphoton vibrational pumping, by either

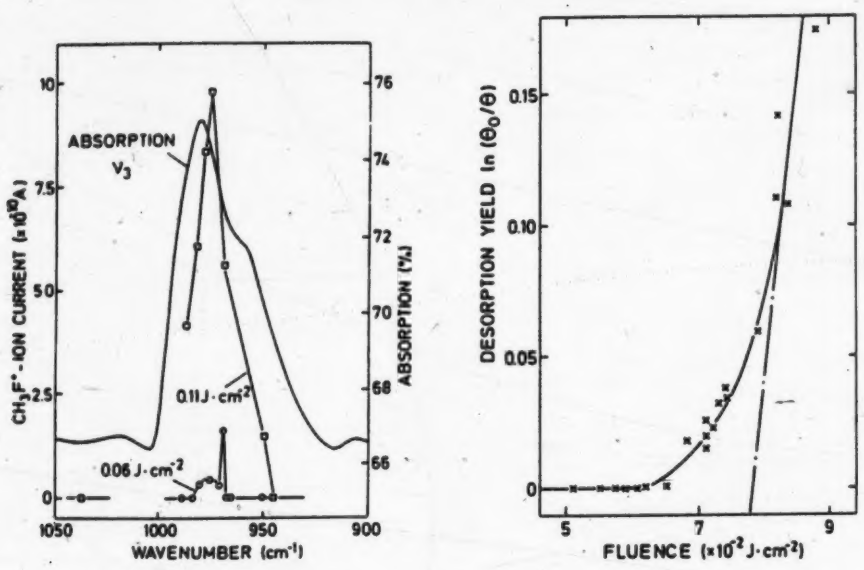

Fig.1.2. Resonant photodesorption yields for CH_3F/NaCℓ at 77 K, from reference 22. **(a)** CH_3F desorption yield per laser pulse as a function of laser frequency, at fluences indicated. Linear infrared absorption spectrum is superimposed. **(b)** CH_3F desorption yield versus laser fluence at frequency Ω_ℓ = 976 cm^{-1}.

coherent or incoherent processes leading to desorption, as noted by Heidberg et al. (For this system, the heat of adsorption is roughly equal to the energy of two incident photons.)

Experiments by Chuang and co-workers have yielded similar results. They photo-excite the asymmetric breathing mode of pyridine adsorbed on Ag and on KCl substrates.[23,24] The dependence of their observed desorption yields on laser frequency is in close agreement with the corresponding SERS spectra.[25] Once again, the yields are found to increase non-linearly with laser fluence. More recently, photodesorption of NH_3 from Cu(100) and Ag(film) has been observed,

with similar results.[26] In addition, coadsorption of NH_3 and ND_3 has been studied. Using the laser to vibrationally excite the NH_3 species, both isotopes are found to desorb with comparable yields. This non-selective desorption process is discussed in detail in Section 3.

Resonant photodesorption by vibrational excitation has also been observed by Heidberg et al. for the CO/NaCl system.[27] On the other hand, careful attempts by Mercier and co-workers to desorb CO from Pd failed.[28] In the latter case, the adsorption bond is much stronger, approximately 1.5 eV. While the experiments discussed above deal with desorption of neutral molecules, photodesorption of methanol ions by infrared photon absorption has also been reported by Mashni and Hess.[29] We will not consider this latter process further here. In summary, photodesorption by laser-vibrational excitation has been observed for a variety of molecules physisorbed on both dielectric and metal substrates.

Theoretical studies of the resonant infrared photodesorption process have been advanced to help understand the interaction mechanisms involved. Beginning with a microscopic model for the couplings within the gas plus solid system, one attempts to predict the observed desorption behaviour shown in Fig.1.2. From the initial investigations by Kreuzer and Lowy,[30] Lucas and Ewing[31] and George et al.[32-34], various theories have been developed. Kreuzer considered step-wise vibrational excitation by incoherent absorption of laser photons, followed by phonon-assisted tunnelling of energy into the translational motion of the adsorbed molecule, leading to desorption. The theory presented in Section 2 developed largely from these ideas. Ewing's theory of photodesorption is constructed in analogy with the

related phenomena of vibrational predissociation of van der Waals molecules.[32] For weakly bound adsorption systems, the probability of elastic tunnelling of a bound but vibrationally excited molecule to the gas phase is calculated. Both these studies suggest that photodesorption is possible via the transition paths suggested above, but more detailed calculations are necessary to predict the desorption kinetics more exactly.

Lin and George[33] have studied the dynamics of energy transfer between the infrared-active vibrational mode of an adsorbed molecule and low frequency librational/translational and phonon modes. Molecular excitation levels are calculated, in terms of the couplings within the laser-adsorbate-solid system, and used to discuss the efficiency of laser-stimulated surface processes. If molecular modes are strongly damped by the substrate, non-selective thermal heating effects are anticipated. However, selective desorption may be expected when the intramolecular coupling is strong or the damping is weak. Recently, the role of phase-dissipative processes in compensating for laser detuning and anharmonic "bottleneck" effects is also considered.[34] It is clear that the kinetics of photodesorption depends critically on the competition between many microscopic coupling processes in the adsorbate.

In addition, Janda and co-workers investigated a desorption model based on a two-level vibrational system for a weakly bound adsorbate.[35] Photon-induced vibrational excitation, non-radiative damping, vibrational dephasing, and tunnelling to the gas phase are included as phenomenological transition rates. By studying the desorption yield as a function of the various rates, they predict that

photodesorption of a weakly bound adsorbate should still be observable in spite of rapid vibrational damping.

A master equation approach to photodesorption has been developed in detail by Fain and Lin and co-workers[36] to model incoherent transition paths leading to desorption. Explicit rate equations for the molecular vibrational level populations are derived, with transition rate coefficients to be determined. In this way, a nonlinear dependence of desorption yield on laser intensity is derived, and narrowing of the yield lineshape is also predicted.[37] Furthermore, vibrational energy transfer laterally in the adsorbate is shown[38] to assist in pumping the higher quantum levels of an anharmonic vibrational mode, as discussed in Section 4. The reduced single-molecule master equation used in this work is similar in spirit to the formalism we represent in Section 2. The main difference is that Fain and Lin thermally average over the states of translational motion of the admolecule, while we will treat them explicitly.

In summary, one finds a variety of theories proposed to explain the observed photodesorption process. The molecule-selective mechanism in which desorption occurs by tunnelling of energy from the photo-excited vibrational mode has been most studied. On the other hand, lateral vibrational coupling induces energy exchange between neighbours in the adsorbate along the path to desorption as Fain and Lin[38] point out. In addition, indirect, resonant surface heating due to strong vibrational damping may enhance non-selective thermal desorption. In this paper, we consider the relative importance of these three desorption mechanisms in detail.

The kinetics of photodesorption stimulated by resonant excitation of a molecular vibrational mode with a laser are calculated here from an explicit microscopic quantum mechanical model of the interacting gas-solid-laser system. In Section 2, a theory of the selective photodesorption process above is developed for a low coverage adsorbate. Using a master equation with explicitly calculated transition probabilities, the rate of photodesorption is predicted. The effect of a resonant surface heating process on the desorption kinetics is shown in Section 3, while enhanced desorption due to lateral vibrational energy transfer is discussed in Section 4. The selective photodesorption model presented in Section 2 is then extended in Section 5 to more strongly coupled adsorption systems by the inclusion of coherent two phonon/photon transition processes in higher order perturbation theory. In Section 6, the photodesorption spectral lineshape is analyzed and compared to the infrared absorption line. Finally, a comparison of explicit theoretical results for the selective photodesorption process and for resonant heating effects is discussed in Section 7 for a variety of experimental systems.

2. Basic Photodesorption Model Theory

2.1 Introduction

We want to theoretically describe the resonant, selective photodesorption process initiated by infrared laser radiation[39]. By comparing the calculated desorption kinetics, based on a microscopic model, with experimentally measured photodesorption yields, the relative importance of the various reaction pathways is determined. First, a quantum mechanical model for the adsorption system is needed. We initially consider a low coverage, homogeneous adsorbate of localized physisorbed molecules which have both translational and internal vibrational degrees of freedom, at low gas pressures. Interaction with the laser radiation and with the phonon bath of the solid leads to transitions among the states of motion of the adsorbed molecules. A quantum statistical formalism is used to calculate transition probabilities entering a master equation that describes the desorption kinetics. In this section, the basic formalism is presented, and its use to calculate desorption rates, as detailed in reference 60, is summarized. Along the way, points of departure for the more detailed study that follows in later sections are noted. The theoretical program is to model the interaction process of Fig.2.1 quantum mechanically, and develop rate equations to describe the desorption process.

The physisorption interaction between a gas molecule and the solid is described by the surface potential shown in Fig.2.2a. The adsorbate is bound to the surface in frustrated translational states labelled by

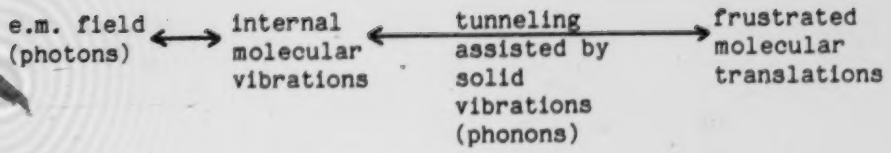

Fig.2.1 The interaction process

the quantum number j, while gas-phase molecules have free translational states denoted q. Internal vibration of the adsorbed molecule is assumed at first to be approximately simple harmonic, giving an energy spectrum of equally spaced vibrational levels, v. The double index (j,v) fully describes the state of an adsorbed molecule in our theory.

To simplify the calculations we assume that the axis of the vibrational coordinate of the adsorbed molecule is oriented perpendicular to the surface. We will furthermore restrict parts 1 and 2 of the molecule to motion along this axis. This one dimensional approximation is most appropriate if the adsorbed molecules are mobile and free to move on the surface. Lateral motion is then decoupled from the motion perpendicular to the surface and thus the desorption process. However, in thermal desorption calculations on localized adsorption systems, it is found that a one dimensional model gives results that are qualitatively similar to the full, three dimensional theory.[50]

The interaction process in Fig.2.1 causes transitions between states (j,v). If a gas molecule, initially adsorbed in a bound state (j,v), is

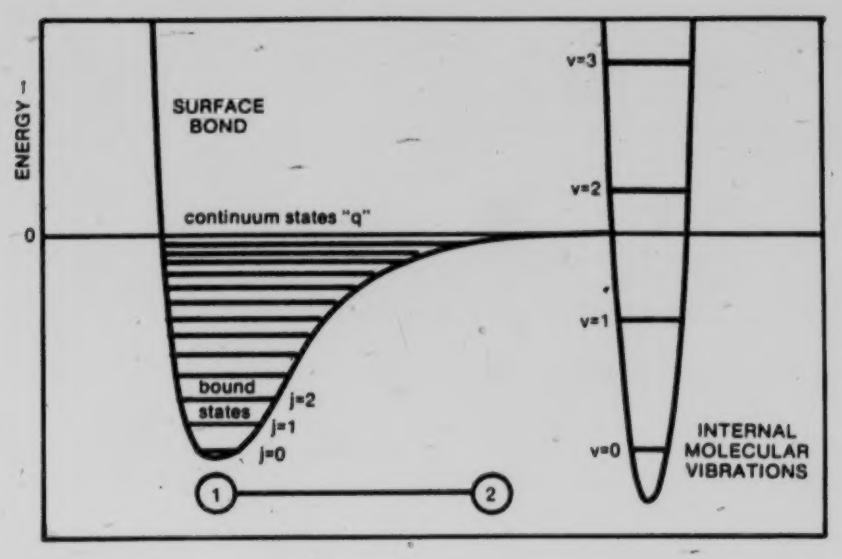

Fig.2.2(a). Energy diagram of gas molecule states

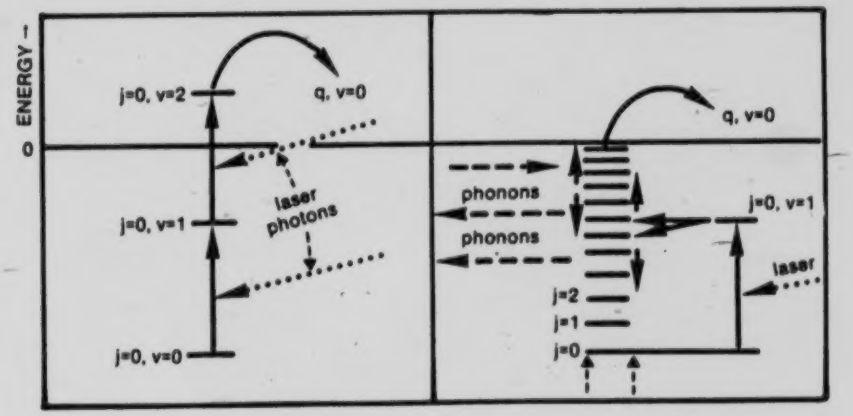

Fig.2.2(b). Two possible paths to desorption

transferred to a free translational state (q,v'), then the surface

bond is broken and desorption occurs. Note that whether the molecule is adsorbed or free depends on the surface bond index (j or q) only. An adsorbate molecule that is vibrationally excited may in fact have positive total energy if the vibrational contribution (state v) exceeds the negative portion due to the bound surface state (j). The desorption process involves both vibrational and surface state excitation, as shown in two possible transition paths in Fig.2.2b. Notice that the path to desorption may be very complex, involving incoherent sequences of many transitions along the way.

We assume that the dynamics of the adsorbate molecules is describable by a stationary Markov process as discussed in Section 2.3. Defining the state occupation probabilities $n_j^v(t)$, we model the time-evolution of the system by the master equation[39]

$$\frac{d}{dt} n_j^v(t) = \sum_{j'v'} R_{jj'}^{vv'} n_{j'}^{v'}(t) \tag{2.1}$$

where, for off diagonal terms ($j,v \neq j',v'$), $R_{jj'}^{vv'}$ is the single particle transition rate from state (j',v') to (j,v). The diagonal term is given by

$$R_{jj}^{vv} = - \sum_{j'v' \neq jv} R_{j'j}^{v'v} = \sum_{v'} R_{cj}^{v'v} \tag{2.2}$$

The desorption rate, r_d, is equal to the rate of depopulation of the bound states (j) and is given by

$$r_d = - \frac{\frac{d}{dt} \sum_{j,v} n_j^v(t)}{\sum_{j,v} n_j^v(t)} \qquad (2.3)$$

and may be determined by numerically solving the coupled system of rate equations (2.1) for specific initial conditions. It turns out that, in most cases, the desorption kinetics is describable by a single time scale, given by the smallest eigenvalue of the rate matrix $R_{jj',vv'}$, as discussed in Section 2.5.

It remains to calculate the transition rates, $R_{jj',vv'}$ and $R_{cj',vv'}$, for the interaction process described in Fig. 2.1. The first step is to construct the Hamiltonian for the gas-solid-laser system, including appropriate interaction terms, as detailed in Section 2.2. The transition rates are defined in Section 2.3, where the master equation is developed. A first order calculation of the rates themselves is summarized in Section 2.4, while subsequent, higher order terms (Section 5) are anticipated. In Section 2.5, the solution of the master equation, both by exact numerical computation, and by an analytic approximation scheme, is considered. Finally, sample results are presented, and a comparison with experimental measurements is discussed.

2.2 The Hamiltonian of the Gas-Solid-Laser System

The Hamiltonian of the gas-solid-laser system is now constructed in second quantized form. We assume, in this chapter, that the density of gas molecules is small, both on the solid surface and in the gas phase, so that gas molecule-gas molecule interactions can be neg-

lected. The gas molecules may then be treated independently.

2.1 The static hamiltonian

We consider one diatomic molecule in a vacuum near a semi-infinite, static, solid surface, and will ignore thermal vibrations and the

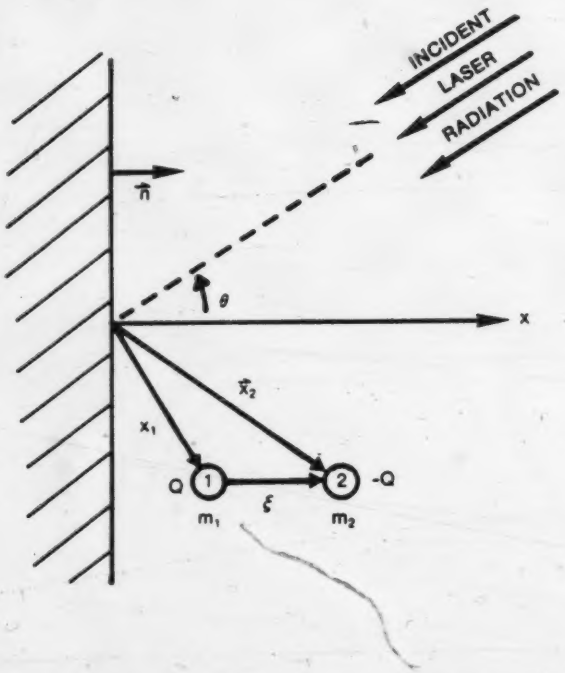

Fig.2.3. Adsorbate molecule configuration.

laser field for now. See Fig. 2.3. Letting $U(x_1-x_2)$ be the interatomic potential of the molecule, and $V_i(x_i)$ be the potential energy of the i^{th} gas atom-solid interaction (i = 1,2), the quantum mechanical Hamiltonian for the diatomic gas molecule and the static solid is

$$H_{st}(x_1,x_2) = -\frac{\hbar^2}{2m_1}\frac{\partial^2}{\partial x_1^2} - \frac{\hbar^2}{2m_2}\frac{\partial^2}{\partial x_2^2} + U(x_1-x_2) + V_1(x_1) + V_2(x_2) \quad (2.4)$$

For a molecule oriented perpendicular to the surface, atom 2 is sufficiently distant from the surface to render its interaction with the solid insignificant. We therefore set $V_2(x_2) = 0$, and introduce centre of mass variables, $m = m_1 + m_2$, $\mu = (m_1^{-1} + m_2^{-1})^{-1}$, $x = \frac{1}{m}(m_1x_1 + m_2x_2)$, and $\xi = x_2 - x_1$, to get

$$H_{st}(x,\xi) = H_\mu(\xi) + H_m(x) + H_{res}(x,\xi) \quad (2.5)$$

where

$$H_\mu(\xi) = -\frac{\hbar^2}{2\mu}\frac{\partial^2}{\partial\xi^2} + U(\xi)$$

$$H_m(x) = -\frac{\hbar^2}{2m}\frac{\partial^2}{\partial x^2} + V_1(x - \frac{\mu}{m_1}\xi_o)$$

and

$$H_{res}(x,\xi) = V_1(x - \frac{\mu}{m_1}\xi) - V_1(x - \frac{\mu}{m_1}\xi_o). \quad (2.6)$$

Here, ξ_o is the mean interatomic spacing of atoms 1 and 2. Since $|\xi-\xi_o|$ is small and $V_1(x)$ is a smooth function, the residual term, H_{res}, in the Hamiltonian will be small; H_{res} is therefore treated as a perturbation.

We now diagonalize H_μ and H_m as

$$H_\mu(\xi)u_v(\xi) = E_v u_v(\xi)$$
$$H_m(x)\phi_j(x) = E_j\phi_j(x) \qquad (2.7)$$

defining the eigenvectors and eigenvalues, $u_v(\xi)$ and E_v, and $\phi_j(x)$ and E_j, for H_μ and H_m, respectively. Taking $U(\xi)$ to be a harmonic potential and $V_i(x)$ to be a Morse potential permits analytic solutions of (2.7).

The total system of many gas molecules is described by the second quantized, many particle, static Hamiltonian given by

$$H_{st} = \int dx d\xi \psi^\dagger(x,\xi)H_{st}(x,\xi)\psi(x,\xi) \quad . \qquad (2.8)$$

We expand the field operator in terms of the complete set of eigenvectors, $\{u_v(\xi)\phi_j(x)\}$, of $(H_\mu + H_m)$ as

$$\psi(x,\xi) = \sum_{j,v} \phi_j(x)u_v(\xi)a_j{}^v \qquad (2.9)$$

where $a_j{}^v$ is the annihilation operator for a particle in the j^{th} state of the surface potential and in the v^{th} internal vibrational state. Then, using the orthogonality of $\{u_v(\xi)\}$ and $\{\phi_j(x)\}$, (2.8) and (2.9) give

$$H_\mu + H_m = \int dx d\xi \psi^\dagger(x,\xi)[H_\mu(\xi)+H_m(x)]\psi(x,\xi) = \sum_{j,v} E_j{}^v a_j{}^{v\dagger} a_j{}^v \qquad (2.10)$$

where

$$E_j^V = E_j + E_V \ . \tag{2.11}$$

Furthermore,

$$H_{res} = \int dx d\xi \psi^{\dagger}(x,\xi) H_{res}(x,\xi) \psi(x,\xi) \ . \tag{2.12}$$

2.2.2 The electromagnetic field

The electromagnetic field at the surface due to the laser radiation must be known. To do so, one solves Maxwell's equations for the appropriate geometry and boundary conditions. The solid is treated as a semi-infinite, lossless, non-magnetic, homogeneous dielectric, with refractive index, n_r (see Fig.2.3). In the Coulomb gauge and in the absence of free charges, the electromagnetic vector potential, $\mathbf{A}(\mathbf{x},t)$, satisfies the wave equation[41]

$$\nabla^2 \mathbf{A} - \frac{1}{v^2(z)} \frac{\partial^2 \mathbf{A}}{\partial t^2} = 0 \tag{2.13}$$

where $\mathbf{n} \times \mathbf{A}$, $\nabla \times \mathbf{A}$, and $n^2(z)\mathbf{A}\cdot\mathbf{n}$ are continuous at $z = 0$. Here, $v(z) = c/n(z)$ is the phase velocity of the wave, while

$$n(z) = \begin{cases} 1; & \text{for } z > 0 \\ n_r; & \text{for } z < 0 \end{cases} \tag{2.14}$$

is the refractive index, equal to unity in the vacuum ($z > 0$), and given by n_r in the solid half-space ($z < 0$).

Before constructing the quantized electromagnetic field from the solutions of (2.13), let us review some of the limitations, and justifications, of employing such a simple model as (2.14) for the dielectric response at a solid surface.[42,43] Formula (2.14) claims that the solid responds in a homogeneous manner to electromagnetic fields at all points in its interior however near or far from the surface. The step function change in (2.14) is indicative of a surface charge layer of infinitesimal thickness and infinite magnitude. This leads, via (2.13), to a discontinuity in the perpendicular component of the electromagnetic field ($\mathbf{E} = -\partial\mathbf{A}/\partial t$) at the surface. However, from the microscopic point of view of an adsorbed molecule, this picture must be considered with some care. In actuality, the induced electronic surface charge layer is of finite magnitude and thickness, extending a distance of a few lattice spacings into the solid. As a result, all fields vary continuously across this charged surface region, in which longitudinal electric fields are also present.

Another deficiency of using (2.14) to describe a real dielectric is the use of a local dielectric function, $\varepsilon(\mathbf{x}) = \varepsilon_0 n^2(\mathbf{x})$. A realistic microscopic description of the electronic response of a solid gives rise to a continuous and non-local constitutive relation such as

$$\mathbf{D}(\mathbf{x},\omega) = \int d^3x' \; \varepsilon(\mathbf{x},\mathbf{x}',\omega)\, \mathbf{E}(\mathbf{x}',\omega) \tag{2.15}$$

where **D** is the electric displacement and the dielectric response function, $\varepsilon(\mathbf{x},\mathbf{x}',\omega)$, varies continuously across the surface. In addition, (2.15) allows the electronic response at **x** to depend on the electric fields at points **x'** in a region near **x**. This non-local behaviour of the dielectric response arises, in linear response theory,[44] from the quantum mechanical, non-local nature of the electrons in the solid, and is most significant for a metal. Non-locality is an essential ingredient in a microscopic determination of the rapid variation of the perpendicular component of the electromagnetic field in the surface region. (For an adsorbate vibrational mode perpendicular to the surface, it is this electric field that couples to the vibrational dipole moment in the infrared absorption process that initiates photodesorption.)

Combining (2.15) with Maxwell's equations leads to, instead of the usual macroscopic boundary condition ($\varepsilon\mathbf{E}\cdot\mathbf{n}$ continuous across an interface), an integral equation for **E**.[42] Alternatively, a Green's function approach leads to an integral expression[43] for the four-vector potential in the Lorentz gauge,

$$A_\mu(x) = A_\mu^0(x) + \sum_{\rho,\nu} \int d^4x_1 d^4x_2 D_{\mu\rho}^0(x-x_1)\ \Pi_{\rho\nu}(x_1,x_2) A_\nu(x_2)\ , \qquad (2.16)$$

where $(\mu,\rho,\nu) = 1,\ldots,4$. Here $A_\mu(x) = (\Phi(\mathbf{x},t), \mathbf{A}(\mathbf{x},t))$ where Φ is the scalar electromagnetic potential, $D_{\mu\rho}^0$ is the free photon Green's function, and $\Pi_{\rho\nu}$ is the proper polarizability, derived in linear response theory. For a homogeneous (infinite) medium, Π depends only on

the difference, $x_1 - x_2 = (\mathbf{x}_1-\mathbf{x}_2, t_1-t_2)$, and (2.16) becomes a convolution integral that is simply solved by Fourier transform. However, near a surface, Π depends on both $\mathbf{x}_1$ and $\mathbf{x}_2$ separately, and Fourier transform leaves an infinite-size matrix equation in momentum space.

Maniv and Metiu[46] have performed an approximate numerical solution of this problem for a "free electron" metal. Calculating Π for non-interacting electrons and then solving (2.16) amounts to a Random Phase Approximation for the interacting electron system response. In this way, the electromagnetic field in the surface region is then shown in Fig.2.4 to vary rapidly across the surface region of several Angstroms width. The real part of the perpendicular component of the electric field, E_z, takes on the constant value of the standard macroscopic theory everywhere outside the metal electron gas. As one enters the metal, E_z drops to zero in several lattice lengths. Note also that electron-hole pair creation, due to photon absorption mediated by the surface, results in a non-zero imaginary electric field component just beneath the surface. These effects are absent in the macroscopic dielectric description of (2.14). Note that plasmon excitation in the metal does not occur for infrared frequencies which are far below the (flat) surface plasmon frequency.

Let us see how these predictions will affect laser-photon absorption by an internal vibrational mode of an adsorbed molecule. We are interested in the interaction, H_ℓ, between the electromagnetic radiation field and a charged, diatomic molecule. Describing the molecule by point charges, $\pm Q$, with masses, m_1 and m_2, located at $\mathbf{x}_1$ and $\mathbf{x}_2$ as shown in Fig. 2.3, the method of minimal coupling yields[41]

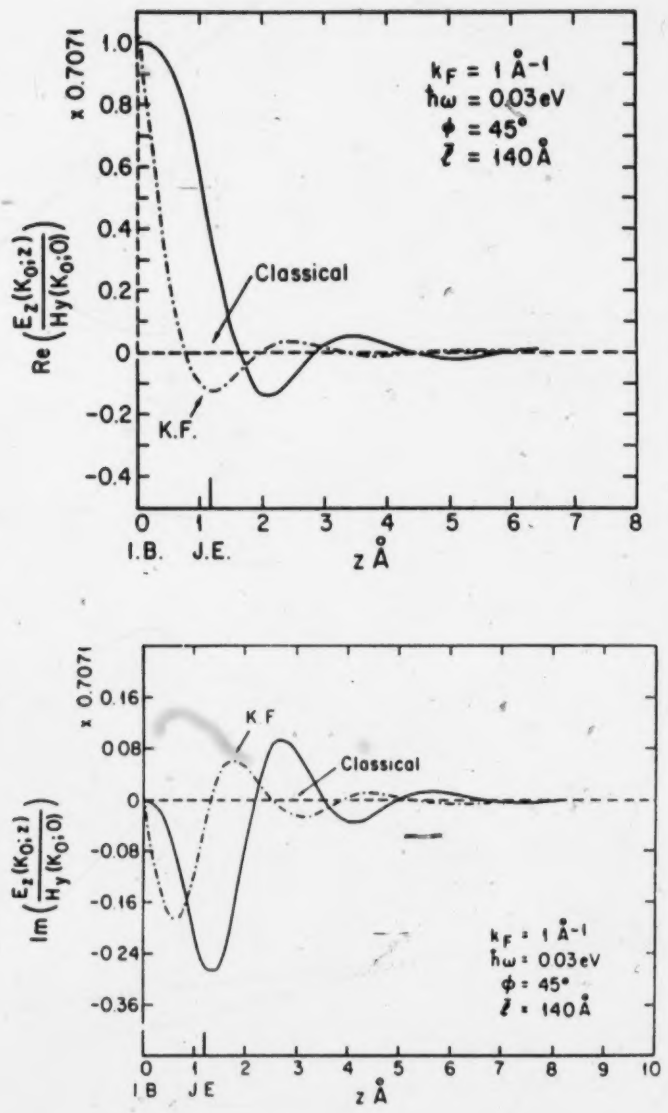

Fig.2.4. Electromagnetic fields at a metal surface.[46] Real and imaginary parts of the field ratio $E_z(z)/H_y(0)$ as a function of distance z into the solid are given by solid lines. Dashed-dotted line is from a simpler nonlocal model,[43] while dashed line is the classical result. Positions of the infinite barrier (I.B.) and jellium edge (J.E.) are noted; k_F is the Fermi wave vector, $\hbar\omega$ is the incident photon energy at the angle of incidence ϕ, and $\bar{\ell}$ is the mean free path of electrons in the solid.

$$H_\ell = i\hbar Q\left[\frac{\mathbf{A}(\mathbf{x}_1,t)}{m_1}\cdot\frac{\partial}{\partial\mathbf{x}_1} - \frac{\mathbf{A}(\mathbf{x}_2,t)}{m_2}\cdot\frac{\partial}{\partial\mathbf{x}_2}\right] . \tag{2.17}$$

If we ignore the effect of the adsorbed molecule on the metal, $\mathbf{A}(\mathbf{x},t)$ is just that calculated in (2.16) for a semi-infinite solid with no adsorbate. Now, we assume that the molecule is strictly physically adsorbed so that it is completely outside the electron gas of the metal. Since the fields outside vary slowly - with spatial scale given by the infrared radiation wavelength - $\mathbf{A}(\mathbf{x},t)$ changes little over atomic distances, such as $\xi = \mathbf{x}_1-\mathbf{x}_2$, and (2.17) reduces to

$$H_\ell(\mathbf{x},\xi) = -i\hbar\,\frac{Q}{\mu}\,\mathbf{A}(\mathbf{x},t)\cdot\frac{\partial}{\partial\xi} . \tag{2.18}$$

This is the usual dipole approximation in the long wavelength limit; μ is the molecular reduced mass. The fortunate conclusion is that one may use the standard, macroscopic, electromagentic theory to calculate $\mathbf{A}(\mathbf{x},t)$ and the usual derivative coupling Hamiltonian in (2.18), provided the adsorbate molecule is physisorbed. The successful use of the dipole coupling approximation to describe infrared absorption data supports this conclusion. The use of a flat model surface, devoid of roughness capable of inducing local field enhancements in the infrared, is only justified in hindsight by the reasonable values of the effective charge Q deduced from experiments. Enhanced infrared photoeffects may still be possible on roughened surfaces or in certain geometries.[47,48] These possibilities are not addressed here.

On the other hand, a chemisorbed molecule shares electrons with the substrate and is, therefore, not "outside" the (metal) electron gas, implying that equation (2.17), along with the exact microscopically calculated fields, should be used. However, representing the adsorbate molecule's electrons classically by fixed atomic charges is of questionable validity anyway when chemisorption takes place. We therefore consider only the physisorption case here. Finally, note that we have thus far ignored the underlying atomic structure of the substrate which induces a crystalline electromagnetic field.[49]

In our physisorption model, we therefore consider the electromagnetic field of the laser to be described by (2.13) and (2.14), with its derivative-coupling to adsorbate vibrations given by (2.18). The quantized electromagnetic vector potential may be expanded as[50]

$$\mathbf{A}(\mathbf{x},t) = \sum_{k\beta} \left[\Phi_{k\beta}\, \mathbf{U}_{k\beta}(\mathbf{x})\, e^{-i\Omega_{k\beta}t}\, C_{k\beta} + \text{hermitian conjugate} \right] \qquad (2.19)$$

in terms of the normal modes of the electromagnetic field, appropriate for planewave radiation incident on the solid. These modes are described by the solutions, $\mathbf{U}_{k\beta}(\mathbf{x})e^{-i\Omega_{k\beta}t}$, of (2.13) and (2.14), and may be constructed from the sum of incident, reflected, and transmitted rays using Snell's law and Fresnel's equations (see Appendix A). In (2.19), k and β are the incident wave vector and polarization of the normal modes. $\Omega_{k\beta}$ is the oscillation frequency, $\Phi_{k\beta}$ is a normalization factor, and $C_{k\beta}$ is the (boson) annhilation operator for the (k,β) mode. Orthogonality of the modes $\mathbf{U}_{k\beta}(\mathbf{x})$ is given by

$$\int dx\, n^2(z) U_{k\beta}(x) \cdot U_{k'\beta'}^{*}(x) = \delta_{\beta\beta'}\, \delta_{k,k'} \,. \tag{2.20}$$

Combining (2.20) and the boson commutation relations

$$[C_{k\beta}, C_{k'\beta'}^{\dagger}] = \delta_{\beta\beta'}\, \delta_{k,k'} \;\; ; \;\; [C_{k\beta}, C_{k'\beta'}] = 0 \tag{2.21}$$

allows one to write the Hamiltonian for the electromagnetic radiation in the presence of the solid as

$$H_{em} = \frac{1}{2} \int dx \left[\varepsilon(z) E^2(x) + \frac{1}{\mu_0} B^2(x) \right] = \sum_{k,\beta} \hbar\, \Omega_{k\beta} \left(C_{k\beta}^{\dagger} C_{k\beta} + \frac{1}{2} \right) . \tag{2.22}$$

The interaction between the laser and an adsorbate molecule (2.18) is then written in second quantization as

$$H_{\ell} = \int dx d\xi \psi^{\dagger}(x,\xi) H_{\ell}(x,\xi) \psi(x,\xi)$$

$$= -i\hbar \frac{Q}{\mu} A(0,t) \int dx d\xi \psi^{\dagger}(x,\xi) \frac{\partial}{\partial \xi} \psi(x,\xi) \,. \tag{2.23}$$

In (2.23) we have taken $A(x,t) = A(0,t)$ where the origin is chosen to be just above the surface at the adsorption site, since the radiation wavelength is much larger than the atomic dimensions of the bound

state wave functions contained in $\psi(x,\xi)$. Defining $C_{k\beta}(t) = \exp(-i\Omega_{k\beta}t)\, C_{k\beta}$ in (2.19) gives

$$A(t) = A(0,t) = \frac{M}{2\epsilon_0} \sum_{k\beta} \Omega_{k\beta}^{-1/2} U_{k\beta}(0)[C_{k\beta}^{\dagger}(t) + C_{k\beta}(t)] \qquad (2.24)$$

2.2.3 Dynamics of the Solid-Phonons

To treat the solid adequately requires consideration of its thermal vibrations which induce a dynamic surface displacement

$$a(r,t) = \left(\frac{M}{2\rho}\right)^{1/2} \sum_{J} \omega_J^{-1/2} [u_J(r)e^{-i\omega_J t}b_J + \text{hermitian conjugate}] . \qquad (2.25)$$

Here, $u_J(r)e^{-i\omega_J t}$ is the atomic displacement at (r,t) due to the J^{th} phonon mode with frequency ω_J as calculated by Ezawa,[51] b_J is the phonon (boson) annihilation operator, and ρ is the mass density of the solid. We will approximate $a(r,t)$ by the displacement field found in the bulk, where

$$u_J(r) = \frac{\hat{e}_{p\sigma}}{V^{1/2}} e^{ip\cdot r} . \qquad (2.26)$$

Here, $\hat{e}_{p\sigma}$ is the unit polarization vector for the phonon mode with wavevector p and polarization σ, and V is the volume of the solid. Choosing the origin to be at the surface position of the adsorbed molecule in question, we approximate the surface displacement as

$$a(t) = a(0,t) = \left(\frac{\hbar}{2M_S N_S}\right)^{1/2} \sum_{p\sigma} \frac{\hat{e}_{p\sigma}}{\omega_{p\sigma}^{1/2}} \left(b_{p\sigma}(t) + b_{p\sigma}^{\dagger}(t)\right) . \qquad (2.27)$$

Here, M_S is the mass of the unit cell in the solid, N_S is the number of such cells and $b_{p\sigma}(t) = e^{(-i\omega_{p\sigma}t)} b_{p\sigma}$. This formula assumes that an adsorbed molecule does not feel the lateral variation in $a(r,t)$ along the surface. This is appropriate at low temperatures for which long wavelength phonon displacements dominate in (2.27). By employing bulk phonon modes (2.26) to describe the surface displacement, we have neglected the softening of certain surface vibrational modes (Rayleigh waves) due to the reduced coordination of the surface atoms. As a consequence, the mean squared thermal surface displacement derived from (2.27) is somewhat small,[52] and its effect on an adsorbed molecule, as given below, is correspondingly diminished. However, it is known that this discrepancy causes no qualitative errors in the desorption kinetics, and may be accounted for quantitatively by a small adjustment of substrate parameters.[53]

To include the effect of thermal vibrations of the substrate in the Hamiltonian, note that the surface to molecule displacement is now $x \to a(t)$, which in (2.4) gives

$$H_{st} \to H_{st} + V_1(x_1 - a(t)) - V_1(x_1) \qquad (2.28)$$

ignoring $V_2(x_2)$ here. We thus identify the phonon interaction Hamiltonian which can be expanded in powers of the dynamic surface displacement as

$$\underline{H_{ph}}(x,\xi) = V_1(x - \frac{\mu}{m_1}\bar{\xi} - a(t)) - V_1(x - \frac{\mu}{m_1}\xi)$$

$$= -a(t)\cdot\frac{\partial}{\partial x} V_1(x - \frac{\mu}{m_1}\xi) + \frac{1}{2!}(a\cdot\frac{\partial}{\partial x})^2 V_1(x - \frac{\mu}{m_1}\xi) + \ldots$$

(2.29)

The second-quantized phonon-adsorbate molecule interaction is thus

$$H_{ph} = -\sum_{i=1}^{3} a_i(t) \int dx d\xi\ \psi^\dagger(x,\xi)\left[\frac{\partial}{\partial x_i} V(x - \frac{\mu}{m_1}\xi)\right]\psi(x,\xi)$$

$$+ \frac{1}{2}\sum_{i,j=1}^{3} a_i(t)a_j(t)\int dx d\xi\ \psi^\dagger(x,\xi)\left[\frac{\partial^2}{\partial x_i \partial x_j} V(x - \frac{\mu}{m_1}\xi)\right]\psi(x,\xi)$$

$$+ \ldots \qquad (2.30)$$

The Hamiltonian for the solid is, in the harmonic approximation,

$$H_s = \sum_{p\sigma} \hbar\omega_{p\sigma}(b_{p\sigma}^\dagger b_{p\sigma} + \frac{1}{2}) . \qquad (2.31)$$

2.2.4 The complete Hamiltonian

We can now construct the complete Hamiltonian for the dynamical gas-solid-laser system. It is assumed that initially (for $t < 0$), thermal equilibrium conditions exist in the gas-solid system, and that at $t = 0$

the laser is turned on. The initial occupation of states, given by $H_\mu + H_m + H_s + H_{em}$, then evolves with time according to the interaction terms, $H_{ph} + H_\ell + H_{res}$, which we turn on at t=0. The complete Hamiltonian is thus

$$H = H_\mu + H_m + H_s + H_{em} + \theta(t)\,[H_{ph} + H_\ell + H_{res}]$$

$$= H_o + \theta(t)\, H_{int} \qquad (2.32)$$

Formally, H_{res} should be included as a static correction to H_μ and H_m for all times. This has been done recently by Landes et al.[54], leading to shifted negative energy (i,v) states, and broadened, positive energy, resonance states. Initially, only the bound, negative energy states are occupied in thermal equilibrium with $k_BT \ll V_o$. (V_o is the maximum depth of the surface potential, $V_i(\mathbf{x}_i)$.) Since H_{res} does not contribute to the dynamics involving only the adsorbed states, it may be neglected for $t < 0$. We have therefore treated H_{res} as a dynamic perturbation in (2.32).[31]

Note that we have assumed that the laser is kept on throughout the complete desorption process. When a pulsed laser is used, our theory predicts that desorption occurs, with rate r_d, for the duration of the pulse. The connection between r_d and the experimental desorption yield per laser pulse will be discussed in Section 2.5.

2.3 The Master Equation

In Section 2.1, we proposed to describe the desorption processes by the master equation

$$\frac{d}{dt} n_i(t) = \sum_{i'} R_{ii'} n_{i'}(t) \tag{2.1}$$

where the double index $i = (j,v)$ denotes states of an adsorbed molecule. This type of master equation was first derived by Pauli and has been discussed from different points of view in the past.[35-37]

Recently, Fain and Lin[36], Gortel and Kreuzer[4], and Efrima et al.[13], have considered the derivation of master equations for desorption kinetics. In photodesorption, an adsorbed molecule interacts with both the thermal phonon reservoir of the solid and the electromagnetic field of the laser. The evolution of the density matrix of the whole system is governed by the Liouville equation. An equation of motion for the reduced density matrix of the adsorbate only is obtained by averaging over the reservoir states, using the standard Zwanzig projection operation method. To obtain a master equation of the form shown in (2.1), it is necessary to assume that the phonon and photon reservoirs equilibriate rapidly enough to lose memory effects between molecular transitions. The desorption dynamics is thus approximated by a Markov process. The buildup of correlations among the phases of off-diagonal elements of the reduced density matrix is also ignored in (2.1) with transition rates calculated in lowest order, as given by Fermi's golden rule formula.

To introduce our theoretical formulation of the transition rate calculation that follows in Section 2.4 and especially in Section 5, we construct the master equation (2.1) as shown below.[4] The quantity of interest is the occupation probability $n_j(t)$ for a molecule to be in the j^{th} state, given by

$$n_j(t) = \mathrm{Tr}\,[\hat{n}_j \rho(t)] \tag{2.33}$$

where $\hat{n}_j = |j><j|$ is the molecule number operator, and $\rho(t)$ is the (normalized) density matrix of the full, interacting, solid + gas molecule + laser system. In the Interaction Picture based on (2.32), the trace operation in (2.33) runs over all states of a gas molecule, $|j>$, and all possible many-phonon states of the solid and many-photon states of the laser radiation. The density matrix may be expressed as

$$\rho(t) = e^{-iH_0 t/\hbar}\, U(t)\rho(0)U^{\dagger}(t) e^{iH_0 t/\hbar} \tag{2.34}$$

in terms of the evolution operator

$$U(t) = T \exp\left[\frac{1}{i\hbar}\int_0^t d\tau H_{int}(\tau)\right]$$

$$= \sum_{n=0}^{\infty} \frac{1}{n!}\left(\frac{1}{i\hbar}\right)^n \int_0^t d\tau_1 \ldots d\tau_n\, T\, H_{int}(\tau_1) \ldots H_{int}(\tau_n) \tag{2.35}$$

where T is the Wick time ordering operator.[5b] Equation (2.32) gives

$$H_o = H_\mu + H_m + H_s + H_{em} \tag{2.36a}$$

and

$$H_{int}(t) = e^{iH_o t/\hbar} [H_\ell + H_{ph} + H_{res}] e^{-iH_o t/\hbar} . \tag{2.36b}$$

Before turning on the interaction at t = 0, the molecule, solid, and laser states are assumed to be uncorrelated, so that the initial conditions may be given by

$$\rho(0) = \rho_m \rho_s \rho_\ell . \tag{2.37}$$

Here, $\rho_{m,s,\ell}$ are the (diagonal) initial-time density matrices for the molecule, solid and laser subsystems, respectively. Specifically, ρ_s represents thermal equilibrium in the solid, ρ_ℓ describes the steady state laser intensity spectrum, while ρ_m gives the initial, classical thermal occupation of the molecule states,

$$\rho_m = \sum_j |j\rangle n_j(0) \langle j| \tag{2.38}$$

where

$$n_j(0) = \frac{e^{-E_j/k_B T}}{\sum_i e^{-E_i/k_B T}} .$$

Substituting (2.37) and (2.34) into (2.33), and writing the trace over molecule states explicitly, gives

$$n_j(t) = \sum_i \mathrm{Tr}_{s,\ell} \left[\langle i|U^\dagger(t)|j\rangle\langle j|U(t)|i\rangle \rho_s \rho_\ell \right] n_i(0) \ . \tag{2.39}$$

(Note that $|i\rangle$, $|j\rangle$ are molecule states only, while U(t) operates on states of the molecule, solid, and laser, and that the trace is taken over solid and laser states.) The time derivative of (2.39) gives

$$\frac{d}{dt} n_j(t) = \sum_j R_{ji}(t) n_i(0) \tag{2.40}$$

where

$$R_{ji}(t) = \frac{d}{dt} \mathrm{Tr}_{s,\ell} \left[\langle i|U^\dagger(t)|j\rangle\langle j|U(t)|i\rangle \rho_s \rho_\ell \right] \ . \tag{2.41}$$

To make the connection between equation (2.40) and the master equation (2.1), we must first consider (2.40) for times short on the timescale of the evolution of $n_i(t)$, that is, $t \ll t_{trans}$. The transient timescale, t_{trans}, depends both on the magnitude of the transition rates and on the initial conditions. However, we are not interested in times as short as $\hbar/E$ where E is the characteristic energy scale of the system. In the time limit

$$\hbar/E \ll t \ll t_{trans} , \tag{2.42}$$

we have

$$n_i(0) = n_i(t) \tag{2.43a}$$

and time-independent transition rates

$$R_{ij} = R_{ij}(t) . \tag{2.43b}$$

Equation (2.40) thus has the form of the master equation (2.1) at initial times given by (2.42). To extend (2.40) to later times, it is necessary to ignore coherent growth of off-diagonal density matrix elements, equivalent to making a repeated random phase approximation.[55] Markovian behaviour is assumed implicitly by keeping the reservoir density matrices, ρ_s and ρ_ℓ, constant in (2.41) throughout the desorption process. Under these assumptions, the master equation (2.1) may be used to describe the time evolution of adsorbed molecules, with transition rates calculated according to (2.41) in the appropriate time limit, (2.42).

In the next section, we calculate these transition rates to lowest order in perturbation theory. This is generally sufficient in the limit or rapid dephasing of the off diagonal density matrix elements, as shown by Fain and Lin.[36] This is often the case, as far as the internal molecular vibrational levels are concerned. However, this approximation breaks down when the surface bond states are also considered explicitly. Efficient phonon-assisted transitions between sur-

face bond states make the rapid-dephasing-approximation invalid for these states. By expanding the transition rate, R_{ji} in (2.41), to higher orders in the interaction Hamiltonian, we relax the upper end of the time limit in (2.42) slightly and thus reduce the severity of the "repeated random phase approximation". Coherent effects represented by these higher order contributions to the transition rates are considered in Chapter 5. The usefulness of the form of equation (2.41) will then become apparent, along with its relation to the T-matrix formulation of scattering theory.

Finally, we note that higher order transition rate terms arise within the phenomenological formulation of the conventional Bloch equations,[59] when they are generalized to treat a system with more than two energy levels.

2.4 The Transition Rates in Lowest Order Perturbation Theory

The transition rates, R_{ij}, that enter the master equation (2.1), are now calculated using the rate formula (2.41) taken to lowest order in the interaction Hamiltonian (2.36). First, the rate formula is simplified by taking $U(t)$ to first order in H_{int} in (2.35), writing the trace operations explicitly, and inserting an identity matrix for the solid and laser states between $U^{\dagger}$ and U in (2.41). This gives

$$R_{ji}(t) = \frac{d}{dt} \sum_{N_s' N_\ell'} \sum_{N_s N_\ell} \left| \langle N_\ell', N_s', j \mid \frac{1}{i\hbar} \int_0^t d\tau H_{int}(\tau) \mid i, N_s, N_\ell \rangle \right|^2$$

$$*\rho_S(N_S)\rho_\ell(N_\ell) \ , \qquad (2.44)$$

where the diagonal density matrix elements, $\rho_S(N_S)$ and $\rho_\ell(N_\ell)$, are the probabilities of the solid occupying the many-phonon state $N_S = \{n_{p_1\sigma_1}^S, n_{p_2\sigma_2}^S, \ldots\}$, and of the laser radiation being in the many-photon state $N_\ell = \{n_{k_1\beta_1}^\ell, n_{k_2\beta_2}^\ell, \ldots\}$, respectively. Performing the time derivative in (2.44) and taking the long time limit (2.42), gives Fermi's golden rule formula

$$R_{ji} = \sum_{N_S', N_\ell'} \sum_{N_S N_\ell} \frac{2\pi}{\hbar} \left| \langle N_\ell', N_S', j \left| H_{int} \right| i, N_S, N_\ell \rangle \right|^2$$

$$*\delta(E_i + E_S + E_\ell - E_j - E_S' - E_\ell')\, \rho_S(N_S)\rho_\ell(N_\ell) \ . \qquad (2.45)$$

This rate formula is valid provided the time scale of the transient evolution of the adsorbate is much longer than the timescale $\hbar/\Delta E$ corresponding to typical energies of the system. Specifically, ΔE is the energy scale on which the matrix element in (2.45) and the density of states of the phonons and photons vary. We anticipate here an integral approximation of the sums in (2.45), which allow for transitions from all occupied initial states, and to all possible final states of the solid and laser.

We now summarize the evaluation of the transition rate given above, which receives three independent contributions - from the laser, phonon, and residual coupling terms in the interaction Hamiltonian. Details may be found in references 39 and 60.

2.4.1 Laser-assisted vibrational transitions

The electric dipole coupling of the adsorbate molecule to the laser radiation induces step-wise vibrational transitions, $v \to v \pm 1$, involving absorption and emission of single photons. Inserting H_ℓ (2.23) into (2.45) and writing the double molecule index (j,v) explicitly now gives the transition rate

$$L_{j'j}^{v'v} = \sum_{N_\ell'} \sum_{N_\ell} \rho_\ell(N_\ell) \frac{2\pi}{\hbar} \left| \langle N_\ell', j'v' | H_\ell | jv, N_\ell \rangle \right|^2$$

$$= \frac{2\pi}{\hbar} \sum_\beta \int dk \, \frac{1}{\Omega_k} \left| Y(j',v',j,v) \cdot U_{k\beta}(0) \right|^2$$

$$* [n_{k\beta}^\ell \, \delta(E_j{}^{v'} - E_j{}^v - \hbar\Omega_k) + (n_{k\beta}^\ell + 1)\delta(E_j{}^{v'} - E_j{}^v + \hbar\Omega_k)] \tag{2.46}$$

where $n_{k\beta}^\ell$ is the mean occupation number for the $(k\beta)$ photon mode and

$$Y(j',v',j,v) = -i\hbar \sqrt{\frac{\hbar}{2\varepsilon_0}} \frac{Q}{\mu} \delta_{j'j} \int d\xi \, u_{v'}{}^*(\xi) \frac{\partial}{\partial \xi} u_v(\xi). \tag{2.47}$$

We now use a one-dimensional approximation ($\xi = \xi_n$) and let $\{u_v(\xi)\}$ be harmonic oscillator wave functions with eigenvalues $v\hbar\Omega$ in the evaluation of (2.47). Ignoring spontaneous photon emission (this is an excellent approximation for an on-resonant laser), the photon occupation function is related to the laser intensity distribution

$$I_{k\beta} = c\left|U_{k\beta}{}^{i}(0)\right|^{2} \hbar\Omega_k \; n_{k\beta}{}^{\ell} \tag{2.48}$$

where $U_{k\beta}{}^{i}(0)$ is the incident part of the wave amplitude. Combining these results in (2.46) and integrating, using polar coordinates $k \rightarrow \omega,\hat{R}$, over the incident laser radiation wavevector which is strongly peaked about Ω_ℓ, $\hat{R}_o$ and assumed to be p-polarized, leads to

$$L_{j'j}{}^{v'v} = \frac{Q^2}{2\varepsilon_o \mu c \hbar \Omega} \pi I g(\Omega) F(\theta)[v'\delta_{v,v'-1} + (v'+1)\delta_{v,v'+1}\;]\delta_{jj'}. \tag{2.49}$$

Here, the dependence of $L_{j'j}{}^{v'v}$ on the angle of incidence, θ, of the radiation is given by

$$F(\theta) = \left| \frac{\hat{n}\cdot U_{k,p}(0)}{U^{i}{}_{k,p}(0)} \right|^{2}_{k=(\Omega/c,\hat{k}_o)} = \frac{4n_r{}^{2}\sin^{2}\theta}{\left[n_r + \sqrt{1 + (1-1/n_r{}^{2})\tan^{2}\theta}\right]^{2}} \tag{2.50}$$

For an insulator such as NaCℓ with $n_r \approx 1.5$ in the infrared, $F(\theta)$ is peaked at an intermediate angle of incidence of $\theta \approx 60°$. For a perfect conductor, one gets by letting $n_r \rightarrow \infty$ for $\theta < 90°$,

$$F(\theta) \approx 4 \sin^{2}\theta \;, \tag{2.51}$$

which favours a grazing incidence angle. In (2.49) we introduced the frequency distribution of the incident laser intensity, assumed for practicality to be given by the Lorentzian, so that

$$g(\Omega) = \frac{1}{\pi} \frac{\Gamma_\ell/2}{(\Omega-\Omega_\ell)^2 + \Gamma_\ell^2/4} \qquad (2.52)$$

where Ω_ℓ and Γ_ℓ are the central frequency and full width at half maximum of the laser line shape, respectively, and Ω is the vibrational frequency.

In deriving (2.49) from the Golden Rule expression, the vibrational levels were assumed to be sharply defined. In actuality, the spectral line shape of adsorbed molecules is non-negligible[61] and we therefore include a Lorentzian distribution of vibrational frequencies to be integrated over in (2.49). This phenomenological procedure has the effect of replacing the linewidth, Γ_ℓ, in $g(\Omega)$ in (2.52) with

$$\Gamma = \Gamma_\ell + \Gamma_v \, . \qquad (2.53)$$

(This procedure can be justified in the master equation formalism of Fain and Lin[36], for example.) Thus, the total linewidth Γ entering (2.49) contains contributions from the laser (Γ_ℓ) and molecular (Γ_v) linewidths. Only homogeneous broadening of the vibrational levels may be treated in this way, as discussed further in Section 6. Furthermore, we assume that Γ_v is independent of the specific quantum levels involved, as appropriate when vibrational dephasing is more rapid than damping.[57] This is anticipated to be the case here.[62]

2.4.2 The phonon interaction

(i) Bound state-bound state transitions

Transitions due to the phonon interaction, H_{ph}, can involve both sur-

face states, j, and vibrational states, v. Including only the first derivative contribution in H_{ph} (2.29) in (2.45) gives the phonon-assisted transition rate

$$P_{j',j}^{v'v} = \sum_{N_S'} \sum_{N_S} \rho_S(N_S) \frac{2\pi}{\hbar} \left| \langle N_S', j'v' | -a(t) \cdot \frac{\partial}{\partial x} V_1(x - \frac{\mu}{m_1} \xi) | jv, N_S \rangle \right|^2$$

$$= \frac{2\pi}{\hbar} \left(\frac{\hbar}{2M_S N_S} \right) \sum_{p,\sigma} \frac{|\hat{e}_{p\sigma} \cdot n|^2}{\omega_{p\sigma}} \left| V_{j'v',jv}^{(1)} \right|^2$$

$$* \{ n_{p\sigma}^S \, \delta(E_{j'}^{v'} - E_j^v - \hbar\omega_{p\sigma}) + (n_{p\sigma}^S + 1) \, \delta(E_{j'}^{v'} - E_j^v + \hbar\omega_{p\sigma}) \} \tag{2.54}$$

Here we have used (2.27) and introduced the thermal occupation function $n_{p\sigma}^S$ for the phonon mode (p,σ). In the one-dimensional approximation, $\mathbf{x} = xn$, $\xi = \xi n$, we have

$$V_{j'v',jv}^{(1)} = \langle j'v' | \frac{\partial}{\partial x} V_1(x - \frac{\mu}{m_1} \xi) | jv \rangle$$

$$= \sum_{\ell=0}^{\infty} \frac{1}{\ell!} \left(-\frac{\mu}{m_1} \right)^{\ell} \langle v' | (\xi - \xi_o)^{\ell} | \psi \rangle \langle j' | \frac{\partial^{\ell+1}}{\partial x^{\ell+1}} V_1(x - \frac{\mu}{m_1} \xi_o) | j \rangle \tag{2.55}$$

A Morse potential is used for $V_1(x - \mu/m_1 \, \xi)$, extending perpendicular to the surface. Hence

$$V_1(x) = V_0[e^{-2\gamma(x-x_0)} - 2e^{-\gamma(x-x_0)}] \tag{2.56}$$

This potential has a maximum depth of V_0 at x_0 and a range given by γ^{-1}. The energy eigenvalues and wave functions of this potential are known analytically, making the Morse potential convenient from a calculational point of view. Current experimental accuracy in determining V_0 and γ^{-1}, combined with our use of a one-dimensional theory, does not necessitate the use of a more accurate physisorption potential.

Since $|\xi-\xi_0| \leq \gamma^{-1}$, the evaluation of the surface potential matrix element, $V_{j'v',jv}^{(1)}$ for specific (j'v',jv), need only include the lowest order contributing term in the expansion (2.55). (See Appendix B for the explicit evaluation of (2.55).) Furthermore, by assuming the Debye model for bulk phonons and asssuming $\omega_{p\sigma}$ is independent of the phonon polarization σ allows the replacement

$$\sum_{p\sigma} |\hat{e}_{p\sigma} \cdot n|^2 \rightarrow \frac{3N_s}{\omega_D^3} \int_0^{\omega_D} d\omega\ \omega^2 \tag{2.57}$$

in (2.54). Combining (2.54) to (2.57) and using (B.1-4) gives

$$\begin{aligned} P_{j',j}^{v'v} = \{&F_{j',j}^{v'v}\, n^s(\varepsilon_{j',v'} - \varepsilon_j^v)\ \theta(\varepsilon_{j',v'} - \varepsilon_j^v) \\ &+ F_{jj',vv'}\ (1 + n^s(\varepsilon_j{}^v - \varepsilon_{j'}^{v'}))\ \theta(\varepsilon_j^v - \varepsilon_{j',v'})\} \\ &*\theta(1 - |\varepsilon_{j',v'} - \varepsilon_j^v|) \end{aligned} \tag{2.58}$$

where

$$F_{j'j}^{v'v} = \omega_D \frac{24\pi\sigma_0^2}{r^3} \frac{m}{M_s} \frac{v_>!}{v_<!} \frac{1}{(|v-v'|!)^2} \left[\frac{4m_2/m_1}{r\delta_v}\right]^{|v-v'|}$$

$$* \frac{j_>!\Gamma(2\sigma_0-j_>)}{j_<!\Gamma(2\sigma_0-j_<)} (\sigma_0-j'-1/2)(\sigma_0-j-1/2)(j-j')^2$$

$$*\left[(v'-v)\delta_v + \frac{1}{r}(j'-j)(2\sigma_0-j-j'-1)\right]$$

$$*\left[\frac{2\sigma_0-j-j'-1}{2\sigma_0} + \frac{1-2^{-|v-v'|}}{|j-j'|}\right]^2 , \qquad (2.59)$$

$$n^s(\varepsilon) = \left[\exp\left(-\frac{\hbar\omega_D}{k_BT}\varepsilon\right) - 1\right]^{-1} , \qquad (2.60)$$

and $v_>$ ($v_<$) is the larger (smaller) of v,v'. (Similarly for $j_>$ and $j_<$) We have scaled all energies by the Debye energy $\hbar\omega_D$, and defined

$$\varepsilon_j^v = E_j^v/\hbar\omega_D \quad \text{and} \quad \delta_v = \Omega/\omega_D . \qquad (2.61)$$

The surface potential is described by the dimensionless parameters,

$$\sigma_0 = \left(\frac{2mV_0}{\hbar^2\gamma^2}\right)^{1/2} \quad \text{and} \quad r = \frac{2m\omega_D}{\hbar\gamma^2} . \qquad (2.62)$$

Here, σ_0 is approximately equal to the number of bound states in the surface potential with range described now by r.

The general features of the transition rate given in (2.58) may be simply understood. The first term in (2.58) corresponds to absorption of a single phonon from the solid, while the second refers to spontaneous or stimulated emission of a phonon to the solid. These

processes are possible provided the molecule state energy difference is less than the maximum phonon frequency, i.e., $|\varepsilon_j{}^{v'} - \varepsilon_j{}^{v}| < 1$. Note that the transition rates decrease rapidly as $|v - v'|$ increases because of the small factor, $(4m_2/m_1 r\delta_v) << 1$. The collection of gamma functions from the surface potential matrix elements involving j and j' has been shown to strongly favour transitions where j and j' are close, sometimes differing by only one.[83] This encourages a cascade of step by step transitions through the bound states of the surface potential.

(ii) Bound state - continuum transitions

The total phonon-assisted transition rate from a particular bound state (jv) to any continuum state with vibrational index v' is

$$P_{cj}{}^{v'v} = \sum_q P_{qj}{}^{v'v} \tag{2.63}$$

where the surface potential state label q is the (one-dimensional) wave vector of translational motion of the free (desorbed) molecule. Proceeding similarly as in (i), and taking q to be a continuous variable leads to

$$P_{cj}{}^{v'v} = C_j{}^{v'v} \int_{\varepsilon_j{}^{v}-v'\delta_v-1}^{\varepsilon_j{}^{v}-v'\delta_v+1} d\varepsilon\ \theta(\varepsilon)\ W_j{}^{v'v}(\varepsilon)\ (\varepsilon-\varepsilon_j{}^{v}+v'\delta_v) n^s(\varepsilon-\varepsilon_j{}^{v}+v'\delta_v) \tag{2.64}$$

where

$$C_j^{v'v} = \omega_D \frac{3\pi}{4} \frac{m}{M_s} \frac{v_>!}{v_<!} \frac{1}{((v-v')!)^2} \left[\frac{4m_2}{m_1 r \delta_v}\right]^{|v-v'|} \frac{2\sigma_o - 2j - 1}{j!\Gamma(2\sigma_o - j)} ,$$

$$W_j^{v'v}(\varepsilon) = \left|\Gamma(\sigma_o + \frac{1}{2} + i\sqrt{r\varepsilon})\right|^2 \frac{\sinh(2\pi\sqrt{r\varepsilon})}{\cosh^2(\pi\sigma_o) + \sinh^2(\pi\sqrt{r\varepsilon})}$$

$$* \left[\varepsilon + \frac{1}{r}\left[(\sigma_o - j - 1/2)^2 + 2\sigma_o(1 - 2^{-|v-v'|})\right]\right]^{-2} ,$$

and

$$\varepsilon_j^v - v'\delta_v = -\frac{1}{r}(\sigma_o - j - 1/2)^2 + (v-v')\delta_v .$$

The integration variable ε in (2.64) is the kinetic energy of the desorbing molecule, scaled by the Debye energy. Both phonon absorption ($\varepsilon + v'\delta_v - \varepsilon_j^v > 0$) and phonon emission processes ($\varepsilon + v'\delta_v - \varepsilon_j^v < 0$) are contained in (2.64). To see this, note that $-\varepsilon n^s(-\varepsilon) = \varepsilon(1+n^s(\varepsilon))$.

2.4.3 Tunneling to the gas phase

The coupling (H_{res}) between vibrational and frustrated translational motion, when treated as a dynamic perturbation, can cause transitions between degenerate states. Ignoring the unlikely possibility of accidental degeneracy between bound states, i.e., $E_j^v = E_{j'}^{v'}$, H_{res} can cause bound state to continuum transitions only. The tunneling rate to the continuum is

$$Q_{cj}{}^{v'v} = \sum_q \frac{2\pi}{\hbar} \left| \langle qv' \left| V_1(x - \frac{\mu}{m_1}\xi) - V_1(x - \frac{\mu}{m_1}\xi_o) \right| jv \rangle \right|^2 \delta(E_q{}^{v'} - E_j{}^v) \tag{2.65}$$

Expanding the difference in the matrix element above in powers of $(\xi - \xi_o)$ as in (2.55) gives, by a similar calculation to that of Section 2.4.2,

$$Q_{cj}{}^{v'v} = \omega_D r \frac{\pi}{16} \frac{v_>!}{v_<!} \frac{1}{(|v-v'|!)^2} \left[\frac{4m_2}{m_1 r \delta_v}\right]^{|v-v'|}$$

$$\frac{2\sigma_o - 2j + 1}{j!\,\Gamma(2\sigma_o - j)} \left| \Gamma(\sigma_o + \frac{1}{2} + i\sqrt{r(\varepsilon_j{}^v - v'\delta_v)}\,) \right|^2$$

$$* \frac{\sinh(2\pi\sqrt{r(\varepsilon_j{}^v - v'\delta_v)})}{\cos^2(\pi\sigma_o) + \sinh^2(\pi\sqrt{r(\varepsilon_j{}^v - v'\delta_v)})}$$

$$* \left[(v-v')\delta_v + \frac{2\sigma_o}{r}(1 - 2^{1-|v-v'|})\right]^{\mu^2} \theta(\varepsilon_j{}^v - v'\delta_v) \,. \tag{2.66}$$

Although we express this transition rate in terms of the parameters ω_D and r for convenience, no phonons are involved in this direct tunneling process between vibrational and surface bond states.

This completes the lowest order calculation of the transition rates, which is to first order in H_{int} for the transition amplitudes, or to second order for the transition rates. The off-diagonal bound state to bound state transition rate matrix elements that enter the master equation (2.1) are

$$R_{j'j}{}^{v'v} = L_{j'j}{}^{v'v} + P_{j'j}{}^{v'v} \,, \tag{2.67}$$

and the transitions to the gas phase (continuum) are

$$R_{cj}^{v'v} = P_{cj}^{v'v} + Q_{cj}^{v'v} . \tag{2.68}$$

2.5 Solution of the Master Equation

2.5.1 Direct numerical solution

To study desorption behaviour, we will follow the time evolution of the adsorbate, given by the solution of the master equation,

$$\frac{d}{dt} n_j^v(t) = \sum_{j'=0}^{j_{max}} \sum_{v'=0}^{v_{max}} R_{jj',vv'} n_{j',v'}(t) \tag{2.1}$$

subject to the initial conditions

$$n_j^v(0) = e^{-E_j^v/k_BT} \Big/ \sum_{j,v} e^{-E_j^v/k_BT} . \tag{2.69}$$

Initially in thermal equilibrium, the state occupation $n_j^v(0)$ is given by the Boltzmann distribution above. The gas molecules obey classical statistics in the low coverage and low gas pressure situation considered here.

We follow the method of reference 14 and solve (2.1) by inverting the matrix, $R_{jj',vv'}$, which has eigenvalues, λ_i, and eigenvectors, e_{jv}^i. The adsorbate population, N(t), during the desorption process is then

given, using basic linear algebra, by

$$\frac{N(t)}{N(0)} = \sum_{jv} n_j^v(t) = \sum_i s_i \, e^{\lambda_i t} \quad \text{where Re } \lambda_i < 0 \tag{2.70}$$

where

$$s_i = \sum_{jv} n_j^v(0) \, \bar{e}_{jv}^i \sum_{j'v'} e_{j'v'}^i \, ,$$

and

$$\sum_{jv} \bar{e}_{jv}^i \cdot e_{jv}^{i'} = \delta_{ii'}$$

defines $\bar{e}_{jv}^i$. In practice, we find that one real, negative eigenvalue, λ_0, is much smaller in magnitude than all the rest, that is, $|\lambda_0| << |\text{Re } \lambda_i|$ for all $i \geq 1$. Furthermore, the corresponding prefactor, s_0, is typically much larger than all the rest $\Rightarrow s_0 = 1 >> |s_i|$ for $i \geq 1$.

This separation of timescales leads to two regimes of physical behaviour. When the laser is first turned on, there is a very short transient period during which the occupation functions, $n_j^v(t)$, evolve from their initial values to a new, laser driven, quasi-stationary state. Negligible desorption occurs during this very short initial phase in which many timescales $\{\lambda_i^{-1}\}$ in (2.70) are present. Since $R_{jj'}^{vv'}$ is not symmetric, some of these rapid transients may even exhibit a strongly damped oscillatory behaviour characterized by

$\mathrm{Im}\lambda_i \neq 0$.

Once the initial transients have died, the adsorbate population then decays exponentially with a single timescale (t_d) according to

$$\frac{N(t)}{N(0)} = s_o e^{\lambda_o t} = e^{-r_d t} \quad \text{for} \quad |\mathrm{Re}\ \lambda_i| t \gg 1 \quad (i \geq 1) \tag{2.71}$$

The desorption rate ($r_d = t_d^{-1}$) is thus identified with the smallest eigenvalue of the rate matrix,

$$r_d = |\lambda_o| \ . \tag{2.72}$$

Experimentally, one measures the desorption yield (Y) defined to be the number of molecules that desorb during the duration (t_L) of a laser pulse. In our model, the yield is given by

$$Y = N(0) - N(t) \tag{2.73}$$

where N(0) is the number of adsorbed molecules initially exposed to the laser beam. Since $|\mathrm{Re}\ \lambda_i|\ t_L \gg 1$ for $i \geq 1$ for typical adsorption systems, we have

$$Y = N(0)\ [1 - e^{-r_d t_L}] \ ,$$

and approximating further,

$$Y = N(0)\, r_d\, t_L \quad \text{provided} \quad r_d\, t_L \ll 1 \,. \tag{2.74}$$

In summary, we typically find a separation of timescales

$$\begin{array}{ccccc} \text{transient time} & \ll & \text{laser pulse time} & \ll & \text{desorption time} \\ (|\mathrm{Re}\ \lambda_i|^{-1},\ i \geq 1) & & (t_L \sim 10\text{-}100\ \text{nsec}) & & (t_d = |\lambda_0|^{-1}) \end{array} \tag{2.75}$$

which leads to a small yield per laser pulse that is proportional to the desorption rate, according to (2.74).

The matrix inversion leading to $\{s_i\}$ and $\{\lambda_i\}$ in (2.70) is accomplished by a lengthy numerical computation. The quantity of interest - the desorption rate r_d - is then studied as a function of the experimental system parameters, as outlined in Section 2.6.

2.5.2 Approximate analytic solution

It is also possible to obtain an approximate, analytic solution of the master equation for photodesorption, by making judicious use of the wide range of time scales included in the rate matrix. An approximate formula for the desorption rate is desirable in an effort to reduce the computational complexity involved in the straightforward matrix inversion method described above. Furthermore, computational innaccuracy due to round-off errors prevents us from applying the matrix inversion method to predict very slow desorption behaviour. Reduction of the master equation (2.1) has been previously accomplished by using approximate ansatzes. At low enough laser intensities, it is valid to approximate $n_j^v(t) = \exp(-\beta E_j)\, n_v(t)$ which, on substitution into (2.1)

gives a master equation in the v-states only.[64] This method assumes that the surface bond (j) states are in thermal equilibrium. At very high laser intensities, all vibrational levels are equally occupied in saturation, and the ansatz $n_j^v(t) = n_j(t)$ may be used to eliminate the v-states from the master equation.[65] However, photodesorption experiments are generally performed at intermediate intensities between these two extremes. A diagrammatic approximation method used by Hill[66] to find the steady state solution of a system of linear rate equations is employed here to predict desorption rates accurately at all laser intensities.

The photodesorption process described by the master equation (2.1) consists of a short transient phase followed by a long kinetic phase during which desorption occurs, as given by equation (2.75). It is just the latter phase in which we are interested here. Although photodesorption is a dynamic process, the molecular occupation functions $n_j^v(t)$ are quasi-stationary during the kinetic phase for times $t_{trans} \ll t \ll t_d$. This is so because the final transition rates from bound surface bond states j to continuum (gas phase) states, $P_{cj}^{v'v} + Q_{cj}^{v'v}$, are generally slower than bound state-to-bound state transitions out of the state (j,v) and thus make a minor contribution to the calculation of $n_j^v(t)$ for $t \ll t_d$. (Actually, $P_c + Q_c$ do affect $n_j^v(t)$ significantly for j near the top of the surface potential well. While these high j-states are crucial in thermal desorption, they play a smaller role in the more efficient photodesorption process.) We therefore calculate the steady state occupation functions n_j^v with the bound state-to-continuum transition rates, $P_{cj}^{v'v} + Q_{cj}^{v'v}$, omitted. The desorption rate during the kinetic phase is then given by

$$r_d = \left[\sum_{j,v} n_j^v \left[\sum_{v'} \left(P_{cj}^{v'v} + Q_{cj}^{v'v} \right) \right] \right] \Bigg/ \sum_{j,v} n_j^v \, . \qquad (2.76)$$

The denominator is included above to correctly normalize the desorption rate per adsorbed molecule.

The calculation of the steady state populations n_j^v is essentially equivalent to inverting the rate matrix as done numerically in the last section, but with the transitions to the continuum omitted. A diagram method devised by Hill to accomplish this task is now outlined. Only the recipe is given here; details and proofs may be found in references 66 and 67. The first step is to construct all "partial diagrams" for the given reaction system. A partial diagram has a vertex for every state of the system and the maximum possible number of lines drawn between these states without resulting in any closed loops. The lines represent allowable transitions between states. "Directional diagrams" for a given state are then constructed by putting arrows onto the partial diagrams in such a way that all (connected) paths flow toward and end at the given state. Each arrow between two states, $jv \rightarrow j'v'$, on such a diagram represents a corresponding transition rate, $R_{j'j}^{v'v}$. A directional diagram is assigned a value given by the product of these rate constants. The relative steady state occupation n_j^v of the state (j,v) is then given by the sum of all directional diagrams for that state. To obtain the absolute occupations, one must divide by a normalization factor equal to the sum of all directional diagrams of all states, i.e., $\sum_{jv} n_j^v$. This

procedure is now applied to the photodesorption system. A physical interpretation of the diagrammatic results will then be discussed.

Since it is impractical to draw all directional diagrams for a typical photodesorption system which has ≈ 100 relevant states, it is essential that the most significant diagrams be considered in a systematic way. For this purpose we utilize a natural hierarchy among the transition rate scales appearing in the master equation, summarized below. (The arrows below the rates show how they appear in Fig.2.6 of the next section and in the directional diagrams to follow.)

$$P_{j'<j}^{vv} > P_{j'>j}^{vv} > P_{j'j}^{v\pm1v} > L^{v\pm1v} \qquad (2.77)$$

The fastest rates of all are phonon emitting transitions $P_{j'<j}^{vv}$ downwards to lower j-states in a given surface potential well in Fig. 2.6. These transitions do not change the vibrational index v. Considerably slower at low temperatures where $k_BT < (E_{j+1}-E_j)$, are thermally activated transitions $P_{j'>j}^{vv}$ upwards in a given surface potential well. Provided the j-states that contribute most to photodesorption are well separated in energy, the separation of timescales given above is very good. Slower still are phonon-assisted transitions $(j,v) \rightarrow (j',v\pm1)$ that involve tunnelling between vibrational and surface bond states. These processes are represented by horizontal lines between adjacent surface wells in Fig. 2.6. Note that direct transitions such a $v \rightarrow v\pm2$ are negligibly slow and are thus ignored. The slowest transition rates of all is the laser-assisted vibrational (de) excitation rate $L^{v\pm1v}$, represented by diagonal lines $v \rightarrow v\pm1$ in Fig. 2.6. Only at saturation does $L^{v\pm1v}$ become equal in magnitude to the

tunnelling rates $P_{jj'}^{v\pm1v}$. The largest directional diagrams are those in the maximum possible number of the fastest rates - $P_{j'<j}^{vv}$. The slower rates involving vibrational transitions - $P_{jj'}^{v\pm1v}$ and $L^{v\pm1v}$ - are included in minimal numbers.

Let us first consider the directional diagrams shown in Fig. 2.5a for the molecular ground state (j,v) = (0,0), which at low temperatures and laser intensities is the most heavily occupied. Summing over the indices i and i' in the diagrams in the figure gives the contribution to n_o^o,

$$\left[\prod_{i=1}^{i_{max}} P_{i-1i}^{oo}\right] \sum_{i=0}^{i_{max}} \left[(L^{01} + \sum_{i'=0}^{i_{max}} P_{i'i}^{01}) \right.$$

$$\left. * \left(\prod_{j=i+1}^{i_{max}} P_{j-1j}^{11} + \delta_{i,i_{max}}\right)\left(\prod_{j=1}^{i} P_{jj-1}^{11} + \delta_{i,0}\right)\right] .$$

Each product in the sums above has only one slow transition rate from v = 1 → 0. Diagrams with a few thermally activated transitions (j-1 → j) are necessary because the tunnelling rates $P_{j'j}^{01}$ increase somewhat with j. For high j-states, many downward transition rates $P_{j'<j}^{oo}$ besides the j → j-1 transition are important. Additional diagrams taking this into account are included by replacing P_{j-1j}^{01} above with

$$\gamma_j = \sum_{j'=0}^{j-1} P_{j'j}^{oo} \quad \text{for} \quad j > 0 . \tag{2.78}$$

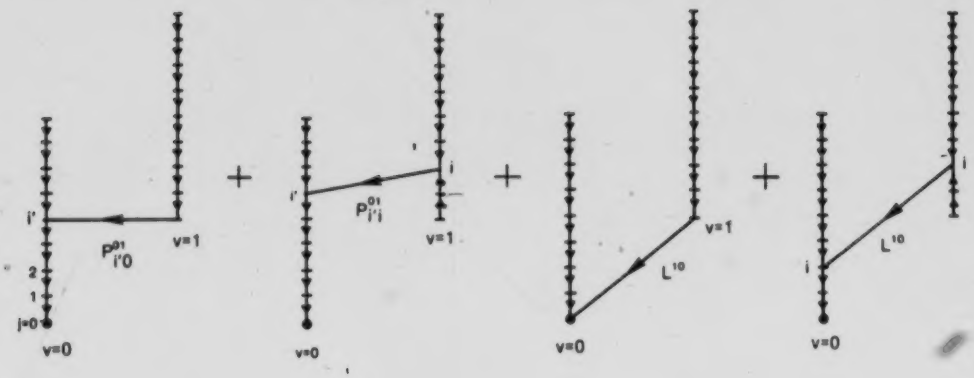

Fig.2.5(a). Some directional diagrams for the ground state (j=0,v=0) for v_{max}=1.(j-states are shown equally spaced for convience only!)

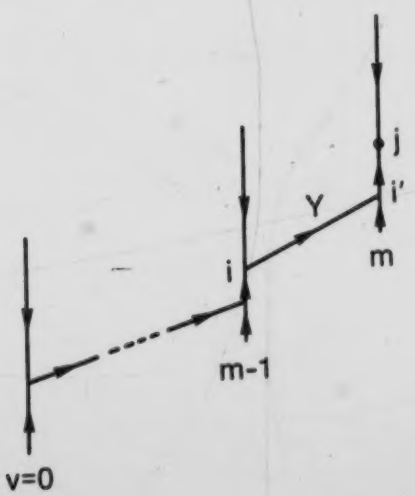

Fig.2.5(b). Diagrams for (j,v_{max}). The horizontal lines represent rates $P_{i'i}^{v'v}$ or $L^{v'v}$, and vertical lines contain rates $P_{j'j}^{vv}$.

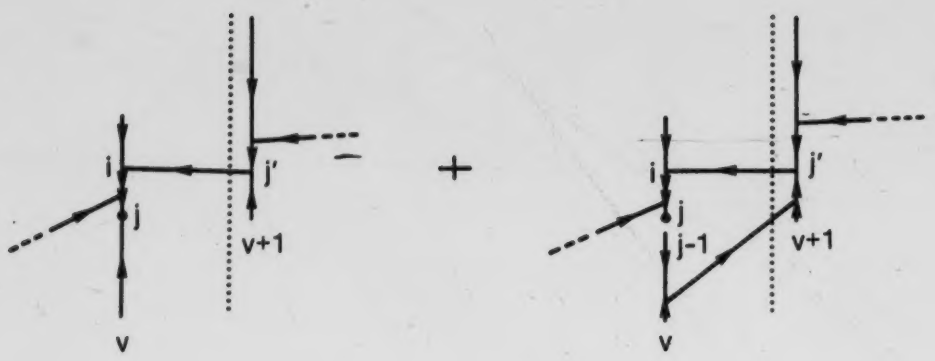

Fig.2.5(c). Relating n_j^{ν} to $n_{j'}^{\nu+1}$. The dotted vertical line delineates the upper (right-hand) diagram parts that are related to $n_{j'}^{\nu+1}$ by (2.86).

Furthermore, detailed balance gives

$$\prod_{j=1}^{i} P_{jj-1}^{\nu\nu} = e^{-\Delta_i} \prod_{j=1}^{i} P_{j-1j}^{\nu\nu} = e^{-\Delta_i} \prod_{j=1}^{i} \gamma_j$$

where $\Delta_j = \beta(E_j - E_o)$. The final, approximate relationship given above is valid for

$$e^{-\Delta_j} \ll 1 ,$$

as is typically the case for the small i that are significant here. Combining these results and extending the diagrams to $\nu_{max} = m$ gives the un-normalized occupation function

$$\bar{n}_o^{\circ} = (DX)^m \, D \, m! \, , \tag{2.79}$$

where we define

$$D = \sum_{i=1}^{i_{max}} \gamma_i \tag{2.80}$$

and

$$X = \sum_{i=0}^{i_{max}} \left[\left[\sum_{i'=0}^{i_{max}} P_{i'i}^{01} + L^{01} \right] e^{-\mu \Delta_i} \right] \tag{2.81}$$

The m! factor in n_o° arises because $P_{ii'}^{v-1v} = vP_{ii'}^{01}$ and $L^{v-1v} = vL^{01}$. The factor D represents transitions $i \to i'$ while X represents $v \to v-1$ transitions.

The occupation function n_j^v of lower vibrational levels will be deduced afterwards. A general class of directional diagrams for the state (j,m) is shown in Fig. 2.5b, leading to the unnormalized occupation function,

$$\bar{n}_j^m = (DY)^m \, D \, e^{-\mu \Delta_j} \, m! \tag{2.82}$$

where

$$Y = \sum_{i=0}^{i_{max}} \left[\left[\sum_{i'=0}^{i_{max}} P_{i'i}^{10} + L^{10} \right] e^{-\Delta_i} \right] . \qquad (2.83)$$

Directional diagrams with additional cross-paths $v \rightarrow v\pm1$ must have fewer fast, downward rates $P_{j'<j}^{vv}$, and are thus negligible, according to (2.77). Note that the occupation probability of the vibrationally excited state (j=0, v=m) is smaller than that of the ground state (j=0, v=0) by a factor $(Y/X)^{\overline{m}}$. Vibrational transitions $v \rightarrow v+1$, due to both phonon and photon assisted processes, are included in Y above. At low enough temperatures and intensities, nearly all adsorbed molecules are confined to the ground state, j=0, v=0. It is therefore convenient to define partially normalized occupation probabilities,

$$n_j^v = \bar{n}_j^v / \bar{n}_o^o . \qquad (2.84)$$

Dividing (2.82) by (2.79) gives

$$n_j^m = \left(\frac{Y}{X} \right)^m e^{-\Delta_j} . \qquad (2.85)$$

We now derive a relation between the occupation functions n_j^v and $n_{j'}^{v+1}$. First, we observe that the most significant directional diagrams for $n_{j'}^{v+1}$ must give the factor $(v+1)!(DY)^{v+1}$ from diagram parts linking the v=0 to v+1 states, in analogy with the calculation of n_j^m above. Regardless of the form of the diagram parts in n_j^{v+1} connecting vibrational levels v+1 to m, the cross-rates $(P_{i'i}^{v+1v} + L_{i'i}^{v+1v})$ in Y can connect into any surface bond level i' of the vibrational

state v+1. The directional diagrams for the state (j',v+1) are thus of the form

$$n_{j'}^{v+1} = (v+1)!(DY)^{v+1} \times (\text{upper diagram parts directed into } (j',v+1)) . \quad (2.86)$$

Diagrams relating n_j^v to $n_{j'}^{v+1}$ are shown in Fig. 2.5c. The first term, with a minimum of slow cross-rates, represents thermal effects, while the second diagram with an extra cross-path includes laser-induced vibrational excitation. In both cases, the undrawn upper diagram parts are directed into the state (j',v+1), and are related to the occupation function n_j^{v+1} according to equation (2.86). Using this fact, the directional diagrams in Fig. 2.5c give

$$n_j^v = \sum_{j'=0}^{i_{max}} f_{jj'}^{v} \, n_{j'}^{v+1} \quad (2.87a)$$

where

$$f_{jj'}^{v} = e^{-\Delta_j} Y^{u_1} \left[\sum_{i=0}^{i_{max}} P_{ij'}^{01} + L^{01} \right] + (v+1) \frac{Y_j}{\gamma_j} Y^{u_1} \sum_{i=j}^{i_{max}} P_{ij'}^{01}, \quad (2.87b)$$

with

$$Y_j = \sum_{i=0}^{j-1} \left[\left(\sum_{i'=0}^{i_{max}} P_{i'i}^{10} + L^{10} \right) e^{-\Delta_i} \right] \quad \text{for } j > 0 \qquad (2.88)$$

and

$$Y_j = 0 \quad \text{for } j = 0 \, .$$

Since the right-hand diagram in Fig. 2.5c exists only for $j > 0$, the second term in (2.87b) is set to zero if $j = 0$.

By repeated use of the recursion formula (2.87) on (2.85), it is straightforward to (numerically) compute the occupation functions n_j^v for all vibrational levels. Substitution into (2.76) gives the properly normalized desorption rate. This computational method reproduces the exact matrix inversion results very well in almost all cases, and is used to obtain the theoretical data presented in Section 7. Inaccuracies are encountered at extremely high intensities above $10^9 MW/cm^2$ where condition (2.77) is violated, and the method fails if the phonon-assisted rates between adjacent vibrational levels is cut off.

The steady state occupation probabilities calculated in this way can be easily interpreted physically in the low temperature ($k_B T << E_j - E_{j-1}$) and moderate intensity ($L^{10} << P_{j0}^{01}$) limit. Photodesorption experiments are typically done in this (sub-saturation) intensity regime, but sometimes at somewhat higher temperatures. In the limits given above, equations (2.87) and (2.85) combine to give the occupation probability for excited vibrational states $j = 0$, $v > 0$ as

$$n_0^v = \left(\frac{Y}{X}\right)^v = \left[\frac{L^{10}}{\sum_{i'} P_{i'0}^{01} + L^{01}}\right]^v . \qquad (2.89)$$

Step-wise vibrational excitation at the rate L^{10} competes with vibrational decay processes assisted by phonons ($P_{i'0}^{01}$) and photons (L^{01}) in populating higher vibrational levels. Similarly, for low surface bound states j such that $E_j - E_0 < \hbar\Omega$ (= vibrational spacing), the occupation probabilities are

$$n_j^v = \left(\frac{Y}{X}\right)^v \left(e^{-\Delta_j} + (v+1)\,\frac{Y_j}{\gamma_j}\,\frac{X_j}{X}\right)$$

$$= n_0^v \left(e^{-\Delta_j} + \frac{L^{v+1,v}}{\gamma_j}\right) \text{ for } j > 0 . \qquad (2.90)$$

Occupation of excited surface bond states can be induced by either thermal or laser-assisted processes, corresponding to the first and second terms in (2.90), respectively. The second term arises from photon-absorption processes exciting the $v \to v+1$ transition, followed by phonon-assisted tunnelling back to excited j-states at the vibrational level v. The molecule then cascades downwards in the surface potential well, stopping at each state for an average time given by γ_j^{-1}. This process, which is responsible for the non-thermal occupation of excited surface bond states, is shown in Fig. 3.2 of the next chapter in connection with resonant surface heating. It is emphasized that the occupation probability n_j^v for higher j-state is generally considerably more complicated than the simple form given in (2.90), and

formulae (2.85) and (2.87) must then be evaluated in full.

2.6 Early Results - Theory and Experiment

2.6.1 Theoretical model results

The dynamics of the photodesorption model just described are now examined, before making a comparison with experimental results obtained by Heidberg et al. We now apply the theory to a model gas-solid system. The system parameters are chosen to model the physisorption of CH_3F on an NaCℓ (100) surface, insofar as the experimental parameters are known.[21,22] The CH_3F molecule is assumed to adsorb with the F atom closest to the surface and the CH_3 complex sticking outwards. (The laser excites the ν_3 vibrational mode, corresponding to a stretching of the C-F bond.) The system is characterized by

i) the internal vibrational frequency (Ω = 970 cm^{-1}) and linewidth ($\Gamma_V \leq$ 20 cm^{-1} FWHM) of the adsorbed molecule, and its atomic masses (m_1,m_2), and effective change (q = 1 el.ch.)*,

ii) the depth (V_0 = 22.5 kJ/mole) and range (γ^{-1} = 0.3 Å) of the surface potential,

iii) the dielectric constant (n_r), molecular mass (M_S), and Debye temperature (T_D = 281 K) of the solid, and

iv) the laser intensity (I), linewidth (Γ_ℓ < 1 cm^{-1}), pulse duration

---

*The effective charge, Q, is related to the dynamic dipole moment, μ_{dyn}, of the molecular vibration by

$$\mu_{dyn} = Q\sqrt{\hbar/2\mu\Omega} \qquad (2.92)$$

where μ on the right hand side is the reduced mass of the molecule.

(t_L = 200 nsec), and angle of incidence (θ = 60°). (2.91)

(Note that we replaced V_o, γ^{-1}, and T_D with σ_o, r, and ω_D in the rates calculated in the last section.)

The molecular and solid parameters (i and iii above) are generally all known, with the exception of Q and Γ_v. The effective change, Q, is estimated from the infrared absorption peak intensity for the adsorbed molecule which is known to within an order of magnitude for $CH_3F/NaC\ell$.[68] The observed infrared absorption linewidth may in general receive contributions from both homogeneous and heterogeneous sources, and thus sets only an upper limit on the homogeneous vibrational width, Γ_v. (Photodesorption from an inhomogeneous adsorbate is considered in Section 6.) Errors in Q and Γ_v, however large, will affect our results by simply rescaling the laser intensity dependence of the desorption rate.

There is also some uncertainty in describing the surface potential. The well depth (V_o) can be roughly equated to the isosteric heat of adsorption, determined from equilibrium adsorption measurements. The range, γ^{-1}, of the potential is not so easily determined experimentally, and is unknown for CH_3F on $NaC\ell$. We have therefore assigned a reasonable value, γ^{-1} = 0.3 Å, for our model analysis. These surface potential parameters translate into the dimensionless variables, σ_o = 18.6 and r = 35.7.

The surface potential for this model system develops 19 bound states representing frustrated translational motion. The energy spacing between adjacent surface bond states is always less than one Debye energy, so purely thermal desorption via one-phonon processes is possible. A molecule in the surface ground state (j = 0) needs a min-

imum vibrational excitation of v = 2 to bring its total energy positive, into degeneracy with the continuum of gas phase states, as shown

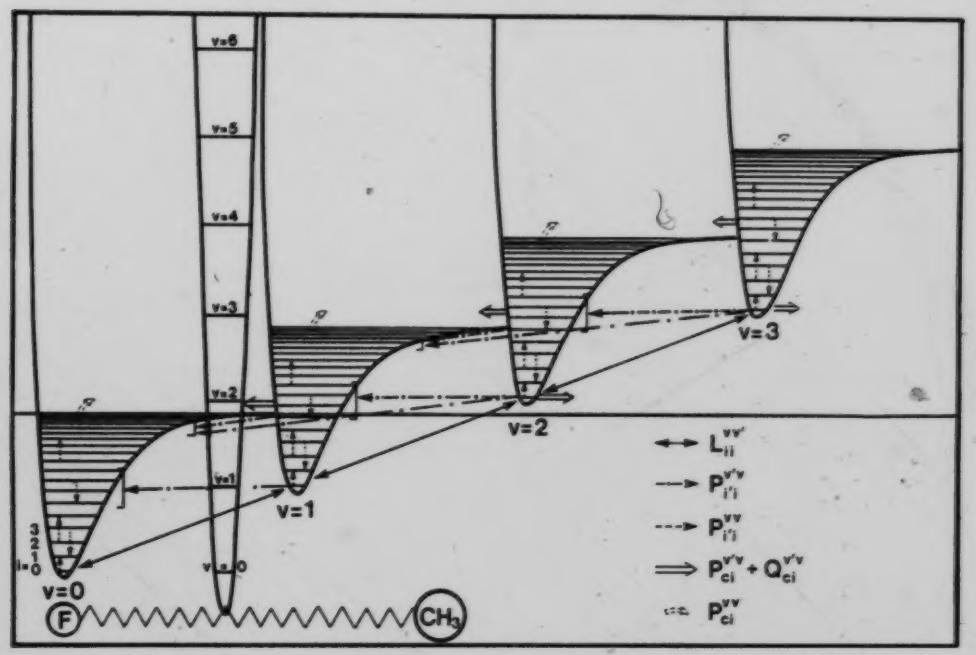

Fig.2.6. Energy level diagram for CH_3F on NaCℓ. Surface potential well corresponding to different vibrational states (v) are transposed laterally for convenience only. Some transition processes included in the theory are indicated by arrows: $P_{i'i}^{v'v}$ indicates phonon-assisted bound state → bound state transitions $(i,v)\rightarrow(i',v')$; $P_{ci}^{v'v}$ and $Q_{ci}^{v'v}$ are phonon-assisted and elastic tunneling rates from bound states to the continuum; $L_{ii}^{v'v}$ represents the laser coupling.

in Fig. 2.6. (We therefore set $v_{max} = 2$ in (2.1) for the calculations in this section. The desorption rate is greatly diminished if we reduce v_{max} below this level. Increasing v_{max} above 2 enhances desorption slightly, but introduces no qualitative differences.)

Using the method described in Sections 2.1 and 2.5, the desorption rate is calculated as a function of laser intensity and temperature. In Fig. 2.7, the desorption rate is plotted as a function of intensity in a log-log graph, for T = 50 and 100 K. The desorption data is red-

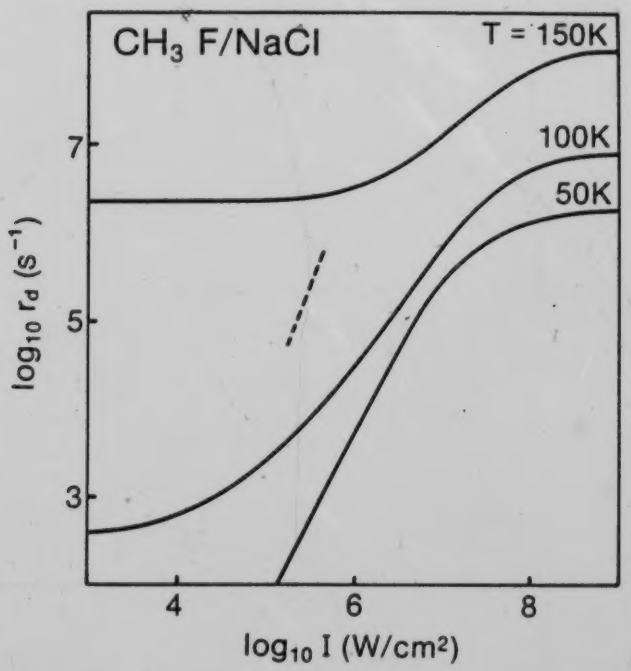

Fig.2.7. Desorption rate versus laser intensity for $CH_3F/NaCl$ at different temperatures. System parameters are given in (2.91). Broken line represents experimental results of reference 21.

isplayed in log rate versus inverse temperature graphs in Fig. 2.8. (Note that a slightly larger potential range, $\gamma^{-1} = 0.37$ Å, is used in this figure.) On the latter graph, we include an estimate for purely thermal desorption, without the laser. This process, relying entirely on phonon-assisted transitions to higher energy levels (j,v), has been considered previously.[14] The thermal desorption graph is a straight

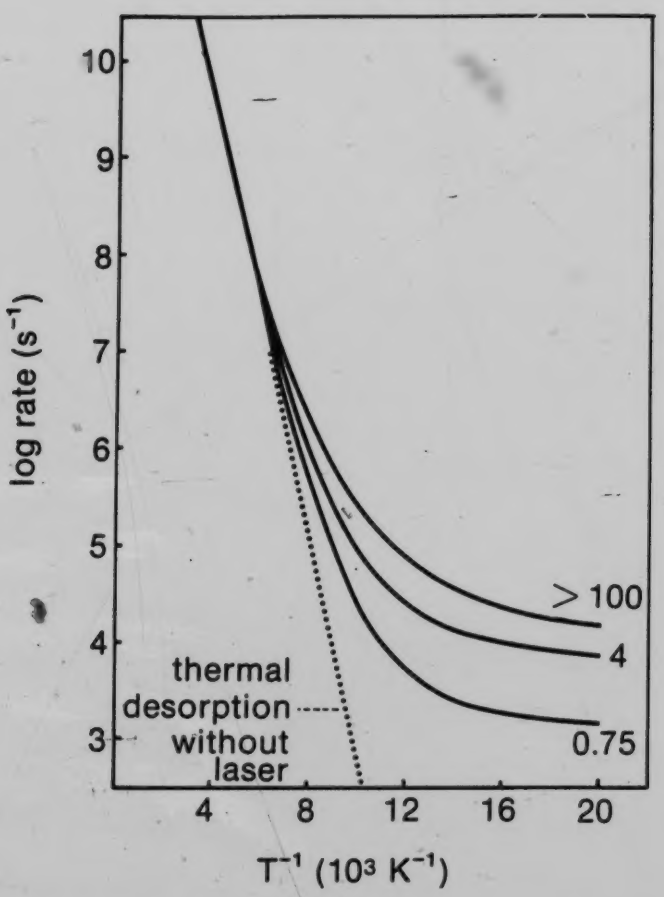

Fig.2.8. Desorption rate versus inverse temperature for $CH_3F/NaCl$ at different laser intensities I[MW/cm²]. The surface potential range is γ^{-1}=0.37Å.

line, indicating an Arrhenius form for the rate

$$r_{des} = \nu\, e^{-E_d/k_BT} . \qquad (2.93)$$

The activation energy, E_d, is approximately equal to the depth of the lowest bound state, $j = 0$, while the prefactor, ν, depends on the microscopic transition rates entering the master equation.

The photodesorption graphs show enhanced desorption rates at low temperatures. At 50 K, the laser enhances the desorption rate by many orders of magnitude over the thermal rate; desorption increases nonlinearly with intensity in Fig.2.7. Note that the T = 150 K graph shows little intensity dependence; thermal desorption dominates in this regime. This behaviour arises from competition between the different (and complex) transition pathways leading to desorption, as seen by examining Fig. 2.6. At high enough temperatures, absorption of thermal phonons by the surface bond leads to vertical transitions $P_{i'>i}^{vv}$, without vibrational (v) excitation. At lower temperatures these processes are less efficient, and then photodesorption may be observed. Photon absorption excites the internal molecular vibration (e.g., v = 0 → 1), represented by the diagonal transitions ($L^{v'v}$) in Fig. 2.6. From an excited vibrational state, the molecule can tunnel (near horizontally) into an excited surface bond state, converting vibrational energy into frustrated translational motion, with absorption or emission of a phonon occuring to conserve energy. (Consider, for example, the (i,v) = (0,1) → (6,0) transition with rate P_{60}^{01}.) This process leads to enhanced occupation of excited surface bond states, j > 0. However, at low temperatures, these states decay rapidly by spontaneous phonon emission ($P_{i'<i}^{vv}$) as the molecule cascades downwards to the bottom of the surface well. This cascade deposits energy into the phonon bath in the surface region, which is considered in more detail in the context of resonant heating in the next chapter.

Alternatively, the molecule may be stepwise excited to higher vibrational levels. From the (i,v) = (0,2) level, the adsorbed molecule is degenerate with gas phase states, and desorption can occur by

the transitions $P_{c0}^{02} + Q_{c0}^{02}$. An often favourable route to desorption is for the molecule to give up its vibrational quanta one at a time, by a near horizontal (tunneling) path such as (i,v) = (0,2) → (6,1) → (continuum,0). The photodesorption rate incorporates contributions from all these photon and phonon-assisted paths, whose individual timescales will be considered in Section 5.

The efficiency of the photodesorption process depends on the depth (V_o) of the surface potential which, along with the vibrational frequency (Ω) determines the energetics of the process. Desorption rates also depend on the potential range (γ^{-1}) which affects the strength of the coupling to the phonons. These effects, discussed in Section 5, make accurate experimental characterization of the adsorption system essential to the theory.

2.6.2 Comparison with experimental results

We will now compare the theoretical results of the last section with the experimental data by Heidberg et al.[21,22] Their measurements on a multilayer adsorbate of CH_3F on an NaCl single crystal at 64 K were discussed in Section 1. At a laser pulse fluence (fluence = intensity x pulse duration) of 200 mJ/cm², a desorption yield of about 0.2 monolayers per pulse is measured. This corresponds to a desorption rate, $r_d = 10^6\ s^{-1}$, at a laser intensity of 1MW/cm². In addition the intensity dependence of desorption is found to follow $r_d \propto I^{\approx 2.7}$.

A comparison with the theoretical model results is shown in Fig. 2.7. The theoretical graph at T = 50 K is displaced from the experimental result to intensities about an order of magnitude larger. This could be due to the inaccuracy in the determination of Q, as discussed

above. On the other hand, if the vibrational linewidth (Γ_v) is attributed partially to inhomogeneous sources (this is likely to be the case), agreement with experiment is slightly improved. The experimental accuracy in making absolute coverage and desorption yield measurements must also be considered in attempting a quantitative comparison.

More importantly, the theory shows a somewhat weaker intensity dependence desorption $r_d \propto I^{1.8}$, as compared to the experimental result, $r_d \propto I^{2.7}$, at moderate laser intensities. We show in Section 5 that a 50% deeper adsorption potential would cause the experimentally observed dependence. Recent experimental work is in support of this possibility.[69] However, for such a deep adsorption well, bound state energies are separated by more than the maximum phonon energy, and a higher order perturbation theory for the transition rates is needed. This is the topic of Section 5. Alternatively, resonant surface heating could assist the photodesorption process, as considered in the next chapter.

Many body effects within the adsorbate, neglected thus far in the theory for low-coverage systems, must be considered, since the experimental systems are at a higher coverage. Specifically, one expects efficient resonant interaction between the vibrational modes of neighbouring adsorbed molecules. Possible effects on the desorption kinetics are discussed in Section 4.

3. Resonant Heating

3.1 Introduction

In this section, an indirect, resonant, laser-stimulated surface heating process is investigated. Previously, in Section 2, a photodesorption mechanism was introduced which was initiated by resonant vibrational excitation of an adsorbed molecule, and which described the selective desorption of that same molecule. The temperature of the substrate was assumed to be constant. However, this process of desorption is quite inefficient energetically. The fraction of the absorbed photon energy that actually ends up in desorbed molecules is typically small, as shown below.

$$\text{efficiency} = \frac{\text{desorption rate x heat of adsorption}}{\text{photon energy absorption rate}}$$

$$= \frac{r_d V_o}{L^{10} \hbar \Omega_\ell} = O(10^{-4}) \qquad (3.1)$$

In fact, most of the absorbed photon energy, which is initially deposited into an adsorbate vibrational mode, decays into the solid. This is shown pictorially in Fig.3.1; the two vibrational decay paths facilitating this process involve (a) indirect, phonon-assisted vibrational damping, and (b) electronic damping, and will be discussed in detail later. The result of this energy flux into the solid is local surface heating. The temperature at the surface is no longer static, as was assumed in Section 2, and modifications to the theory of photodesorption are necessary. A large rise in surface temperature may lead to

enhanced thermal desorption, both of the molecules originally excited by the laser, and of other co-adsorbed species.

The indirect, resonant heating process described here can be observed as a photoacoustic effect.[70] A light pulse directed on a solid induces local surface heating which, because of thermal expansion, generates sound waves in the solid. By detecting these acoustic waves, one can measure the infrared absorption spectrum of adsorbed molecules. The absorbed laser energy eventually spreads, from the surface region, over the whole sample, causing a minute temperature rise that has also been detected in aid of infrared spectroscopy at surfaces.[71] Note that, in this context, one has also to consider the possibility of direct laser-surface heating, which is a non-resonant process. This is easily separated experimentally from the resonant heating effects by studying the laser-frequency dependence either the photoacoustic signal, or in our case, the desorption yield.

In this section, we will first present a full calculation of the photodesorption kinetics, determining explicitly the surface temperature rise throughout the desorption process.[72] Vibrational damping to electronic degrees of freedom will be neglected, as appropriate for an insulating substrate such as NaCl.

Then we will also treat resonant heating effects at a metal surface.[73] To do so, vibrational relaxation mediated by the electronic damping processes must be considered. A dynamic dipole moment of a vibrationally excited physisorbed molecule is coupled to the conduction electrons of the metal. This interaction allows for vibrational relaxation by electron-hole pair excitation near the surface. Assuming no charge transfer between adsorbate and solid, Persson and Pers-

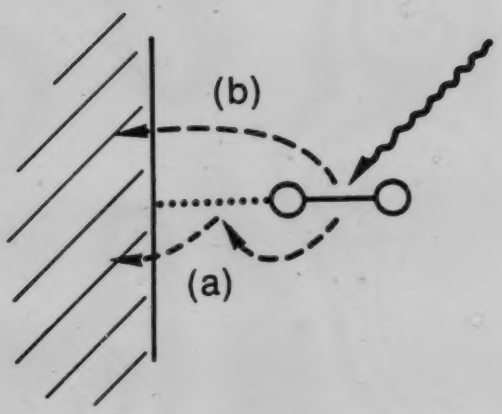

Fig.3.1 Resonant surface heating pathways.
(a) Vibrational damping to phonons of solid via surface bond.
(b) Vibrational damping into metal electrons.

son[74] calculated a decay time for the C-O stretch vibration of the CO/Cu(100) system of $\sim 10^{-10}$sec (see also Brus[75]). By including charge transfer in order to model chemical bonding, they suggest a shorter decay constant of $\sim 10^{-12}$ sec,[76] to match the observed infrared absorption linewidth of 5 cm^{-1}.[77] At a metal surface, vibrational damping can clearly be dominated by this electronic process. To treat resonant heating effects on a metal, we include such relaxation processes phenomenologically in a simplified desorption model. These results are compared with experimental observations for both single and multi-species adsorbed.

3.2 Theory

The photodesorption model presented in Section 2 is now generalized to include resonant heating effects.[72] Recall that the master equation (2.1) contains transition processes (2.58) involving phonon absorption and emission, $P_{j'j}^{v'v}$, which depend on the substrate surface temperature. Since these processes transfer energy between the adsorbate and substrate, they may disturb the thermal equilibrium in the surface region of the solid during a desorption experiment. This latter effect, while ignored in the last section, can be understood in terms of the microscopic transition cycle shown in Fig. 3.2. Upon absorption of an infrared photon from the laser, the (cold) adsorbed molecule is lifted out of the ground state to a vibrationally excited state; $v = 0 \rightarrow 1$. The molecule then undergoes a rapid tunneling transition, P_{00}^{01}

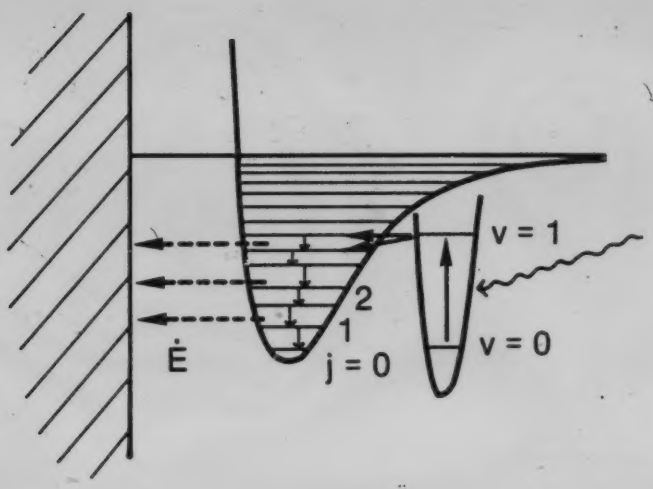

Fig.3.2. Resonant heating cycle.

for example, which converts vibrational energy to frustrated translational motion. The latter is then efficiently damped at low temperatures, that is, for $k_BT \ll \hbar\Omega$. This occurs via phonon emitting transitions such as $j \to j - 1$ as the molecule cascades downwards, to end up again in its ground state $(j,v) = (0,0)$.

The effect of this repeated cycle is to provide an energy flux into the surface given by

$$\dot{E} = N_a \sum_{p\sigma} \hbar\omega_{p\sigma} \frac{dn_{p\sigma}}{dt} \text{ (per unit surface area)} \tag{3.2}$$

where N_a is the adsorbate concentration on the surface; $n_{p\sigma}$ and $\omega_{p\sigma}$ are the occupation function and frequency respectively, of the phonon mode (p,σ). In equilibrium, we have

$$n_{p\sigma}^{eq} = (e^{\hbar\omega_{p\sigma}/k_BT} - 1)^{-1} \tag{3.3}$$

The phonon occupation function $n_{p\sigma}$ increases whenever an adsorbed molecule makes a transition from an initial state with energy E_i^v to a final state with lower energy $E_{i'}^{v'}$, emitting a phonon of energy $\hbar\omega_{p\sigma} = E_i^v - E_{i'}^{v'}$. On the other hand, $n_{p\sigma}$ decreases whenever the reverse transition, involving phonon absorption, takes place. Specifically, we have

$$\frac{dn_{p\sigma}}{dt} = \sum_{iv} \sum_{i'v'} em_{R_{i'i}^{v'v}}(p,\sigma) n_i^v(t)$$

$$- \sum_{iv} \left[\sum_{i'v'} \text{abs}_{R_{i'i}^{v'v}(p,\sigma)} + \sum_{q,v'} \text{abs}_{R_{qi}^{v'v}} \right] n_i^v(t) \qquad (3.4)$$

where q runs over continuum surface bond states. $R_{i'i}^{v'v}(p,\sigma)$ is the transition probability per unit time for the molecular transition $(i,v) \to (i',v')$, accompanied by either emission or absorption of a phonon of momentum p and polarization σ. Energy conservation, $E_i^v - E_{i'}^{v'} = \pm \hbar\omega_{p\sigma}$, allows us to express the energy flux (3.2), using (3.4), in terms of the $P_{i'i}^{v'v}$ transition rates as

$$\dot{E}(t) = N_a \sum_{iv} n_i^v(t) \left[\sum_{i'v'} (E_i^v - E_{i'}^{v'}) P_{i'i}^{v'v} + \sum_{q,v'} (E_i^v - E_q^{v'}) P_{qi}^{v'v} \right] \qquad (3.5)$$

where we normalize $\sum_{iv} n_i^v(0) = 1$. At low coverage, the heat flux is proportional to the adsorbate concentration, N_a, on the surface, because each molecule contributes independently.

The effect on the solid of the phonon emission and absorption processes, $R_{i'i}^{v'v}(p,\sigma)$, is to force the phonon occupation functions $n_{p,\sigma}(t)$ out of equilibrium due to (3.4). However, relaxation processes within the solid tend to rapidly restore local thermal equilibrium conditions. The phonon system equilibriates on the timescale of phonon lifetimes, which are much shorter than the times over which heating occurs, as we shall see later in hindsight. As a result,

local equilibrium conditions are maintained in the surface region. The energy distribution in the solid may then be described by a space and time-dependent temperature field, T(r,t), which varies little over distances of the order of the phonon mean free path and over times of the order of the phonon relaxation time. In this case, the temperature field obeys the heat equation[78]

$$\frac{\partial T}{\partial t} - \chi \nabla^2 T = 0 \tag{3.6}$$

with a radiative boundary condition describing the heat flux at the surface,

$$\frac{\partial T}{\partial z}\bigg|_{z=0} = \frac{\dot{E}(t)}{\lambda} \tag{3.7}$$

Here, λ is the thermal conductivity of the solid and χ is the thermal diffusivity. For a surface with no lateral variation, $T(r,t) = T(z,t)$.

3.2.1 Exact solution[72]

To calculate the resonant heating effect in photodesorption, we must solve the heat equation (3.6) with boundary condition (3.7). However, the energy flux $\dot{E}(t)$, given by (3.5), depends on the molecule occupation functions, $n_i^v(t)$. To determine $n_i^v(t)$, we must solve the master equation (2.1) which is

$$\frac{d}{dt} n_i^v(t) = \sum_{i'v'} R_{ii'}^{vv'}(T(0,t)) n_{i'}^{v'}(t). \tag{3.8}$$

However, now the transition rates $R_{ii'}^{vv'}$ depend on the surface temperature, T(0,t), and thus evolve themselves with time. We must therefore solve the coupled set of equations (3.6) to (3.8) simultaneously, giving both the adsorbate state populations and the temperature distribution in the solid as a function of time.

Equation (3.6) may be solved by standard Green's function techniques[79] for a semi-infinite homogeneous solid (z>0) with boundary condition (3.7) at z = 0 to give

$$T(z,t) = \frac{1}{2\sqrt{\pi\chi}} \int_{-\infty}^{\infty} dz' \left[e^{-(z-z')^2/4\chi(t-t_0)} + e^{-(z+z')^2/4\chi(t-t_0)} \right] \frac{T(z',t_0)}{(t-t_0)^{1/2}}$$

$$+ \frac{V_m}{C_v} \frac{1}{\sqrt{\pi\chi}} \int_{t_0}^{t} dt' \, e^{-z^2/4\chi(t-t')} \frac{\dot{E}(t')}{(t-t')^{1/2}} \tag{3.9}$$

Here C_v is the specific heat per mole and V_m is the molar volume of the solid; z is the distance into the solid. The first term describes the relaxation of a nonuniform temperature distribution, $T(z',t_0)$, while the second term explicitly includes the dissipation of the external energy flux, $\dot{E}(t')$. An iterative numerical procedure is used to solve (3.8) and (3.9) together. At a sequence of discrete times, t_i where i = 0,1,..., we consider the temperature profile, $T(z,t_i)$, and the

molecular occupation functions, $\{n_j^v(t_1)\}$. Initially, we have a uniform temperature distribution, $T(z,t_o) = T_o$, and thermal occupation functions $n_j^v(t_o=0)$ given by (2.69). Assuming $T(z,t_o)$ is nearly constant over the time interval $t_o \to t_1$, we solve the master equation (3.8) which yields

$$n_j^v(t) = \sum_k A_{j,k}^v(t_o)\, e^{-\lambda_k(t_o)(t-t_o)} \quad \text{for } t_o < t < t_1 . \tag{3.10}$$

(The coefficients $A_{j,k}^v$ and eigenvalues λ_k depend on the conditions at t_o.) We then let the adsorbate evolve according to (3.10) from t_o to t_1, to give $n_j^v(t_1)$ and, via (3.5), $\dot{E}(t_1)$. To calculate $T(z,t_1)$, we take $\dot{E}(t') = \dot{E}(t_o)$ over the interval $t_o < t' < t_1$ in equation (3.9). This procedure is then iterated to follow the evolution of the adsorbate population and the temperature field in the solid with time. The adsorbate population

$$N(t) = N(0) \sum_{jv} n_j^v(t) \tag{3.11}$$

no longer obeys a simple exponential decay law because the surface temperature is changing with time throughout the desorption process. In practice, we define the desorption time, t_d by

$$N(t_d) = N(0)\, e^{-1} \tag{3.12}$$

Choosing time steps, $t_{i+1} - t_i < 0.1\ t_d$, we determine the desorption time with sufficient accuracy.

Applying this procedure for the adsorption system CH_3F on NaCl, using the model parameters given in Section 2.6.1 (except where noted), gives desorption and temperature behaviour shown in Figs. 3.3 to 3.5.* The non-exponential decay of the adsorbate population over the desorption process is graphed in Fig.3.3. For reference, an exponential curve fitted to the initial slope, or initial desorption rate $t_d(0)^{-1}$, is shown as a dashed line. This represents photodesorption at the initial substrate temperature, $T_0 = 50K$, with resonant heating effects ignored. In actuality, the adsorbate population (solid line) decays more rapidly, leading to a 30% smaller desorption time, $t_d = 1.5 \cdot 10^{-5}$ s, as given by (3.12). The temperature at the surface throughout this process is graphed versus time in Fig.3.4. The surface temperature increases from 50K to over 60K, within the desorption time t_d, and then decays as the adsorbate leaves the surface and the resonant heating flux $\dot{E}(t)$ drops to zero.

The effect of this temperature increase on the desorption rate, $r_d = t_d^{-1}$, is understood by referring back to Fig.2.8 in which we plotted r_d vs T^{-1}. At saturation intensity, increasing the temperature from 50 to 60K gives an increase in the photodesorption rate of about 1/3, in agreement with the result of Fig.3.3. This moderate increase in the desorption rate is a result of the relatively weak dependence of r_d on T in this region, as shown in Fig.2.8. Photodesorption at

---

*The factor $C_v\sqrt{\chi}$ in (3.9) is estimated, for the temperature range of interest from data given in reference 80.

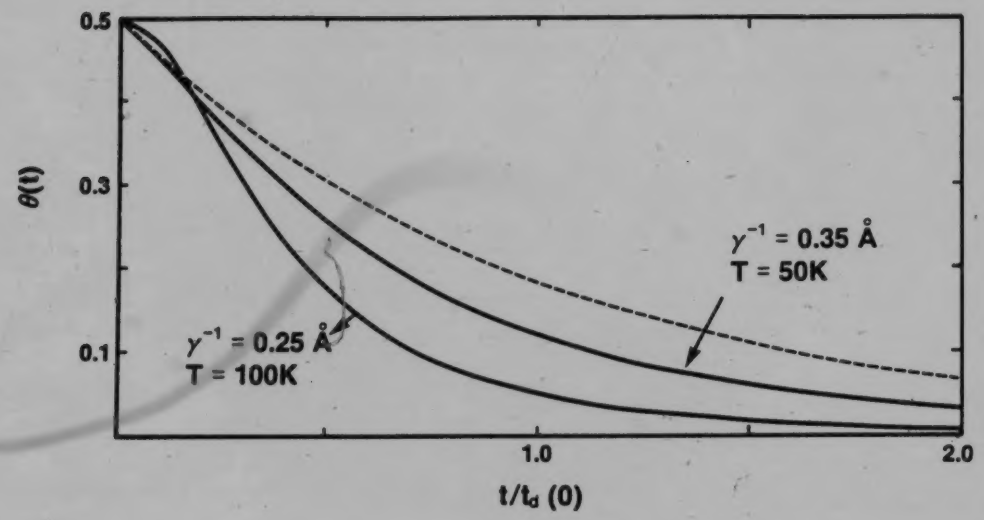

Fig.3.3. Time dependence of the coverage, $\theta(t) = N(t)/N(0)$ for the $CH_3F/NaCl$ system at saturation intensity with surface potential range $\gamma^{-1} = 0.35$Å. Dashed line is pure exponential decay ignoring heating effects.

this temperature and laser intensity is stimulated mainly by photoexcitation processes ($L^{v'v}$) rather than thermal excitation.

On the other hand, at higher temperatures, thermal excitation processes become more efficient and contribute more significantly to photodesorption (see Fig.2.8). As a result of this stronger temperature dependence, at $T_o = 100$ K, a smaller temperature rise of $\Delta T = 6$K is still sufficient to reduce the desorption time by 40%. Resonant heating also depends on the adsorbate system parameters. At moderate intensities, below saturation, the resonant heating cycle shown in Fig.3.2 is limited by the laser-vibrational excitation rate $L^{v+1,v}$. A high effective charge (Q) and small vibrational linewidth (Γ_v) lead to more efficient heating in this case. At higher intensities, the vibra-

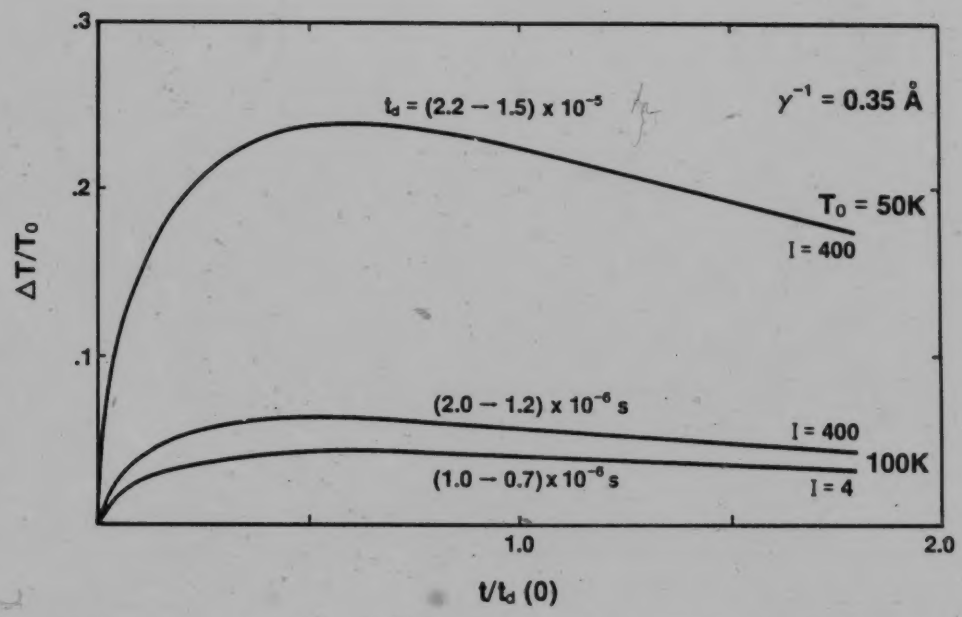

Fig.3.4. Relative change in surface temperature, $\Delta T/T_0 = (T(0,t)-T_0)/T_0$, as a function of time. The change in t_d is also noted. (These graphs are only relevant to the experimental situation for times $t < t_L$ = laser pulse duration.) Laser intensity is measured in MW/cm²; initial coverage is half a monolayer.

tional-to-translational transfer rate, e.g., P_{60}^{01}, may limit the heating process. Stronger coupling of the adsorbate to the solid, achieved by increasing the depth (V_0) or decreasing the range (γ^{-1}) of the surface potential, enhances this rate, leading to greater surface heating at high intensities. This effect has been verified numerically.

Also of theoretical interest is the temperature profile in the solid, as graphed for different times through the desorption process in Fig.3.5. At a high intensity and for a narrower surface potential range, a surface temperature rise of over 30% is predicted. Even in these conditions, the temperature rise extends 500 to 1000Å into the solid. These distances are longer than the typical length scale of

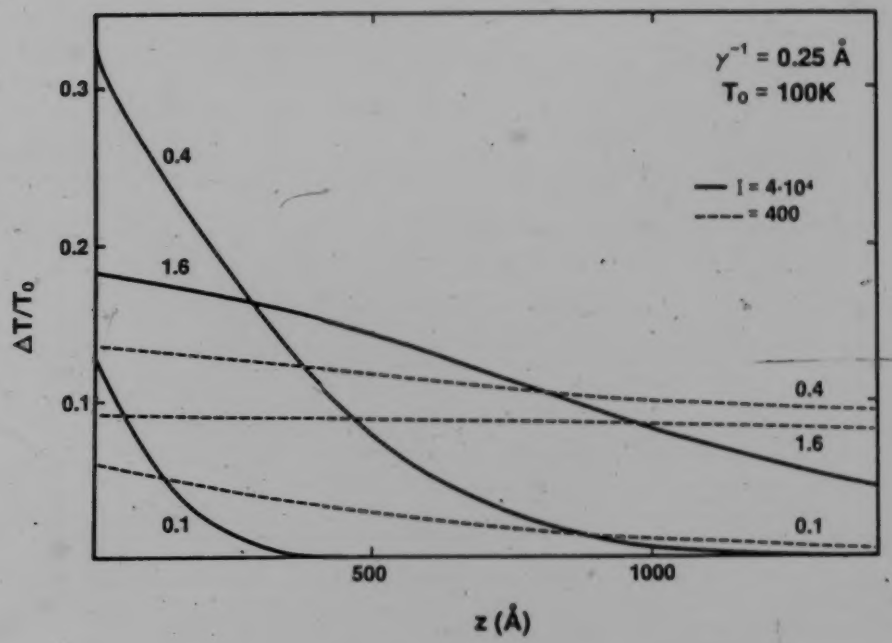

Fig.3.5 Temperature profile into the solid at high intensity for $CH_3F/NaCl$ system with γ^{-1} = 0.25Å, at various times $t/t_d(0)$=0.1, 0.4, and 1.6. Intensity I is given in units of MW/cm².

the phonon mean free path, i.e., ≈ 100Å. Furthermore, $\Delta T/T_0$ changes on a microsecond time scale in Fig.3.4, which is much longer than the phonon lifetimes. These observations show that local equilibrium conditions exist, justifying the use of a (macroscopic) thermodynamic description - i.e., T(z,t) - for the energy distribution in the solid.

3.2.2 Approximate solution[73]

The analysis presented above shows that resonant heating is most efficient in enhancing desorption under conditions in which the photodesorption rate is strongly temperature dependent. However, the large theoretical photoenhancement of desorption yields found in Section

2.6 depends rather weakly on temperature. Rather, heating effects are most important in situations for which purely thermal desorption from the elevated surface temperature is efficient. We now present a simplified theoretical description of this latter situation, which is then compared with experimental work on both single and multicomponent absorbates. In addition, we include phenomenologically other vibrational decay mechanisms, such as electronically mediated processes, that are not treated in the microscopic theory of Section 3.2.1 above.

The procedure for simplifying the full master equation (3.8) and including electronic vibrational damping is now described. In cases for which the photo-enhancement of desorption in Section 2 is not too efficient, rapid phonon-assisted transitions thermalize the molecular occupation of the surface bond states, i. This allows us to use the ansatz

$$n_i^v(t) = a_v(t)\, e^{-\beta E_i} \Big/ \sum_j e^{\beta E_j} \quad . \tag{3.13}$$

Note that the vibrational state occupations, given by $a_v(t)$ are not necessarily thermalized. They obey a reduced master equation, obtained by substituting (3.13) into (3.8) which yields

$$\frac{d}{dt}\, a_v(t) = \sum_{v'} (L^{vv'} + R^{vv'})a_{v'} - \sum_{v'} (L^{v'v} + R^{v'v})a_v - R_d a_v \quad , \tag{3.14}$$

where

$$R^{vv'} = \sum_{i,i'} e^{-\beta E_{i'}} \left(P_{ii'}^{vv'} + R_{ii'}^{vv'}\right) \Big/ \sum_{j} e^{-\beta E_j} \tag{3.15}$$

and

$$R_d^{v} = \sum_{v'i} e^{-\beta E_i} \left(P_{ci}^{v'v} + Q_{ci}^{v'v}\right) \Big/ \sum_{j} e^{-\beta E_j} . \tag{3.16}$$

In (3.14) to (3.16), the sums over v', i, and i' exclude the terms (i'v') = (i,v). The diagonal rate matrix elements in the master equation (see (3.8)) are included explicitly as the last two terms in (3.14). The transition rate term $L^{v'v}$ describes stepwise vibrational (de)excitation by the laser, $P_{i'i}^{v'v}$ represents phonon-assisted transitions between bound states, while $P_{ci}^{v'v}$ and $Q_{ci}^{v'v}$ are, respectively, phonon-assisted and direct tunneling rates to the gas phase. (These rates were described in Section 2.4.) The additonal transition rate term in (3.15), $R_{i'i}^{v'v}$, is included to describe vibrational damping arising from molecular coupling to the conduction electrons of the metal. Since we do not calculate $R_{i'i}^{v'v}$ explicitly, the entire vibrational transition rate, $R^{v'v}$, is treated as a phenomenological parameter. Note also that we assume that the desorption term in (3.14) is independent of v; that is,

$$R_d^{v} = R_d . \tag{3.17}$$

This approximation is valid provided diagonal vibrational terms, v' =

v, dominate in the sum in (3.16), as is the case when the photo-enhancement of desorption in Section 2 is small. In this way, we assume that the thermal desorption mechanism dominates in (3.16), and therefore write R_d in its customary parametrization

$$R_d = \nu\, e^{-\beta E_d} \; ; \; \beta = 1/k_B T \tag{3.18}$$

as given previously in (2.93). It is through this term that the substrate temperature (T) enters the master equation (3.14).

The heat flux into the solid, previously given by (3.5), now receives contributions from both phonon and electronic processes, $P_{i'i}^{v'v}$ and $R_{i'i}^{v'v}$, respectively. This yields

$$\dot{E}(t) = N_a \sum_{iv} \sum_{i'v'} (E_i^v - E_{i'}^{v'})(P_{i'i}^{v'v} + R_{i'i}^{v'v})\, n_i^v(t) \; . \tag{3.19}$$

(The last term in (3.5) due to transitions to continuum states has negligible contribution to $\dot{E}$ and is thus dropped here.) A simpler form for $\dot{E}(t)$ is deduced by examining the features of the resonant heating cycle shown in Fig.3.2. At low temperature, the dominant phonon tunneling transition, $P_{i'o}^{01}$ (horizontal line in Fig.3.2), is immediately followed by a rapid cascade of downward transitions, $P_{i''<i'}^{00}$, that take the molecule back to the ground state (i,v) = (0,0). The net amount of energy given up to the solid in this phonon emission sequence is $\hbar\Omega$. To describe this process we may approximate E(t) by letting $E_i^v - E_{i'}^{v'} = E_o^v - E_o^{v'} = \hbar\Omega(v-v')$ in (3.19) and using the

ansatz (3.13) for $n_i^v(t)$ to get

$$\dot{E}(t) = N_a \hbar\Omega \sum_{v,v'} (v-v') R^{v'v} a_v(t) . \qquad (3.20)$$

(The summation over v,v' omits v = v' terms.)

The heat flux given above results from laser-assisted vibrational excitation, immediately followed by vibrational damping into the phonon bath of the solid. The damping may occur via either (i) excitation of translational motion ($P_{i'>i}^{v'<v}$), or (ii) electronic excitation in the substrate ($R_{ii}^{v'v}$). Provided the electrons and phonons in the substrate thermalize rapidly, the rate $R^{v'v}$ in (3.20) satisfies detailed balance. That is,

$$R^{v'v} e^{-\beta\hbar v\Omega} = R^{vv'} e^{-\beta\hbar v'\Omega} . \qquad (3.21)$$

The resonant heating process deposits the energy flux, $\dot{E}(t)$ in (3.20), into the substrate, which then experiences a temperature rise given by (3.9). Starting from an initially uniform temperature field in the solid, $T(z',t_o) = T_o$, and assuming $\dot{E}(t')$ is constant over the duration of the laser pulse time t_L (this will be justified below), allows for simplification of (3.9) to

$$T(z,t) = T_o + \frac{V_m}{C_v} \frac{\dot{E}}{\sqrt{\pi\chi}} \int_{t_o}^{t} dt' \frac{e^{-z^2/4\chi(t-t')}}{(t-t')^{1/2}} \qquad (3.22)$$

The surface temperature rise is thus given by

$$\Delta T(t) = T(0,t) - T_o$$

$$= \frac{2}{\sqrt{\pi}} \frac{V_m}{C_v\sqrt{\chi}} \dot{E} \left[\sqrt{t}\ \theta(t_L-t) + (\sqrt{t} - \sqrt{t-t_L}\ )\ \theta(t-t_L) \right] \qquad (3.23)$$

To understand this temperature rise, we rewrite (3.23) for $t<t_L$ as

$$\Delta T(t) = \frac{2}{\sqrt{\pi}} \frac{\dot{E}t}{C_v V_m^{-1}\sqrt{\chi t}}$$

$$= \frac{2}{\sqrt{\pi}} \frac{\text{energy absorbed per unit surface area}}{C_v V_m^{-1} \times \text{depth heated}} . \qquad (3.24)$$

This shows simply that the resonant heat flux penetrates the solid to a depth of $\sqrt{\chi t}$, as expected from the diffusion equation (3.6). The resultant temperature rise at the surface in (3.24) is proportional to

$$\frac{V_m}{C_v\sqrt{\chi}} = \frac{\sqrt{\chi}}{\lambda} = \sqrt{\frac{V_m}{C_v\lambda}} \qquad (3.25)$$

since the diffusivity is given by $\chi = \lambda\ V_m/C_v$. Increasing either the heat capacity per unit volume (C_v/V_m), or the thermal conductivity (λ), decreases the rise in temperature at the surface. For example, at 100K, the thermal conductivity of Cu is an order of magnitude

larger than that of NaCℓ, while the heat capacity of Cu is smaller by about the same amount. The result is that the ratio in (3.25) differs by only 25% between Cu and NaCℓ. Furthermore, increasing temperature causes an increase in C_v, but a decrease in λ. The substrate parameters (3.25) in the temperature rise formula are therefore quite similar for the experimental photodesorption systems considered to date.

We now return to consider the reduced master equation, (3.14). At moderate laser intensities, higher vibrational states are considerably less occupied than the lowest levels. It is then sufficient to include only the $v = 0$ and $v = 1$ levels in (3.14). Furthermore, the detailed balance condition (3.21) states that $R^{10} \ll R^{01}$ at the low temperatures considered here. That is, vibrational damping (R^{01}) by the substrate is much more efficient than thermal excitation (R^{10}). The laser provides the only significant vibrational excitation process. In these approximations, the rate equations (3.14) reduce to

$$\frac{d}{dt} a_0 = -(L+R_d)a_0 + (L+R)a_1$$

$$\frac{d}{dt} a_1 = La_0 - (L+R+R_d)a_1 \qquad (3.26)$$

where we let $L = L^{10}$ and $R = R^{01}$. Solving (3.26) leads to

$$\frac{N(t)}{N(0)} = a_0 + a_1 = e^{-R_d t} \qquad (3.27)$$

and

$$a_1(t) = \frac{L}{R+2L}\, e^{-R_d t} - \frac{L}{R+2L}\, e^{-(2L+R+R_d)t} \tag{3.28}$$

Equation (3.27) shows that desorption occurs with a temperature dependent rate, R_d. Note that the second, transient term in $a_1(t)$ is of negligible amplitude for times $tR \gg 1$ and may therefore be ignored. Substituting (3.28) into (3.20) and using the same approximations as those contained in (3.26) leads to

$$\dot{E}(t) = N_a \hbar\Omega R a_1(t) = N_a \hbar\Omega \frac{RL}{R+2L}\, e^{-R_d t} . \tag{3.29}$$

Since R_d depends on temperature, one gets, in principle, a nonlinear equation for ΔT by substituting (3.29) into (3.23). However, experimentally measured photodesorption yields are typically very small, implying that $R_d t_L \ll 1$ (see (2.75)). This shows that the energy flux, $\dot{E}(t)$ in (3.29), is practically constant over the duration of a laser pulse, with its exponential factor equal to one. This justifies taking $\dot{E}$ out of the integral in reducing (3.9) to (3.24).

In summary, equations (3.18), (3.23), and (3.29) predict thermal desorption at an enhanced surface temperature due to resonant heating, with rate constant

$$R_d(T_o+\Delta T(t)) = \nu \exp[-E_d/k_B(T_o+\Delta T(t))] \tag{3.30}$$

where

$$\Delta T(t) = \frac{2}{\sqrt{\pi}} \frac{\hbar\Omega\sqrt{\chi}\, N_a}{\lambda} \frac{RL}{R+2L}$$

$$*[\sqrt{t}\ \theta(t_L-t) + (\sqrt{t} - \sqrt{t-t_L}\ \theta(t-t_L)] \ . \qquad (3.31)$$

Since R_d depends exponentially on ΔT, experimental desorption yields receive their main contribution from $R_d(T_s)$ where $T_s = T_o + \Delta T(t_L)$ is the maximum surface temperature. We therefore discuss the behaviour of $R_d(T_s)$ in the next section when comparing with experimental work.

3.3 Comparison with Experiments; Discussion

Recent experiments on the photodesorption of NH_3 and ND_3 from Cu(001) provide support for the resonant heating mechanism discussed above. By resonantly exciting an internal vibrational mode of adsorbed NH_3, Hussla et al.[74] observe desorption yields that depend on laser frequency and intensity, and on absorbate coverage. They also co-adsorb ND_3 and observe laser-stimulated desorption of both NH_3 and ND_3. These experimental phenomena are analyzed in terms of the theory of photodesorption, including resonant heating effects.

First, we consider the NH_3/Cu(001) adsorption system. Using temperature-programmed thermal desorption measurements, the heat of adsorption (E_d in (3.18)) is estimated for the different adsorption phases present. Using a kinetic prefactor $\nu = 5\cdot10^{14}\ s^{-1}$ in (3.18) gives adsorption energies of $E_\alpha = 70 \pm 7$ kJ/mole and $E_\beta = 52 \pm 5$ kJ/mole, identifying two distinct adsorption sites at mono-

layer coverage. At multilayer coverage, physisorption is characterized by $E_\gamma = 35 \pm 4$ kJ/mole, and a "solid" NH_3 phase with $E_\delta = 29$ kJ/mole is seen at still higher gas dosage. The prefactor, ν, was chosen to fit E_δ to the heat of sublimation of solid NH_3. However, changing ν by an order of magnitude causes only 10% variations in the energy estimates, which is within the experimental error. Photodesorption at monolayer coverage is expected to deplete the β-phase, while the γ-phase is removed in multilayer conditions.

Using a pulsed laser tuned in the infrared frequency region 3320 to 3370 cm^{-1}, experimental photodesorption yields are found to depend

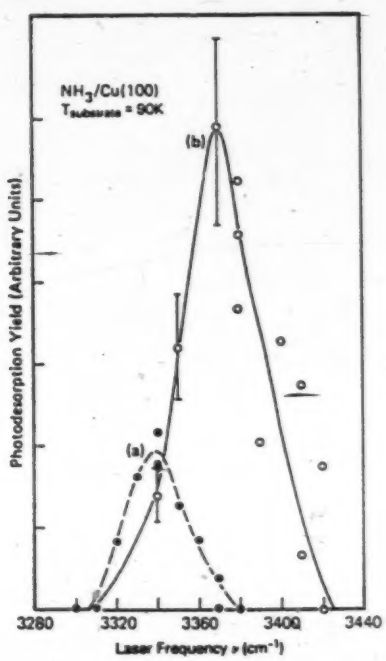

Fig.3.6. Photodesorption yields of NH_3 on Cu(100) as a function of laser frequency at a fluence of 1.0mJ/cm^2 and coverages (a) $\theta = 1$, and (b) $\theta = 3.4$.[73]

resonantly on the laser frequency, as shown in Fig.3.6. Superimposed

are results for (a) monolayer coverage, and (b) for about 3 monolayers. The peak positions at 3340 and 3360 cm^{-1} are close to the symmetric and asymmetric stretching modes of gaseous NH_3, which have frequencies $\nu_{s,gas}$ = 3377 cm^{-1} and $\nu_{a,gas}$ = 3414 cm^{-1}, respectively. The laser fluence dependence of the desorption yield is given in

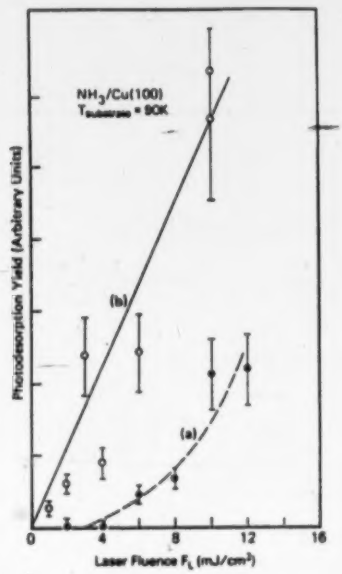

Fig.3.7. Photodesorption yields of NH_3/Cu(100) as a function of laser fluence. (a) θ = 1, Ω_ℓ = 3340cm^{-1}; (b) θ = 3.4, Ω_ℓ = 3370cm^{-1}.[73]

Fig.3.7 (laser fluence = intensity x pulse duration.) At monolayer coverage, desorption of the β-phase shows a smaller magnitude, but more strongly nonlinear intensity dependence, than that of the γ-phase in the multilayer situation. These effects can be understood theoretically, as outlined below.

We first attempt to predict the yield versus intensity dependence of Fig.3.7 using the photodesorption theory of Section 2, ignoring

resonant heating. A phenomenological, vibrational damping constant of $10^{11}s^{-1}$ has been included to account for electronically assisted relaxation.[74-76] The results shown in Fig.3.8 for desorption from both β and γ phases, give a rate constant, $r_d \approx 10s^{-1}$ at $I = 1MW/cm^2$ and $T = 90K$. However, the theory of Section 2 predicts selective desorption, while nonselective desorption of coadsorbed isotopes is observed

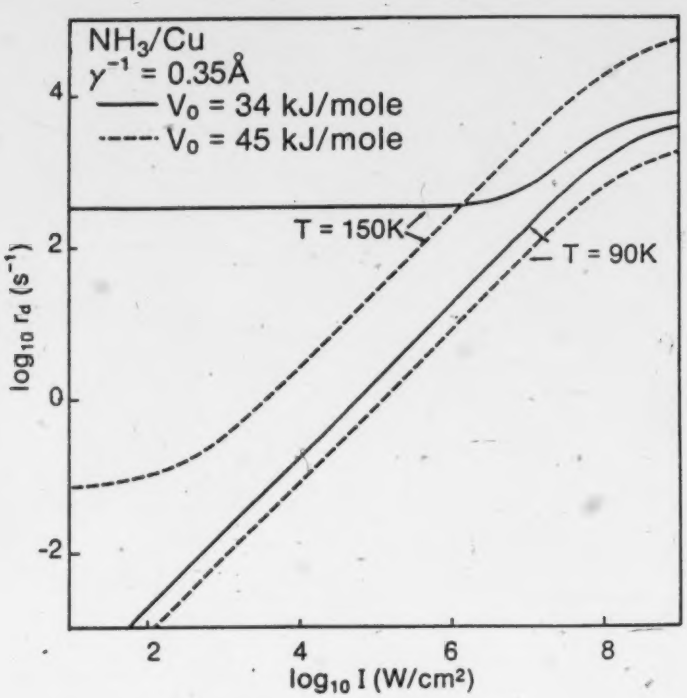

Fig.3.8. Selective photodesorption rates for NH_3/Cu(100) as a function of laser intensity for T = 90 and 150K. Surface potential depths V_o = 34 and 45kJ/mole represent coverages of 3.4 and 1 monolayers, respectively. $\Gamma = 40cm^{-1}$.

experimentally. Furthermore, the moderate intensity dependence for both phases is predicted to be linear, leading to poor agreement with the experimental results in Fig.3.7. For these reasons, we now apply the resonant heating theory of Section 3.2.2 – namely, enhanced ther-

mal desorption from an elevated surface temperature - to explain the observed photodesorption yields.

The resonant heating theory requires as inputs, in addition to the Arrhenius parametrization of thermal desorption kinetics ($R_d(\nu,E_d)$), values for the vibrational damping rate (R) and laser-excitation rate (L) given by (2.49). We treat R and Q, the effective charge entering L, as phenomenological parameters to be fitted to the experimental results. Note that at multi-layer coverage, direct electronic damping is expected to be inefficient. However, rapid vibrational energy transfer between adsorbate layers is anticipated, even in the eventuality of some vibrational energy mismatch. (See Section 4, and references 81-86.) This allows for efficient vibrational damping of physisorbed overlayer molecules by a multistep process involving transfer of vibrational quanta to molecules in the first layer which are subsequently damped by electronic coupling. In this way, infrared absorption by all molecules in the adsorbate contributes to surface heating. This feature contributes to the coverage dependence of the desorption yields.

In attempting a comparison between theory and experiment, we first note that the desorption yield axis of the experimental graphs in Fig.3.7 is uncalibrated. Only an upper limit on the absolute magnitude of the desorption yields is known; this translates, via (2.74), into a condition on the rate constant,

$$r_d < 3 \cdot 10^4 \ s^{-1} \ , \qquad (3.32)$$

at a laser fluence of 10 mJ/cm^2. We therefore have to choose, some-

what arbitrarily, an absolute desorption rate scale in Fig.3.7. (Recall that yield = rate x pulse duration here.) Once this is done, the coupling parameters, R and Q, may be chosen to predict the correct intensity dependence of r_d for the mono- and multi-layer coverage sit-

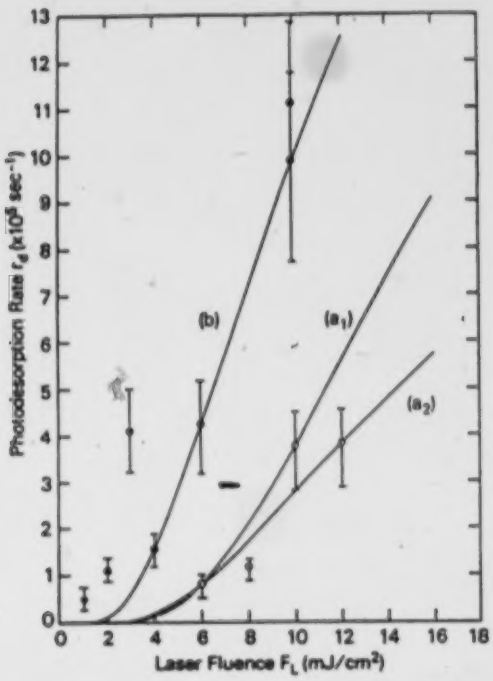

Fig.3.9. Desorption rate versus laser fluence for NH_3/Cu(100). The angle of incidence is 75° and the effective charge Q given below corresponds to laser linewidths Γ = 1.0~3.0cm^{-1}. Curve b: E_d = 35kJ/mole, R = $4.6 \cdot 10^{10} s^{-1}$, Q = (4.2-7.8)e. Curve a: E_d = 51kJ/mole, R = $2.6 \cdot 10^{11} s^{-1}$, Q = (5-9)e. Here E_d and $\nu = 5 \cdot 10^{14} s^{-1}$ are the thermal desorption parameters in (3.30).

uations. In Fig.3.9, the fitted theoretical rate constant r_d is shown, superimposed on the experimental results of Fig.3.7.* The increase in

surface temperature needed to induce these desorption rates is shown

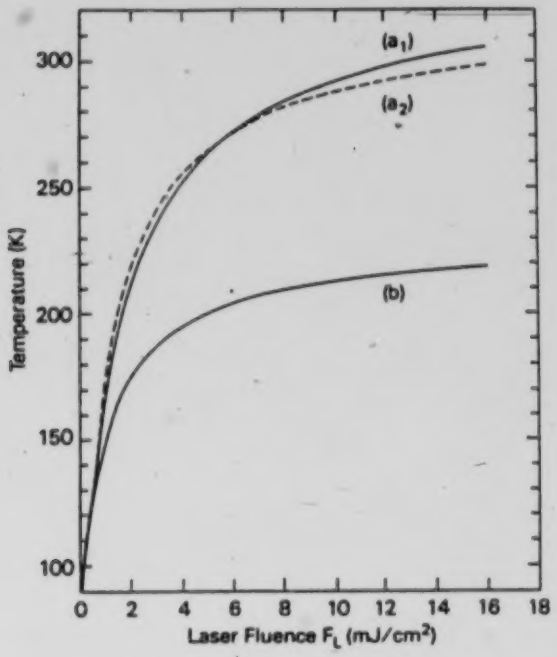

Fig.3.10. Maximum surface temperature rise used in Fig.3.9, calculated from (3.31) at $t=t_L=6$nsec, and using the parameters given under Fig.3.9.

in Fig.3.10 as a function of laser fluence. A higher temperature is needed to desorb the more strongly bound, monolayer adsorbate in (a) than the physisorbed overlayer molecules in case (b). Theoretically, to obtain comparable yields for the two cases requires that $T_\beta/T_\gamma \approx E_\beta/E_\gamma$. This very approximate relation is obtained by using

*In obtaining the theoretical results shown in Fig.3.9, we assumed originally that the homogeneous vibrational width was only 1-3cm^{-1}, while the spectrum in Fig.3.6 is considerably broader. If the additional broadening is caused by inhomogeneous effects, it may be taken into account in our theory by simply rescaling the (already arbitrary) desorption rate axis in Fig.3.9. On the other hand, an increased homogeneous linewidth may be included by rescaling the fluence axis instead. This would necessitate redetermining the fit between theory and experiment, although qualitatively similar results at slower desorption rates would be expected.

the form (3.30) for r_d and assuming that $\nu_\beta = \nu_\gamma$, and is roughly obeyed in Fig.3.10. We find, in Fig.3.10, that desorption from the multilayer, γ-phase occurs more readily than from the monolayer, β^4-phase. This is due to the smaller heat of adsorption for the γ-phase, that is, $E_\gamma/E_\beta < 1$. The nonlinear dependence of r_d on laser fluence (or equivalently, intensity) arises from the exponential dependence of R_d on temperature in (3.30). Thus, while the temperature rise, $\Delta T(t_L)$ in (3.31), is proportional to the fluence, r_d is not.

The significance of the parameter choice used in obtaining the data fit in Fig.3.9 must be considered. First, we note that the vibrational damping rate is diminished by a factor of 5-6 in going from the monolayer ($R = 2.7 \cdot 10^{11}$ s^{-1}) to the multilayer ($R = 4.6 \cdot 10^{10}$ s^{-1}) case. This is reasonable because (i) in the multilayer case, only the fraction of the adsorbate that is in the first monolayer is damped directly by the substrate, and (ii) vibrational transfer rates between adsorbate layers may partially limit the damping of vibrations in the overlayers. The rather large values of the effective dipolar charge per adsorbed molecule, $Q = 2$-4 el. ch. in going from γ to β^4 phases, may be reconciled by postulating a moderate field enhancement at the surface,[48] rather than by invoking an unusually large molecular polarizability. The smaller value of Q assigned to the overlayer molecules may be interpreted in terms of an orientational effect. One may speculate that in the submonolayer case, NH_3 adsorbs with the nitrogen atom closes to the surface, and that the symmetric stretch mode with dipole moment normal to the surface is excited by the laser. (The electric field has negligible amplitude in the direction parallel to the metal surface.) Overlayer molecules, with less propensity for

this perpendicular orientation, would be expected to couple less strongly with the radiation, leading to a smaller effective charge, Q. (This orientational disorder would also permit the asymmetric stretch mode, previously fixed nearly parallel to the surface, to adsorb radiation too. Infrared adsorption in the overlayer could receive contributions from both vibrational modes.) The fact that the multilayer desorption peak in Fig.3.6. is higher than in the monolayer case is due primarily to the smaller binding energy for the overlayer (γ-phase) molecule.

Hussla et al have also measured photodesorption of NH_3 and ND_3 from Cu(001).[73] Initially, NH_3 and ND_3 are coadsorbed in equal amounts to a total coverage of 2-3 monolayers. The NH_3 molecules are then excited vibrationally by the laser tuned to Ω_ℓ = 3370 cm^{-1}. However, both NH_3 and ND_3 are detected as desorption products in the mass spectrometer, with roughly equal yields. Thus, to within an error of 25%, there is no isotope selectivity in the photodesorption of these isotopic coadsorbates. Although only NH_3 molecules are initially excited by the laser, either the resonant heating mechanism described above, or direct non-resonant vibrational transfer processes cause ND_3 to desorb as readily as NH_3. This is in contrast to the predictions of the selective photodesorption mechanism described previously in Section 2 where heating effects were ignored.

We conclude this section by comparing the photodesorption processes discussed so far and considering their relative importance. First, it was shown in Section 3.2.1 that resonant heating does not enhance the already efficient photodesorption process for CH_3F on NaCl at submonolayer coverage. In this case, selective photodesorption may be possi-

ble. On the other hand, in Section 3.3 above, we found that the resonant heating process best predicts the desorption of NH_3 from Cu at monolayer to multilayer coverage. In fact, photodesorption is found to be non-selective isotopically in experiments on this adsorption system. This may be attributed to the inefficiency of the selective photodesorption process as shown in Fig.3.8, and to an efficient resonant heating mechanism. While the theoretical results in Fig.3.9 involve phenomenological fitted parameters, it is suggested that resonant heating can induce a significant amount of thermal desorption in the NH_3/Cu case. To better pin down the theoretical parameters and check the accuracy of this theory, additional experimental work is needed. An adsolute determination of the desorption yields is desirable. Infrared adsorption data would fix the effective charge (Q) and set an upper limit on the damping rate (R). Additional thermal desorption spectra at a second temperature ramp rate would pin down the parameterization of $R_d(\nu,E_d)$ better. Theoretically, explicit determination of lateral energy transfer rates in the adsorbate, especially between different isotopes and adsorption sites, would be useful, as would be a full three dimensional calculation taking into account energy exchange with rotational/librational degrees of freedom.

In spite of this, some important qualitative conclusions are in order. Resonant heating is clearly reduced at low coverage and at low initial substrate temperature. A high specific heat per unit volume and a high thermal conductivity both diminish the surface heating effect. Reducing vibrational damping by electronic processes, achieved by using a dielectric substrate instead of a metal, leads to

both reduced heating and more efficient selective photodesorption. All these conditions clearly enhance the possibility of selectively desorbing isotopes, initiated by resonant absorption of infrared radiation.

4. Lateral Vibrational Energy Transfer

4.1 Introduction

Molecules in the solid state and at surfaces may undergo efficient vibrational energy transfer if the energies of their respective vibrational modes are in near coincidence. The effect of such a transfer process between adsorbed molecules on the kinetics of photodesorption is considered in this chapter. Impetus for studying this phenomena comes largely from experience with matrix-isolated molecules.[81]

Infrared laser-induced vibrational excitation to high quantum numbers has been observed in molecules trapped in rare-gas matrices in the past.[82,83] However, anharmonicity of the internal vibrational mode of such molecules makes the single photon absorption process, $v \rightarrow v+1$, nonresonant for such high quantum levels. Vibrational energy transfer, due to the dipole-dipole interaction between molecules, has been proposed to assist in the excitation process. For example, a molecule that is excited to its first vibrational level ($v_1 = 1$) may interact with another, leading to the transfer process - $v_1 = 1 \rightarrow 0$, $v_2 \rightarrow v_2+1$ - as shown in Fig.4.1. The transition can be resonant, as shown in (a), or non-resonant, as in transition (b). In the latter case, vibrational anharmonicity (exaggerated in Fig.4.1) can cause a significant energy mismatch between the two vibrational transitions involved. This is so because the vibrational energy level spacings of the adsorbed molecule are not equal, but rather given roughly by

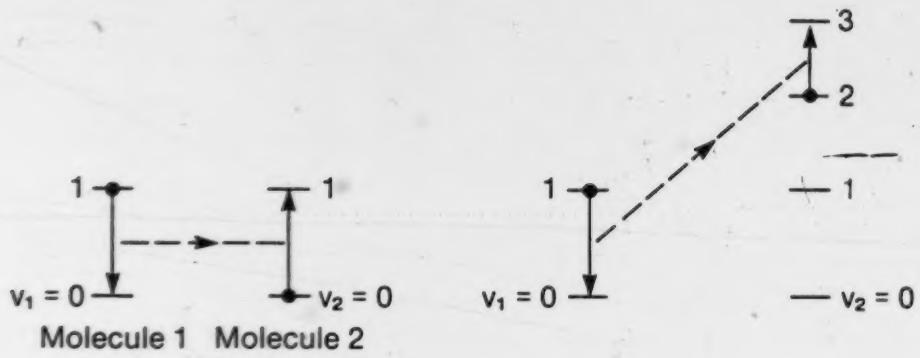

(a) A resonant transition (b) A non-resonant transition

Fig.4.1 Possible vibrational transfer processes between molecules.

$$E_{v+1} - E_v = \hbar(\Omega - v\Delta) \tag{4.1}$$

for small v, in terms of the anharmonic defect Δ, with $\Omega = E_1 - E_0$. The anharmonic energy mismatch in a V-V transfer process where $v_1 \rightarrow v_1 - 1$, $v_2 \rightarrow v_2 + 1$ is then defined by

$$E_{v_1 v_2} = \left|(E_{v_1} - E_{v_1 - 1}) - (E_{v_2 + 1} - E_{v_2})\right| = \hbar\left|v_2 - v_1 + 1\right|\Delta . \tag{4.2}$$

For example, the energy mismatch is $E_{12} = 2\hbar\Delta$ for the transition shown in Fig.4.1(b). The excess energy must be taken up by the other molecules in the solid matrix, and can occur by excitation of acoustic phonon modes. This type of process has been used, in a master equation approach, to successfully explain the observed vibrational level populations.[84] Phonon-assisted vibrational transfer has been shown to

be an efficient process, which, even for resonant transitions, is only an order of magnitude slower than direct, dipole-dipole mediated transfer.[85]

Furthermore, detailed balance requires that the phonon-emission process shown in Fig.4.1b be faster than the reverse transition involving phonon absorption by a factor of $e^{E_{v_1 v_2}/k_B T}$. For low enough substrate temperatures T, i.e., $k_B T < \hbar\Delta$, nonresonant vibrational transfer favours excitation of high levels, $v \rightarrow v+1$, over de-excitation, $v \rightarrow v-1$! This fact has been used to explain observed population inversion of the vibrational levels.[84,86] Note that this effect is only possible if vibrational damping by the substrate is less efficient than the transfer processes discussed above. In matrix isolation, vibrational lifetimes are exceedingly long, typically 10–100 msec, and in fact dominated by radiative decay.[82] This, combined with narrow spectral lineshapes, facilitates effective vibrational transfer in a solid matrix.

At a surface, however, the broken translational symmetry of the substrate leads to enormously shortened vibrational lifetimes and broader lineshapes for adsorbed molecules.[61] To understand this, we intuitively picture the matrix and surface cases in Fig.4.2 below, and study translational and vibrational motion of the molecule in the horizontal direction. To the extent that the (van der Waals) bonding (dashed lines) is the same to both ends of the diatomic molecule in the matrix, then at low temperatures, long wavelength phonons will affect only the translational motion of the molecule. Its vibrational motion is uncoupled from its translational coordinate, except in the presence of short wavelength phonons, present at high temperatures

Fig.4.2 Comparison of molecule in matrix and at surface.

($T \approx T_{Debye}$). On the other hand, an adsorbed molecule, bonded as shown in Fig. 4.2, has vibrational and translational coordinates coupled by the "residual interaction" term given by (2.6). This coupling is due to the much stronger interaction of the solid to one end of the molecule than to the other. As a consequence, vibrational damping by transition to an excited state of frustrated translation ($P_{1,0}{}^{v-1,v}$ in Section 2.4.2.) is an efficient process, assisted by a (long wavelength) phonon. Furthermore, the low temperature limit ($k_BT < E_{vv'}$) of the matrix case is not realized in most photodesorption experiments, in which k_BT is typically several times larger than $E_{vv'}$. (This is partly because of using higher temperatures, but also due to the fact that vibrational damping at the surface restricts one to low

vibrational levels where the anharmonic mismatch, $E_{vv'}$, is less.) We should thus not base our intuition too strongly on matrix-state results when considering vibrational transfer between molecules adsorbed at surfaces.

Vibrational interaction between molecules adsorbed on a solid has been studied by means of infrared absorption spectrosocopy. Dipole-dipole coupling in the adsorbate leads to collective normal vibrational modes (optical phonons) with frequency shifted from the single-molecule case.[87] The effects of partial coverage and of the substrate on this interaction have also been addressed.[88] However, in a theory of desorption phenomena, the dynamics of individual molecules must be considered. Note that absorption of infrared radiation excites only long wavelength optical phonons, in which neighbouring adsorbate molecules vibrate in unison in response to the same incident electromagnetic field. We may then describe this energy transfer process in terms of phonon absorption per individual adsorbate molecule. The coverage induced frequency shift is contained in the vibrational normal mode frequency, Ω, determined experimentally.

Heidberg et al have suggested the possibility of accessing higher vibrational levels in adsorbed molecules by vibrational coupling.[89] Recently, Fain and Lin[36] showed that V-V coupling can enhance photodesorption when photon-assisted vibrational pumping is cut off above the first excited level. They assume that a laser, tuned to resonantly excite the lowest vibrational level ($v = 0 \rightarrow 1$), cannot efficiently excite higher levels due to the energy mismatch arising from large vibrational anharmonicity, $\Delta >> \Gamma$ (Γ is the vibrational linewidth). Vibrational energy transfer, if rapid enough, then excites higher

vibrational levels by transitions such as $v_1 = 1 \to 0$, $v_2 = 1 \to 2$ as a necessary precursor to desorption. For example, they consider the model shown in Fig.4.3 where the adsorbed molecule must be excited to its

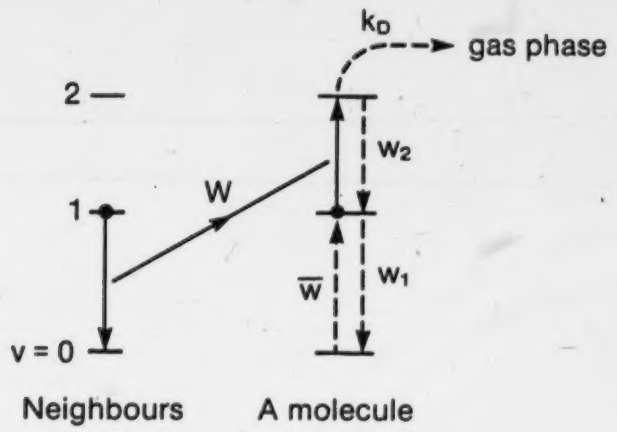

Fig.4.3 The photodesorption mechanism of Fain and Lin[38]. Solid lines indicate vibrational transfer; dashed lines represent single-molecule transitions.

second vibrational state before desorption is possible. Then, from this excited state, $v = 2$, desorption is allowed to proceed with rate constant k_D. The laser excites the $v = 1$ level with rate $\bar{w}$, but vibrational damping is assumed to occur at a much faster rate, w_1. The V-V transfer rate W is assumed to be faster than all other processes, leading to a homogeneous distribution of vibrational excitation throughout the adsorbate.

In these approximations, Fain and Lin[38] arrive at a simple formula for the photodesorption rate, due to the pathway shown in Fig.4.3 for monolayer coverage,

$$r_d = P_2 k_D = \left(\frac{\bar{W}}{w_1} \right)^2 \frac{W}{w_2 + k_D} k_D \ ,$$

$$\text{for times } t > (w_2 + k_D)^{-1},\ w_1^{-1} \qquad (4.3)$$

This formula may be interpreted as follows. Since $\bar{W} << w_1$, the probability of a molecule occupying its v = 1 state is $\bar{W}/w_1$, and the probability for a pair of molecules to do so simultaneously is $(\bar{W}/w_1)^2$. The molecule then absorbs a vibrational quanta from one of its neighbours with probability per unit time W, to end up in the v = 2 level. This process competes with decay from the v = 2 state at the rate $k_D + w_2$. This gives the second term in (4.3) and the occupation probability (P_2) of the v = 2 level, from which desorption proceeds with rate k_D. Note that, since $\bar{W}$ is proportional to laser intensity, desorption depends on intensity squared. This formula is obtained by using a reduced master equation in which only the vibrational coordinate is considered explicitly, thus averaging implicitly over the frustrated translational and rotational motion.[38] We will see shortly that the "large anharmonicity" and "fast V-V transfer" limits are typical of some, but not all, adsorption systems. Later in this chapter, we therefore consider the moderately anharmonic case, in an effort to apply the model desorption mechanism discussed above to the $CH_3F/NaCl$ adsorption system.

It is essential that we determine the timescales of the microscopic vibrational processes occurring in the adsorbate so that the macroscopic dynamics of photodesorption may be better understood. This is discussed in the next section. Macroscopic energy flow in the adsor-

bate is then considered in Section 4.3, where the possibility of vibrational energy leaking laterally out of the laser-illuminiated region on the surface is considered. Finally, the effect of V-V coupling on the photon-assisted pumping of higher adsorbate vibrational levels is calculated in a dynamic mean field theory of photodesorption in Section 4.4. The latter calculation, for a weakly anharmonic vibrational mode, supports the general predictions by Fain and Lin[38] discussed above.

4.2 Resonant V-V transitions

Vibrational energy transfer between identical adsorbed molecules is facilitated by their mutual interaction energy, which for large intermolecular separation is dominated by the dipole-dipole pair potential

$$V(r_1,r_2) = \frac{1}{4\pi\varepsilon_0} \frac{\mu_1\mu_2}{|r_1-r_2|^3} F \qquad (4.4)$$

where the two adsorbed molecules have positions on the surface given by r_1 and r_2 respectively. Their dynamic dipole moments, μ_1 and μ_2, are assumed to be aligned parallel, corresponding to an internal molecular vibrational mode oriented perpendicular to the surface. Here, ε_0 is the permitivity of free space and F is a correction factor that takes into account the electronic polarizability of the adsorbate and the image effects of the substrate. Since these two effects partially cancel one another[88], we will assume $F = 1$ to get order of magnitude estimates for the vibrational transition rate relevant for our

discussion. The internal molecular vibrational mode has energy levels $\hbar\varepsilon_{v_i}$ where $v_i = 0,1,2,\ldots$, for the i^{th} molecule in the adsorbate.

Vibrational energy transfer between two molecules, due to the interaction potential (4.4) induces V-V transitions $v_1 \to v_1-1$ with $v_2 \to v_2+1$. The transition probability per unit time for this near resonant process is given by

$$D_{v_2 v_1} = \frac{2\pi}{\hbar^2} \left| \frac{1}{4\pi\varepsilon_0 a_0^3} \langle v_1-1|\mu_1|v_1\rangle \langle v_2+1|\mu_2|v_2\rangle \right|^2 * \frac{1}{\pi} \frac{(\Gamma_1+\Gamma_2)/2}{(\varepsilon_{v_1-1}+\varepsilon_{v_2+1}-\varepsilon_{v_1}-\varepsilon_{v_2})^2 + (\Gamma_1+\Gamma_2)^2/4} \tag{4.5}$$

where the vibrational transitions are assumed to have Lorentzian line shapes with widths Γ_i given by the interaction with the substrate, and $a_0 = |r_2-r_1|$. This transition rate formula arises from taking the Fermi's golden rule expression[90] and integrating over the lineshapes of the vibrational modes of both molecules, and is valid for small linewidths, i.e., $\Gamma \ll \varepsilon_v$.

Equation (4.5) permits efficient vibrational transfer between identical molecules for resonant transitions, with $v_1 = v_2+1$. (Then $v_1 \to v_2$ and $v_2 \to v_1$.) Consider, for example, the adsorption system CH_3F on NaCl, with the infrared-active C-F vibrational mode assumed to be oriented perpendicular to the surface. The transition $v_1 = 1 \to 0$, $v_2 = 0 \to 1$, occurs with the rate $D_{01} = 2\cdot10^{11}\ s^{-1}$ for an intermolecular separation of $a_0 = 4$Å near full coverage; $D_{01} = 3\cdot10^{10}\ s^{-1}$ for $a_0 = 5.6$Å at partial coverage. (Here, typical parameters for the $v = 0 \to 1$ transition, $\Gamma_1 = \Gamma_2 = 20\ cm^{-1}$ and $\langle 0|\mu|1\rangle = .2$ D, were estimated from infrared

absorption data[68], letting F = 1.) It is clear that dipole-dipole coupling is sufficient to cause rapid vibrational transfer between adsorbed molecules. See Table 4.1 where similar data are included for

Table 4.1. Resonant V-V transfer (D_{01}) and vibrational decay (γ) constants, and V-V diffusion length (d) for adsorbed molecules with nearest neighbour distance a_0. A matrix-state example is included for comparison.

* Phonon-assisted vibrational damping rates calculated from (2.58) and (5.50) for the system parameters given in (2.91).

** Using $\langle 0|\mu|1\rangle \rightarrow 0.25D$; $\Gamma = 5cm^{-1}$; $\gamma = \Gamma$.[76,77]

*** See ref. 82.

System	a_0(Å)	$D_{01}(s^{-1})$	$\gamma(s^{-1})$	d(Å)
$CH_3F/NaCl$	4.0	$2\cdot10^{11}$	$2\cdot10^{9}$	<40
T = 100K	5.6	$3\cdot10^{10}$	to $2\cdot10^{11}$*	
CO/Cu(100)**	3.6	$\leq 3\cdot10^{12}$	$1\cdot10^{12}$	<6
T = 100K				
CO in				
Ar-matrix***	40	10^{7}	$7\cdot10^{1}$	10^{4}
T = 9K				

the CO/Cu(001) system as well. Note that vibrational damping, calculated in Section 5, can occur with rate γ on the same timescale as V-V transfer. This situation is in contrast to the matrix-isolation case in which both rates are drastically reduced and $D_{01} >> \gamma$ at low temperature.

Near-resonant transitions such as $v_1 = 1 \rightarrow 0$, $v_2 = 1 \rightarrow 2$ are also possible in equation (4.5), provided the vibrational anharmonicity is not

too great; that is, $\Delta = (\varepsilon_1 - \varepsilon_0) - (\varepsilon_2 - \varepsilon_1) < \Gamma$. On the other hand, for larger anharmonicity or for non-resonant vibrational transfer between different species, phonon assisted transitions can occur, as calculated for the matrix situation by Blumen et al.[88] Phonons enter the dipole coupling Hamiltonian in (4.4) because they modulate the relative position and orientation of the molecular dipoles, μ_1 and μ_2. Finally, we note that, for small intermolecular separations, short range chemical forces (neglected here) contribute to V-V transfer.

4.3 Macroscopic energy flow

The extent of macroscopic energy flow in the adsorbate due to microscopic V-V transitions is now assessed. To do so, assume, for simplicity, that each molecule interacts only with its neighbours according to (4.4) in a monolayer adsorbate that forms a square array with lattice spacing a_0. Adsorbed molecules experience vibrational damping by the substrate, characterised by the decay constant γ. Note that $\gamma < \Gamma$ because the vibrational linewidth, Γ, receives contributions from decay effects, as well as from dephasing and heterogeneity.[91]

Supposing an infrared laser illuminates a spot on the surface and resonantly excites molecular vibrations in this region of the adsorbate, one can estimate the efficiency with which vibrational energy is transported laterally out of this area. Resonant V-V transitions (4.5) permit this energy transfer along the surface, while vibrational damping sets the timescale, γ^{-1}, during which the process may occur. As shown in Table 4.1, vibrational lifetimes $\gamma^{-1} < 10^{-10}$ s are to be expected. In this short time, vibrational quanta cannot diffuse more

than a few lattice spacings outside the illuminated region.

Quantitatively, one can follow the hopping motion of a vibrational quanta which constitutes a symmetric random walk[92], in the direction perpendicular to the edge of the illuminated region. At the moderate laser intensities used in photodesorption experiments, rapid vibrational damping maintains a very low level of vibrational excitation within the irradiated region. As a result, excitation above the v = 1 level can be ignored and the random, lateral motion of independent vibrational quanta out of the illuminated area is described by the difference equation

$$\frac{d}{dt} P_i(t) = D_{01}(P_{i+1} + P_{i-1} - 2P_i) \qquad (4.6)$$

Here $P_i \ll 1$ is the probability of a vibrational quanta existing on the molecule at site i on an axis along the surface perpendicular to the edge of the lit region. This equation ignores vibrational damping to the substrate for now, and is to be solved for boundary conditions which place a finite vibrational excitation probability, P_o, on the boundary, i = 0.

It is straightforward to show that equation (4.6) leads to diffusive behaviour.[92] This implies immediately that vibrational energy spreads to a distance

$$d = a_o\sqrt{D_{01}\gamma^{-1}} \qquad (4.7)$$

outside the illuminated area, in the characteristic vibrational damping

time, γ^{-1}. Typical diffusion length estimates, d, are given in Table 4.1. Since $D_{10}\gamma^{-1} = O(1\text{-}100)$, it is concluded that energy transfer occurs over microscopic distances only, and there is no significant leakage of vibrational energy to the rest of the adsorbate. The fact that d is small justifies the use of a one-dimensional random walk model.

In conditions of high vibrational excitation, $v_i > 1$, one must consider transitions such as $(v_i \rightarrow v_i+1;\ v_{i+1} \rightarrow v_{i+1}-1)$ with corresponding rate $D_{v_i,v_{i+1}} = (v_i+1)v_{i+1}D_{01}$. This leads to the same difference equation (4.6) for the vibrational excitation level v_i, which is now not restricted to the low levels to which P_i was previously. We therefore expect the same result (4.7) independent of laser intensity.

Note that anharmonicity of the vibrational mode, which has been ignored here, has been considered in a detailed master equation approach by Manz for V-V transfer in the matrix state.[84] However, for a typical photodesorption system, anharmonic effects are not expected to significantly alter our main result. This conclusion stems from the observations that (i) vibrational damping is efficient at a surface and (ii) non-resonant V-V transition rates remain nearly symmetric in spite of vibrational anharmonicity provided the substrate temperature is not too low, as discussed earlier in Section 4.1.

Lateral energy transfer is equally well understood by studying the vibrational motion of the adsorbate in terms of collective phonon modes. Dipole-dipole nearest-neighbour coupling in an adsorbate that is weakly coupled to the substrate gives rise to damped normal vibrational modes consisting of transverse optical phonons localized in the adsorbate monolayer. Using the interaction model of Section 4.2, one

can calculate the dispersion relation, and thus the group velocity v_K of these phonons, given by

$$v_K = \frac{Q^2}{4\pi\varepsilon_o a_o^2 \mu\Omega} \sin(Ka_o) \; ; \; K = |K| \tag{4.8}$$

for

$$\Omega^2 >> \frac{Q^2}{4\pi\varepsilon_o a_o^3 \mu} \; . \tag{4.9}$$

Here, **K** is the phonon wave vector and is taken along a nearest neighbour direction on the surface. The limiting condition we find in (4.9) makes v_K very small, severely limiting lateral energy transfer. Specifically, we may construct a Boltzmann equation for the local phonon density, $n_K(\mathbf{x},t)$

$$\frac{\partial}{\partial t} n_K(\mathbf{x},t) + v_K \cdot \frac{\partial}{\partial \mathbf{x}} n_K(\mathbf{x},t) = \left(\frac{\partial n_K(\mathbf{x},t)}{\partial t} \right)_{coll} , \tag{4.10}$$

where **x** is the position vector in the surface plane. The collision term is taken in a relaxation time approximation[93] to model damping of phonon modes to the substrate with time constant assumed to be the vibrational decay time γ^{-1}.

Solving (4.10) with boundary conditions describing a quasi-steady state phonon population in the illuminated region, shows that the phonon occupation probability decays exponentially with distance outside this area. The characteristic decay length, $d = v_K \gamma^{-1}$, depends on phonon wavevector **K**. It is maximal for $K = \pi/2a_o$, and then agrees precisely with the earlier length estimate of (4.7). This represents an upper limit on d because phonon-phonon scattering in the adsorbate

(not included explicitly here) may not significantly populate high K modes, beginning from only the K = 0 modes excited directly by photon absorption. However, we clearly see that, whether the adsorbate vibrational modes are treated as localized or collective excitations, lateral energy transfer out of the illuminated region of the surface is negligible macroscopically, and therefore does not reduce the efficiency of the photodesorption process.

4.4 Microscopic V-V transfer in photodesorption

The effect of intermolecular vibrational transfer on laser-assisted vibrational pumping in the photodesorption process is now addressed. We specifically consider the case in which more than one quanta of vibrational energy is needed to stimulate desorption, as studied by Fain and Lin[38]. Recall that they employ a reduced master equation for the vibrational motion and allow laser-excitation from the ground vibrational level only. We now consider the effect of V-V coupling on photodesorption when direct laser-excitation of higher vibrational levels is still possible. This represents the small vibrational anharmonicity limit ($\Delta < \Gamma$), in contrast to the large anharmonicity case ($\Delta > \Gamma$) treated by Fain and Lin[38]. Experimental systems, for which Δ and Γ are both of the order of 10-30 cm^{-1}, fall in between these two limiting cases. For example, the CO/NaCl (100) adsorption system[94] has $\Delta = 25\ cm^{-1}$ and $\Gamma = 14\ cm^{-1}$, while $\Delta = 16\ cm^{-1}$* and

*For CH_3F/NaCl, we use Δ estimated from matrix[95] and gas phase results[96], which agree closely.

$\Gamma = 20\ cm^{-1}$ for $CH_3F/NaCl(100)$.

Our study of the photodesorption process is based again on the master equation (2.1) with one-phonon and one-photon-assisted transition probabilities given by (2.67) and (2.68). In this way, both the vibrational and translation motion of the gas molecules are treated explicitly. Intermolecular vibrational transitions in the adsorbate are now included in the master equation in a dynamic, self-consistent mean field theory. To do so, we begin by assuming that the many-body dynamics of the adsorbate layer are adequately described by the master equation

$$\frac{d}{dt}\, n(\mathbf{i},\mathbf{v};t) = \sum_{\mathbf{i},\mathbf{v}} S(\mathbf{i},\mathbf{v},\mathbf{i}',\mathbf{v}')n(\mathbf{i}',\mathbf{v}';t) \tag{4.11}$$

where $(\mathbf{i},\mathbf{v}) = i_1,v_1,\ldots,i_N,v_N$ describes a state of the adsorbate which contains N molecules, $n(\mathbf{i},\mathbf{v};t)$ is the occupation probability for this state, and $S(\mathbf{i},\mathbf{v},\mathbf{i}',\mathbf{v}')$ is the transition rate matrix. Its $(\mathbf{i},\mathbf{v},\mathbf{i}',\mathbf{v}')$-component is the transition rate from the state $(\mathbf{i}',\mathbf{v}')$ to $(\mathbf{i},\mathbf{v})$. We separate the rate matrix as

$$S(\mathbf{i},\mathbf{v};\mathbf{i}',\mathbf{v}') = R(\mathbf{i},\mathbf{v};\mathbf{i},\mathbf{v}') + V(\mathbf{i},\mathbf{v},\mathbf{i}',\mathbf{v}') \ . \tag{4.12}$$

Here, R includes transitions involving only one molecule, as given in Section 2, while V contains vibrational transfer between any two molecules, as given by (4.5). (See Appendix C for explicit definitions of R and V.)

The single molecule occupation probability is given by

$$n_\ell(i,v;t) = \sum_{(i,v)'} n(i,v;t) \tag{4.13}$$

where the primed sum goes over all (i,v) with the ℓ^{th} molecule held in the state (i,v). Performing this sum on the master equation (4.11) and letting i run over both bound and continuum states leads to the equation

$$\frac{d}{dt} n_\ell(i,v;t) = \sum_{i'v'} R_{ii'}^{vv'} n_\ell(i',v';t)$$

$$+ \sum_{k\neq\ell} \sum_{\substack{v'v'' \\ v'''i''}} V_{v'''v''}^{vv'}(r_k - r_\ell) n_{\ell k}(i,v';i''v'';t) \; . \tag{4.14}$$

Here, the two-molecule joint probability function is defined by

$$n_{\ell k}(i_\ell v_\ell, i_k, v_k;t) = \sum_{(i,v)''} n(i,v;t) \tag{4.15}$$

where the primed sum goes over all (i,v) with the ℓ^{th} molecule held in the state (i_ℓ, v_ℓ) and the k^{th} in the state (i_k, v_k). The first term in (4.14) describes transitions undergone by the ℓ^{th} molecule independently of its neighbours. This is just the rate process considered in Section 2. The second term describes vibrational transitions of the

ℓ^{th} molecule due to V-V transfer with its neighbours (labeled k). The rate factor $V_{v''_\ell v''_k}^{vv'}$ in (4.14) contains the vibrational transfer processes given by (4.5), and is defined in Appendix C.

Although equation (4.14) is an exact reformulation of the master equation (4.11), some approximations must be made in order to solve it. We first ignore pair correlations and write

$$n_{\ell k}(i_\ell v_\ell, i_k v_k; t) = n_\ell(i_\ell, v_\ell; t) n_k(i_k, v_k; t) \ . \qquad (4.16)$$

Averaging (4.14) over all N adsorbed molecules, and replacing n_k in (4.16) by the average probability (mean field approximation) leads to the equation

$$\frac{d}{dt} \bar{n}_i^v(t) = \sum_{i'v'} [R_{ii'}^{vv'} + W_{ii'}^{vv'}(t)] \bar{n}_{i'}^{v'}(t) \qquad (4.17)$$

where

$$\bar{n}_i^v(t) = \frac{1}{N} \sum_{\ell=1}^{N} n_\ell(i, v; t) \qquad (4.18)$$

and

$$W_{ii'}^{vv'}(t) = \delta_{ii'} \sum_{\alpha} \sum_{i^* v^*} [\delta_{v,v'+1} D_{v'v^*} + \delta_{v,v'-1} D_{v^*v'}] \bar{n}_{i^*}^{v^*}(t)$$

$$\text{for } iv \neq i'v', \qquad (4.19)$$

and

$$W_{ii}^{vv}(t) = -\sum_{i'v' \neq iv} W_{i'i}^{v'v}(t). \qquad (4.20)$$

The α-sum runs over all adsorbate molecule sites except a reference one, labeled $\alpha = 1$. ($D_{v'v}$ is given by (4.5), with $a_o = |r_\alpha - r_i|$.) The first term in the brackets in (4.19) describes vibrational excitation, $v' \to v'+1$, of a molecule by absorption of energy from a neighbour in the adsorbate; the second term refers to the de-excitation process, $v' \to v'-1$. Note that we can ignore summation terms in (4.19) for which $(i^*,v^*) = (i,v)$, as these processes merely exchange the states of two neighbouring molecules without altering the average occupation probabilities.

We see that the inclusion of dipole-dipole pair transitions, in the approximations described above, leads to an additional term (4.19) in the single molecule master equation (4.17). This extra rate term, $W_{ii'}^{vv'}(t)$, depends on the occupation functions $\bar{n}_i^v(t)$ which evolve with time. As a result, the rate matrix $R + W(t)$ is time dependent and the combination of (4.17) and (4.19) represents a nonlinear equation for $\bar{n}_i^v(t)$.

To study the desorption behaviour, we must solve this nonlinear master equation numerically. Starting from initial conditions of thermal equilibrium and then turning on the laser, an iterative procedure gives the evolution of the mean occupation probabilities, $\bar{n}_i^v(t)$. This involves calculating $W_{ii'}^{vv'}(t_k)$ at a given time t_k from $\{\bar{n}_i^v(t_k)\}$, and then letting the system evolve for a short time interval to t_{k+1} by assuming $W_{ii'}^{vv'}(t)$ is constant on this interval and diagonalizing the rate matrix as in Section 2.5. This gives the occupations at t_{k+1},

$\bar{n}_i^v(t_{k+1})$, which are used to calculate $W_{ii'}^{vv'}(t_{k+1})$ and hence the system evolution over a subsequent time interval. In this way, we calculate the decay of the adsorbate population, N(t), which may be expressed as

$$N(t) \propto \sum_{i,v} \bar{n}_i^v(t) = \sum_{\kappa} S_\kappa(t)\exp(-\lambda_\kappa(t)t) \ . \qquad (4.21)$$

Here $\{\lambda_\kappa(t)\}$ are the eigenvalues of the rate matrix (square brackets in equation (4.17)) which depends on time through the V-V coupling term, W. The prefactors $\{S_\kappa(t)\}$ are derived from the eigenvectors of the rate matrix, and also depend on the initial conditions.

As in Section 2.5.1, it is found that one eigenvalue, $\lambda_0(t)$, is typically several orders of magnitude smaller than the rest, and that its prefactor, $S_0(t)$, is correspondingly larger than the rest. Furthermore, it is found that $\{\lambda_\kappa(t)\}$ and $\{S_\kappa(t)\}$ stabilize at $\{\lambda_\kappa\}$ and $\{S_\kappa\}$, respectively, at early times, long before the adsorbate population has begun to decay in (4.21). These two theoretical results show that, after some fast transients have settled, the adsorbate population decays exponentially with the single rate constant λ_0 that is identified as the desorption rate, just as in Section 2 where V-V coupling was neglected.

We now present results separately for the harmonic and weakly anharmonic cases.

4.4.1 Harmonic vibrational mode

For a perfectly harmonic vibrational oscillator with anharmonic defect $\Delta = 0$, the desorption rate constant calculated above is found to be essentially unchanged from the very low coverage limit described in Section 2 where V-V coupling was neglected. The resonant vibrational coupling transitions included in (4.17) have no effect on the experimentally observable desorption rate, λ_0.

The transient behaviour can also be studied theoretically, although experimental observation is difficult because of the short timescales involved. (Typical laser pulse times used are longer than the transients.) At short times, $t < t_{trans}$, the individual parameters $\lambda_K(t)$ and $S_K(t)$ are not physically meaningful, but together they give the time dependent desorption rate, $r_d(t) = N(t)^{-1} \frac{d}{dt} N(t)$, using (4.21). It is found that $r_d(t)$ increases from an initial value at $t = 0$ corresponding to thermal desorption to a final value given by λ_0 over a transient timescale of the order of the vibrational damping rate constant, γ^{-1}. While V-V transition terms in the master equation alter the eigenvalues $\lambda_K(t)$ at these short times, the desorption rate $r_d(t)$ is unaffected. Thus, resonant vibrational transfer is found theoretically to have negligible influence on desorption on any timescale. This result, which is particular to the harmonic case, is explained below.

To understand the effects of vibrational coupling, we examine the form of the transition terms in (4.19). The resonant V-V coupling rates satisfy detailed balance if the occupation probabilities obey

$$\frac{n_i^{v+2}(t)}{n_i^{v+1}(t)} = \frac{n_i^{v+1}(t)}{n_i^{v}(t)} = r_i(t) \ . \qquad (4.22)$$

This condition is initially satisfied at t= 0 when the ratio in (4.22) is given by $r_i = e^{-\hbar\Omega/k_BT}$ in thermal equilibrium. However, the laser then drives the adsorbate out of equilibrium, through the transient regime, and finally into a quasistationary state from which desorption slowly proceeds. The quasistationary occupation probabilities calculated in (2.90) also obey (4.22) for the very low i-states that are most populated. However, $r_i(t)$ is much larger than its initial, thermal value. The fact that the desorption rate $r_d(t)$ is unaffected by the V-V transfer rates suggests that equation (4.22) is essentially valid (for low i-states) for all times, keeping the V-V rates in a state of detailed balance. This is not surprising, since (i) stepwise, photon-assisted vibrational excitation occurs with the slowest microscopic transition rate ($L^{v+1,v}$) of the whole system, and (ii) tunnelling transitions from excited bound states to the gas phase are slow compared to bound state-bound state relaxation rates.

4.4.2 Anharmonic vibrational mode

Moderate vibrational anharmonicity is now included in the desorption rate calculation. We let the anharmonic defect Δ be non-zero in the V-V transition rates (4.5), and must also alter the laser induced vibrational excitation rates $L^{v'v}$ in (2.49), as discussed in Section 6.3. The laser-assisted transition rates include anharmonic detuning effects through the lineshape function given in equation (6.3). A

laser tuned to excite the lowest vibrational transition, $v = 0 \to 1$, will be detuned by an amount $v\Delta$ from the $v \to v+1$ transition frequency, according to (4.2). This detuning results in slower laser-excitation of higher vibrational levels and consequently lower steady state occupations for $v > 1$ than that given by (4.22). The near-resonant vibrational transfer rates to these higher levels are also less efficient, but still satisfy detailed balance when (4.22) is obeyed. (On the other hand, phonon-assisted V-V transitions, while not calculated here, are no longer in detailed balance under condition (4.22) when $\hbar\Delta > k_B T$.) It is thus natural to expect that the photodesorption kinetics will be affected by V-V transfer when anharmonicity is significant.

Whether V-V transfer or laser excitation dominates in populating higher vibrational levels depends on their respective transition rates. Lacking a microscopic calculation of phonon-assisted vibrational transfer at a surface, we are limited to the near resonant, or weakly anharmonic case.

Using the modifications outlined above, we calculate the photodesorption rate for the $CH_3F/NaCl$ system, including V-V transfer as before, but taking into account an anharmonic defect of $\Delta = 8\ cm^{-1}$.* It is assumed that the laser is tuned to resonance with the $v = 0 \to 1$ transition, i.e., $\Omega_\ell = \Omega$. The magnitude of the V-V coupling rates depends strongly on the adsorbate coverage, or intermolecular separation

---

*The measured anharmonicity[95] for $CH_3F/NaCl$ is a factor of 2 larger than that used here. The magnitude of the enhancement of desorption due to V-V coupling is thus somewhat underestimated in Fig.4.4. The discussion above is not altered by this fact.

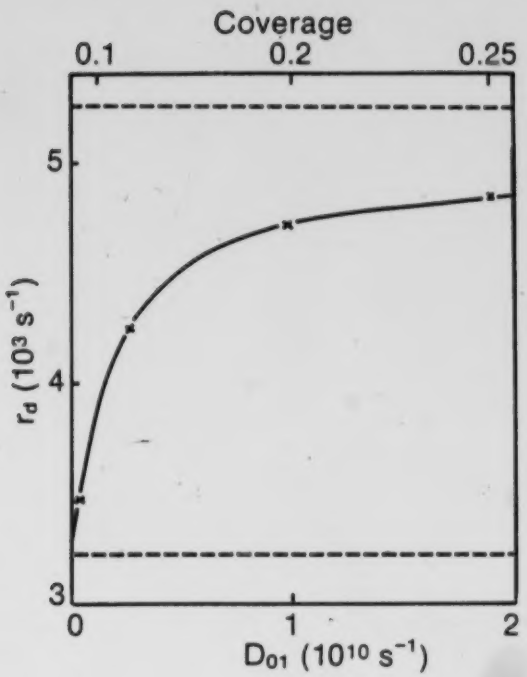

Fig.4.4. Photodesorption rate as a function of V-V transfer rate D_{01} for $CH_3F/NaCl$ at T = 50K and at laser intensity $\bar{I}$ = 1MW/cm². The vibrational anharmonicity is $\Delta = 8cm^{-1}$ and the linewidth is $\Gamma = 20cm^{-1}$. Other system parameters are given in (2.91). The upper (lower) dashed lines give the desorption rate calculated without V-V coupling in the harmonic (anharmonic) cases.

a_0. In Fig.4.4, the desorption rate constant, $r_d = \lambda_0$, is graphed as a function of the V-V transfer rate D_{01}, which is related by (4.5) to a_0 and hence coverage.

For large intermolecular separations, $a_0 > 16\text{Å}$, vibrational transfer is too slow to affect desorption. However, as the separation is decreased (by increasing coverage), the photodesorption rate con-

stant in Fig.4.4 increases. Finally, for coverages larger than 0.2, the desorption rate begins to level off at a value slightly less than the rate calculated from the model in Section 2 with anharmonicity and V-V coupling ignored.* The change-over region in Fig. 4.4 from the slow to fast vibrational transfer limits is centred at an intermolecular separation $a_0 \approx 10\text{Å}$, corresponding to a coverage of about 0.1 monolayers. The lateral V-V transfer rate at this coverage is given by $D_{01} \approx 2 \cdot 10^9\ s^{-1} \approx \gamma$, the vibrational damping constant for the $v = 1$ state. These features can be explained qualitatively by the simple model discussed below.

Intermolecular vibrational transitions act in parallel with laser-assisted vibrational excitation processes. Specifically, the $v = 1 \to 2$ transition is accessible by off-resonant photon absorption at a rate $L^{21}n^1$, and also via V-V transfer processes with transition rate $D_{11}n^1n^1$. The latter term is nonlinear in n^v, the occupation probability of the v^{th} vibrational level, since V-V coupling involves a pair of adsorbed molecules. As noted below equation (4.3) and derived in equation (2.89) with V-V transfer neglected, we find that $n^1 \approx L^{10}\gamma^{-1}\, n^0$. From these simple arguments, it is expected that V-V transfer dominates in exciting the $v = 1 \to 2$ transition if $D_{11}L^{10}\gamma^{-1} > L^{21}$, or equivalently, if $D_{01} > \gamma$. This is precisely the cross-over behaviour observed in Fig.4.4 as noted above. However, increasing V-V transition rates further does not lead to unlimited enhancement of the desorption rate. For $D_{01} \gg \gamma$, the V-V transfer processes saturate and maintain vibrational

---

*Our perturbation approach to the V-V transfer rates in the master equation solution breaks down for smaller separations, manifested by poor convergence in the numerical iteration.

level occupations $n^2/n^1 = n^1/n^0 = L^{10}\gamma^{-1}$ according to (4.22) for intensities much below saturation, as is approximately the case here (see Fig.2.7). These are the same occupation probabilities as expected in the harmonic case ($\Delta = 0$) with V-V coupling ignored (see Section 2.5). This explains the "high" coverage ($\theta > 0.1$ monolayer!) desorption kinetics seen in Fig.4.4. In arriving at these results, we have assumed that near-resonant V-V transfer dominates over phonon-assisted vibrational coupling. The latter process may be thermally activated and induces quite different behaviour in the fast V-V transfer limit. Specifically, the equilibrium condition (4.22) is altered to favour population of higher vibrational states, and the upper limit to the desorption rates in Fig.4.4 is raised. Recall that the result (4.3) derived by Fain and Lin[38] does not immediately show a finite, fast V-V transfer limit. This is due to neglecting slow V-V processes requiring thermal phonon absorption, as is valid for low temperatures $k_BT \ll \hbar\Delta$.

In summary, enhanced photodesorption yields are found if lateral vibrational transfer rates exceed the vibrational damping constant. The magnitude of the enhancement is greater for larger anharmonicity. In the fast V-V transfer limit and at not too low temperatures, the desorption rates for a laser tuned resonantly to $\Omega_\ell = \Omega$ approach those calculated previously in the harmonic case with V-V transitions neglected.

4.5 Discussion

It is clear that vibrational transfer processes take place within a homogeneous adsorbate during photodesorption experimental conditions.

However, it has been shown in Section 4.3 that macroscopic energy flow away from the laser-illuminated region is negligible. Efficient vibrational damping by the substrate severely limits lateral energy transport, even for fast V-V transfer conditions.

On the other hand, V-V transitions can enhance the laser-assisted pumping of higher vibrational states. For an harmonic vibrational oscillator, the macroscopic desorption kinetics is unchanged, both at short (transient) and longer times. In this case, vibrational transfer rates parallel already efficient laser-induced vibrational excitation processes. However, in the more realistic situations where vibrational anharmonicity is non-zero, photodesorption yields are enhanced if the V-V transfer rates exceed the vibrational damping constant, which occurs for the $CH_3F/NaCl$ system at all coverages greater than 0.1 monolayers. This result was shown in Fig.4.4 for a weakly anharmonic adsorption system for which $\Delta < \Gamma$ and supports similar results derived by Fain and Lin (4.3) for the strong anharmonicity ($\Delta > \Gamma$) case.[38]

5. Coherent Two-Quanta Processes

5.1 Introduction

In this chapter we calculate additional transition rate terms in the master equation for photodesorption. These terms, arising in higher perturbation theory, include the coherent absorption and/or emission of two phonons, two photons, or one photon plus one phonon by an adsorbed molecule. These processes give rise to transitions between states not directly accessible by a single one-quanta process. Since the coupling between the adsorbed molecule and the phonon bath is quite efficient, higher order coherent processes contribute significantly to the master equation, which already describes incoherent sequences of single phonon/photon-mediated transitions as described in Section 2. The calculation of these coherent two-quanta effects, based on the expansion of the transition rate formula (2.41), permits the extension of our results to more strongly bound adsorption sytems.[97]

Coherent multiphonon processes in thermal desorption have been previously addressed by several research groups and are discussed below. Bendow and Ying[12] have considered phonon-mediated desorption of an atom physically adsorbed in a shallow surface potential that develops a single bound state. They calculated multiphonon contributions to the desorption rate, given by the probability per unit time for a bound state to continuum state transition, in a three dimensional theory. An expansion of the transition matrix[98] yields the desired higher order terms which are computed numerically. The tran-

sition probability, calculated here to describe the coherent absorption of two phonons, includes the first order term in the interaction Hamiltonian

$$H_{int} = -a(t)V^{(1)}(x) + \frac{1}{2!}\, a^2(t)V^{(2)}(x) + \frac{1}{3!}\, a^3(t)V^{(3)}(x) + \ldots \qquad (5.1)$$

taken to fourth order in perturbation theory. (Recall that a(t) is the surface displacement, while $V^{(n)}(x)$ is the n^{th} derivative of the surface potential acting on the atom at x.)

Gortel, Kreuzer, and Teshima[99] have also treated thermal desorption from a single bound state. By iterating the Heisenberg equation for the adsorbate molecule field operator, the (desorption) transition probability was evaluated to fourth order in the phonon amplitude, a(t). Their calculation includes both vertex and self energy corrections, and receives contributions from the first three terms in (5.1). It was shown, for example, that interference between the two-phonon absorption process due to the second term in (5.1) taken to first order, and the first term in (5.1) taken to second order in perturbation theory, is very important. They find that absorption of a single phonon dominates in the desorption rate for a weakly bound atom provided the bound state energy is less than the maximum phonon energy. On the other hand, two-phonon absorption is essential when the binding energy becomes greater than the maximum phonon energy.[99]

Multiphonon effects in thermal desorption from more strongly bound systems which develop many bound states have been addressed by Jedrzejek et al.[13] They employ a master equation approach, in which

the transition rates contain the effect of the full interaction Hamiltonian in (5.1), but taken only to lowest order in perturbation theory. In this way, some of the coherent multiphonon contributions are included, and are found to play an important role in the desorption process. The inclusion of coherent multiphonon effects in photodesorption is thus of interest.

In this chapter, coherent multiphoton and multiphonon effects are now calculated for photodesorption systems developing many bound states, using a diagrammatic formalism as described in detail in Section 5.2. Coherent absorption and emission of two phonons, a necessary process for strongly bound adsorption systems where bound state energies are separated by more than the maximum phonon energy, is considered in Section 5.3. Since large laser intensities are used in photodesorption experiments, we calculate, in Section 5.4, the vibrational transition rate due to coherent absorption of two photons. This process is nonlinear in the laser intensiy. In addition, the coherent absorption/emission of one photon plus one phonon is considered in Section 5.5, and found to contribute asymmetrically to the photodesorption line shape as detailed in Section 6. In these calculations, certain higher order virtual processes must be accounted for in the form of self energy corrections. Finally, we include these coherent two-quanta transitions in the master equation and discuss their effect on the desorption kinetics in Section 5.6.

5.2 Formulation of the Transition Rate Calculation

The calculation of the transition rates is based on an expansion of the rate formula derived previously in Section 2.3. The phonon and

photon reservoirs of the solid and laser radiation respectively are described using thermal field theory methods. Higher order transition rate terms are then derived in perturbation theory. Bound state resonances necessitate the inclusion of molecular state line widths in the rates in our master equation.

5.2.1 Transition rate formula

Our task is to evaluate the transition rate for a single adsorbed molecule between state i and f, given in (2.41) as

$$R_{fi}(t) = \frac{d}{dt} \mathrm{Tr}_{s,\ell} \left[\langle i|U^{\dagger}(t)|f\rangle \langle f|U(t)|i\rangle \rho_s \rho_\ell \right]. \tag{5.2}$$

Recall that, in the appropriate time limits, this expression becomes independent of time. The trace operators in (5.2) run over all many particle states of the phonon and photon reservoirs. This makes higher order terms in a direct expansion of the evolution operator U(t) in (5.2) quite complicated. To overcome this problem, we adopt the methods of Thermo Field Dynamics (TFD)[100] to describe the phonon and photon systems. This approach is advantageous over the more conventional techniques of thermal field theory[101] because it is compatible with our time-dependent formalism and is also capable of describing the non-thermal photon states of the laser radiation.

Using the theory of TFD, averaging over the states of the phonon and photon reservoirs is accomplished by taking an expectation value given by

$$\mathrm{Tr}_{s,\ell}[A(t)\rho_s\rho_\ell] = \langle\beta|\langle I|A(t)|I\rangle|\beta\rangle. \tag{5.3}$$

The operator $A(t)$ is an arbitrary function of the phonon and photon amplitudes. It is averaged by taking its expectation value in the "thermal phonon ground state" $|\beta\rangle$ of the solid, and in the "photon ground state" $|I\rangle$ of the laser radiation. The former is characterized by the inverse temperature, β, of the solid, while the latter depends on the intensity distribution, I_k, of the laser radiation. The information stored in the reservoir density matrices, ρ_s and ρ_ℓ, is now contained in the states $|\beta\rangle$ and $|I\rangle$, respectively. The field operators for which $|\beta\rangle$ and $|I\rangle$ are ground states are related to the original phonon and photon fields by unitary transformations,[100] as described later.

Substituting (5.3) into (5.2) gives

$$R_{fi}(t) = \frac{d}{dt}\left[\langle\beta|\langle I|\langle i|U^\dagger(t)|f\rangle\langle f|U(t)|i\rangle|I\rangle|\beta\rangle\right]. \tag{5.4}$$

We now define the identity operator in the reservoirs' state space to be

$$I = \sum_{n_s(\beta)} \sum_{n_\ell(I)} |n_s(\beta)\rangle|n_\ell(I)\rangle\langle n_\ell(I)|\langle n_s(\beta)|. \tag{5.5}$$

Here, $n_s(\beta)$ represents a state of the transformed "thermal" phonon field, with respect to the "thermal" ground state $|\beta\rangle$ of the solid. Similarly, $n_\ell(I)$ denotes a state of the transformed photon field with

respect to its ground state $|I\rangle$. The sums in I run over all such states. Inserting this identity into (5.4) leads to the single molecule transition rate

$$R_{fi}(t) = \frac{d}{dt} \sum_{n_s(\beta)} \sum_{n_\ell(I)} |\langle n_\ell(I), n_s(\beta), f|U(t)|i, \beta, I\rangle|^2. \tag{5.6}$$

The sum over $n_s(\beta)$ and $n_\ell(I)$ above enables us to classify contributions to $R_{fi}(t)$ in terms of one and two phonon/photon absorption or emission processes, and so on. For a given term in the sum in (5.6), the transition rate is just the time derivative of a squared transition amplitude.

The rate $R_{fi}(t)$ in (5.6) must be calculated in the time limit given in (2.42). Anticipating the inclusion of molecular self energy (line width) corrections (5.59) in the expansion of (5.6), we must consider times large on the scale of the inverse line width, $(\omega_D \sigma_{iv})^{-1}$. On the other hand, the transient evolution of a molecule driven out of thermal equilibrium by the laser occurs on the rate scale of the vibrational decay constant γ. We verify by explicit calculation, the separation of time scales relevant to (5.6) as given below

$$(\omega_D \sigma_{iv})^{-1} \ll t \ll \gamma^{-1} . \tag{5.7}$$

Note that the surface bond states are primarily lifetime broadened, making a conventional rapid dephasing approximation inapplicable. This limit amounts to taking $t \to \infty$ in (5.6) and corresponds to the

usual long time limit encountered in deriving the Fermi's golden rule expressions as seen already in Section 2.4.

For future convenience, we do the time derivative in (5.6) explicitly using (2.35). This leads, in the time limit described above and after a few manipulations, to the time-independent transition rate

$$R_{fi} = \sum_{n_s(\beta)} \sum_{n_\ell(I)} \langle n_\ell(I), n_s(\beta), f | U(\infty) | i, \beta, I \rangle$$

$$* \langle n_\ell(I), n_s(\beta), f | U(\infty)\ (H_{int}(0))/i\hbar\ | i, \beta, I \rangle^* + \text{complex conj.} \quad (5.8)$$

The thermal phonon and photon fields (and states $n_s(\beta)$ and $n_\ell(I)$) introduced above are now described in detail.

5.2.2 Description of the reservoirs with Thermo Field Dynamics

Some basic elements of the TFD theory are now introduced, so that the thermal ground state can then be defined. Details are found in the text on this subject by Umezawa, Matsumoto, and Tachiki,[100] and in earlier papers referenced there. First consider the free phonon field, introduced in (2.27), with annihilation and creation operators b_p and $b_p^\dagger$, respectively. The quantum index $p = (p,\sigma)$ describes phonon wavevector and polarization. The many phonon states N_s of the solid are defined below equation (2.44).

We now associate with the phonon field a duplicate field built up from a duplicate set of phonon operators, $\tilde{b}_p$ and $\tilde{b}_p^\dagger$. This second,

independent "tilde"-field is introduced for mathematical reasons that are discussed below. The many "tilde"-phonon states of this field are denoted $\tilde{N}_S$, in a one to one correspondence with the original phonon states, N_S. The thermal phonon ground state is then given by

$$|\beta\rangle = \rho_S^{1/2} \sum_{N_S} |N_S\rangle |\tilde{N}_S\rangle, \tag{5.9}$$

where

$$\rho_S = \frac{e^{-\beta H_S}}{Tr_S[e^{-\beta H_S}]}, \tag{5.10}$$

with H_S defined in (2.31). This form for $|\beta\rangle$, along with the analogous photon ground state $|I\rangle$, satisfies equation (5.3), as required. The inclusion of the "tilde"-states in (5.9) is crucial to the evaluation of the thermal expectation value,

$$\langle\beta|A(t)|\beta\rangle = \sum_{N_S} \sum_{N_S'} \langle N_S|\rho_S^{\frac{1}{2}} A(t) \rho_S^{\frac{1}{2}} |N_S'\rangle \langle \tilde{N}_S|\tilde{N}'_S\rangle$$

$$= \sum_{N_S} \langle N_S|\rho_S A(t)|N_S\rangle$$

$$= Tr[\rho_S A(t)], \tag{5.11}$$

since the term $\langle \tilde{N}_s \,|\tilde{N}_{s'}\rangle = \delta_{N_s,N_{s'}}$ reduces the double sum above to a single one. The physical significance of the duplicate phonon field will be seen after considering the transformed, thermal phonon fields for which $|\beta\rangle$ is the ground state.

The "thermal" field operators, $b_p(\beta)$ and $\tilde{b}_p^{\dagger}(\beta)$, are related to the original phonon field b_p and its duplicate $\tilde{b}_p$ by the unitary transformation[100]

$$b_p = \cosh\theta_p \, b_p(\beta) + \sinh\theta_p \, \tilde{b}_p^{\dagger}(\beta)$$

$$\tilde{b}_p^{\dagger} = \sinh\theta_p \, b_p(\beta) + \cosh\theta_p \, \tilde{b}_p^{\dagger}(\beta), \tag{5.12}$$

By defining the thermal phonon operators in this way, the Boson commutator is preserved by the transformation. By combining (5.12) (inverted) with (5.9) and (5.10), it is verified that

$$b_p(\beta)|\beta\rangle = 0 = \tilde{b}_p(\beta)|\beta\rangle, \tag{5.13}$$

provided we define

$$\sinh\theta_p = (n_p^s)^{1/2} = \left[\frac{1}{e^{\beta\hbar\omega_p}-1}\right]^{1/2}. \tag{5.14}$$

This condition defines the unitary transformation (5.12), and hence the thermal operators.

The thermal field operators, $b_p(\beta)$ and $\tilde{b}_p(\beta)$, have independent physical roles. Consider for a moment the original phonon operators, b_p

and $b_p^\dagger$. Since $|\beta\rangle$, defined in (5.9), contains excited phonon states,

$$b_p|\beta\rangle \neq 0 \quad \text{and, of course,} \quad b_p^\dagger|\beta\rangle \neq 0. \tag{5.15}$$

This means simply that it is possible to both annihilate an excited phonon mode contained in $|\beta\rangle$, and to create an additional excitation of the p^{th} mode in $|\beta\rangle$. Let us now see how the thermal phonon operators are used to perform these two independent processes. Clearly, $b_p^\dagger(\beta)$ creates an additional phonon excitation when it operates on $|\beta\rangle$. However, equation (5.13) sets $b_p(\beta)|\beta\rangle = 0$, so we need to use the additonal, tilded thermal operator $\tilde{b}_p^\dagger(\beta)$ to independently annihilate phonon modes in $|\beta\rangle$ by creating "thermal holes".

While the discussion above dealt specifically with the phonon reservoir, the laser photon field is treated in an analogous fashion. We construct the new photon ground state, similarly to (5.9), given by

$$|I\rangle = \rho_\ell^{1/2} \sum_{N_\ell} |N_\ell\rangle|\tilde{N}_\ell\rangle. \tag{5.16}$$

Here, ρ_ℓ is chosen to describe the steady state intensity spectrum of the laser radiation. The photon field operators obey

$$C_k = \cosh\theta_k\, C_k(I) + \sinh\theta_k\, \tilde{C}_k^\dagger(I)$$

$$\tilde{C}_k^\dagger = \sinh\theta_k\, C_k(I) + \cosh\theta_k\, \tilde{C}_k^\dagger(I) \tag{5.17}$$

where $\sinh\theta_k = (n_k^\beta)^{1/2} \propto I_k^{1/2}$. (See equation (2.48) relating n_k^β to the intensity distribution I_k. Here $k = (k,\beta)$ denotes photon wave vector and polarization.) The operators $C_k^\dagger(I)$ and $\tilde{C}_k^\dagger(I)$ create photon excitations and holes, respectively, with respect to the intensity distribution described by the ground state $|I\rangle$.

The equations of motion of the "tilded" fields are similar to those for the original fields. For example, the original phonon annihilation operator, b_p, obeys the Heisenberg equation

$$i\hbar \frac{d}{dt} b_p(t) = [b_p(t), H_s], \tag{5.18}$$

which gives

$$b_p(t) = b_p e^{-i\omega_p t} \tag{5.19}$$

using H_s in (2.31) and Boson commutator $[b_p(t), b_q^\dagger(t)] = \delta_{p,q}$. On the other hand, the Heisenberg equation for $\tilde{b}_p$ has a negative sign in front of the time derivative in (5.18) which leads to

$$\tilde{b}_p(t) = \tilde{b}_p e^{i\omega_p t}. \tag{5.20}$$

The positive frequency associated with the "tilded" operator above is consistent with earlier identification of $\tilde{b}_p^\dagger(\beta)$ with the creation of thermal holes.[100] The theory described above is now applied to the transition rate calculation.

5.2.3 Perturbation expansion of the transition rate

To calculate the transition rates, the matrix elements in the formula given in (5.8) are simplified by expanding the evolution operator U(t) in powers of the interaction Hamiltonian according to (2.35). The appropriate formulae are given below, before describing their evaluation using Feynman diagram techniques.

$$\langle n_\ell(I), n_s(\beta), f | U(\infty) | i, \beta, I \rangle = \sum_{n=1}^{\infty} \frac{1}{n!} \left(\frac{1}{i\hbar} \right)^n \int_0^\infty d\tau_1 \ldots d\tau_n$$
$$* \langle n_\ell(I), n_s(\beta), f | T\, H_{int}(\tau_1) \ldots H_{int}(\tau_n) | i, \beta, I \rangle \qquad (5.21)$$

and

$$\langle n_\ell(I), n_s(\beta), f | U(\infty)\, (H_{int}(0))/i\hbar\, | i, \beta, I \rangle =$$
$$\langle n_\ell(I), n_s(\beta), f | (H_{int}(0))/i\hbar\, | i, \beta, I \rangle$$
$$+ \sum_{n=1}^{\infty} \frac{1}{n!} \left(\frac{1}{i\hbar} \right)^n \int_0^\infty d\tau_1 \ldots d\tau_n$$
$$* \langle n_\ell(I), n_s(\beta), f | T\, H_{int}(\tau_1) \ldots H_{int}(\tau_n)\, (H_{int}(0))/i\hbar\, | i, \beta, I \rangle \; . \qquad (5.22)$$

The "final" state appearing here

$$|f, n_s(\beta), n_\ell(I)\rangle = |f\rangle |n_s(\beta)\rangle |n_\ell(I)\rangle$$

is constructed using the molecular and thermal field operators according to $|f\rangle = \alpha_f^\dagger |0\rangle$, ($|0\rangle$ is the vacuum state for the molec-

ule field.)

$$|n_s(\beta)\rangle = |n_{p_1}, n_{p_2}, \ldots\rangle\, |\tilde{n}_{p_1}, \tilde{n}_{p_2}, \ldots\rangle = \prod_i \frac{[b_{p_i}^\dagger(\beta)]^{n_{p_i}}\, [\tilde{b}_{p_i}^\dagger(\beta)]^{\tilde{n}_{p_i}}}{(n_{p_i}!\tilde{n}_{p_i}!)^{1/2}}\, |\beta\rangle$$

and

$$|n_\ell(I)\rangle = |n_{k_1}, n_{k_2}, \ldots\rangle\, |\tilde{n}_{k_1}, \tilde{n}_{k_2}, \ldots\rangle = \prod_i \frac{[C_k^\dagger(I)]^{n_{k_i}}\, [\tilde{C}_k^\dagger(I)]^{\tilde{n}_{k_i}}}{(n_{k_i}!\tilde{n}_{k_i}!)^{1/2}}\, |I\rangle . \quad (5.23)$$

The final state of the phonon (and photon) reservoir for a given transition is expressed in (5.23) in terms of the excitation of thermal particles with respect to the thermal ground state. By choosing $|n_s(\beta)\rangle = |\, p, \tilde{q}\,\rangle = b_p^\dagger(\beta)\tilde{b}_q^\dagger(\beta)|\beta\rangle$ for example, we single out molecular transitions that involve emission of a thermal phonon with quantum number p, and absorption of a thermal phonon, q. This classification of molecular transitions in terms of real thermal phonon processes is not necessarily equivalent to the analogous classification in terms of "original"-phonon processes as used in Chapter 2. However, at the tree diagram level, that is without self energy or vertex corrections included, these two classification schemes yield identical transition amplitudes.

The matrix elements appearing in (5.21) and (5.22) have operator parts (see H_{int} in (2.12), (2.23), (2.30), and (2.32)) of the form

$$\langle f|T\psi^\dagger(y_1,\tau_1)\psi(y_1,\tau_1)\ldots\psi^\dagger(y_n,\tau_n)\psi(y_n,\tau_n)|i\rangle \; * \; \langle n_s(\beta)|T\; a(\tau_1)\ldots a(\tau_\ell)|\beta\rangle$$

$$* \langle n_\ell(I)|TA(\tau_{\ell+1})....A(\tau_m)|I\rangle; \quad 0 \leqslant \ell \leqslant m \leqslant n \qquad (5.24)$$

(Here, $y = (x,\xi)$) The phonon field $a(t)$ and the photon field $A(t) = \mathbf{n}\cdot\mathbf{A}(t)$ are expressed in terms of the "thermal" operators, $b_p(\beta)$ and $C_k(I)$ respectively. The matrix elements of interest above involve only ground states or few thermal-particle excited states. As a consequence, it is fruitful to apply Wick's theorem to the thermal operators, leading to a standard Feynman diagram analysis.[58] The diagram rules are given explicitly in Appendix D. Only the highlights of the expansion are outlined below.

The kinds of molecular transitions permitted are governed by the interaction Hamiltonian. The different terms in H_{int} are shown pictorailly in Fig.5.1, corresponding to the diagram vertices listed in Appendix D. The basic processes from which the transition amplitude is built up are:

(a) single photon absorption or emission by the molecular vibrational mode;

(b) absorption/emission of n phonons, corresponding to the n^{th} derivative of the surface potential in the phonon interaction;

and

(c) direct tunnelling between molecular states due to the residual coupling between the translational and vibration modes of the adsorbed molecule.

Combinations of these processes are included in the transition elements in (5.21) and (5.22). In the expansion of these transition amplitudes, it is convenient to re-group the terms in (5.21) and (5.22) according to classes of diagrams constructed from irreducible vertex

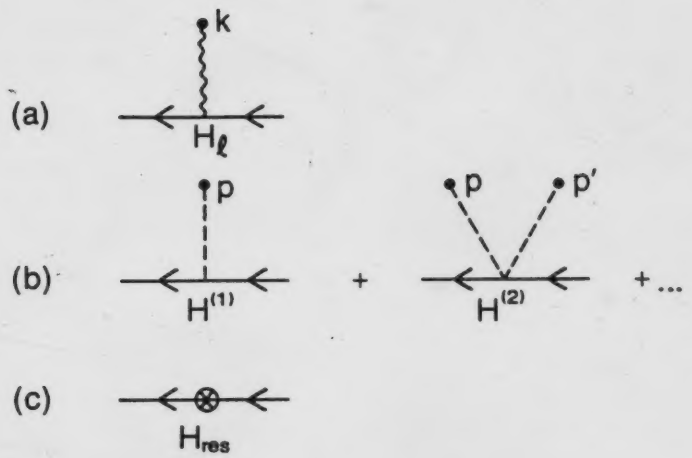

Fig.5.1. Interaction processes due to H_{int}. Solid, broken, and wavy lines represent the adsorbed molecule, phonons and photons, respectively. In (b), we define $H^{(n)} = (-1)^n/n!\ a(t)^n V^{(n)}(x - \mu/m_1, \xi)$.

and propagator parts.[58] This allows for a straightforward separation of transition rate terms based on the number of real phonons or photons absorbed or emitted to the reserovirs. We therefore re-write the transition amplitude in (5.21) in terms of these composite diagrams, as described in general in Appendix D.

The transition amplitudes involving absorption or emission of one or two real phonons/photons correspond to the diagrams in Fig.5.2, which represent the formulae given below. For example, the term for absorption of one real phonon (p), in the overall amplitude $\langle n_\ell(I), n_s(\beta), f|U(\infty)|i,\beta,I\rangle$, is written as

$$A_{fi}^{(1)}(\bar{p}) = \langle I,\bar{p},f|U(\infty)|i,\beta,I\rangle$$

$$= \sum_{j_1 j_2} \frac{1}{2\pi} \int d\omega\, G_{fj_1}^{out}(-\omega)\, V_{j_1 j_2 p}\, G_{j_2 i}^{in}(\omega+\omega_{\bar{p}}). \quad (5.25)$$

$$(\omega_{\bar{p}} = -\omega_p)$$

Here, G^{out} and G^{in} are Green's functions connecting the final and initial states, respectively, and are defined shortly. The irreducible vertex function, $V_{j_1 j_2 p}$ describes absorption of a phonon mode p while transferring the molecule from state j_2 to j_1. (The absorption of a phonon is represented by the creation of a thermal hole, $\bar{p}$, in the final state; phonon emission involves creation of a thermal phonon, p, instead.) The amplitudes for absorption or emission of a single photon mode k, $A_{fi}^{(1)}(\bar{k})$ and $A_{ji}^{(1)}(k)$ respectively, are defined in analogy with (5.25), but involve the one photon vertex $V_{j_1 j_2 k}$ instead.

The amplitude for the emission of two real phonons, p and p',contains three terms shown in Fig.5.2(d), corresponding to

$$\langle I,pp',f|U(\infty)|i,\beta,I\rangle = A_{fi}^{(2)}(p,p') + A_{fi}^{(2)}(p',p) + A_{fi}^{(1)}(p,p') \quad (5.26)$$

where

$$A_{fi}^{(2)}(p,p') = \sum_{j_1 \ldots j_4} \frac{1}{2\pi} \int d\omega\, G_{fj_1}^{out}(\omega)\, V_{j_1 j_2 p}\, G_{j_2 j_3}(\omega+\omega_p) V_{j_3 j_4 p'}$$

$$* G_{j_4 i}^{in}(\omega+\omega_p+\omega_{p'}) \quad (5.27)$$

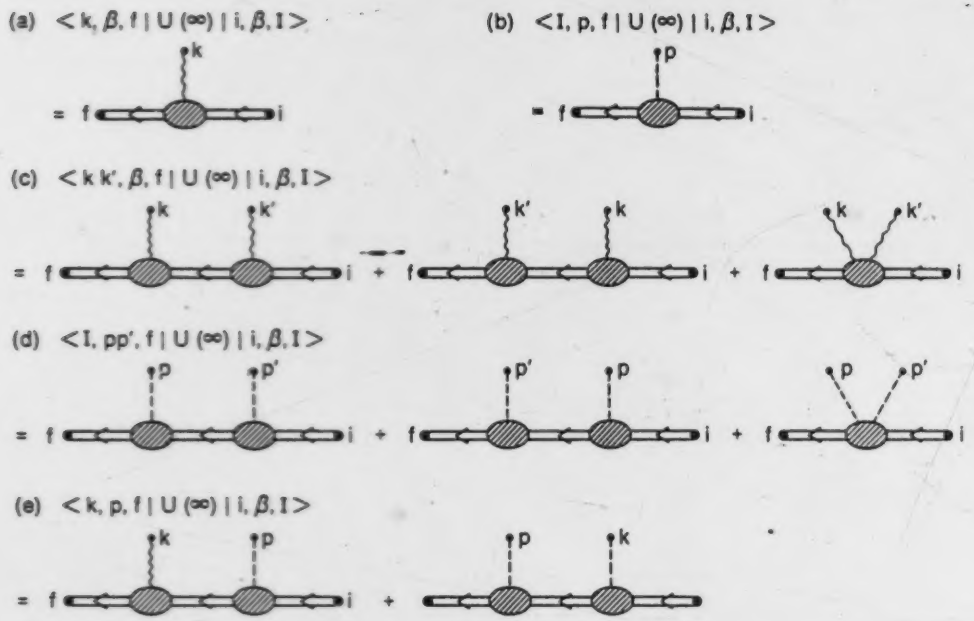

Fig.5.2. Transition amplitudes containing one or two real quanta. One and two photon processes are given by (a) and (c), respectively, while one and two phonon processes are shown in (b) and (d). In (e), the one-phonon plus one-photon process is given.

and

$$A_{fI}^{(1)}(p,p') = \sum_{j_1 j_2} \frac{1}{2\pi} \int d\omega \; G^{out}_{fj_1}(-\omega)\; V_{j_1 j_2 pp'}\; G^{in}_{j_2 I}(\omega+\omega_p+\omega_{p'}) \qquad (5.28)$$

The irreducible vertex functions, such as the two-phonon vertex $V_{j_1 j_2 pp'}$ occurring above, are expanded graphically in Fig.5.3. The two-photon and one-phonon plus one-photon processes given in Fig.5.2(c) and

(e) are defined in a similar manner, amounting to replacing the phonons (p's) with photons (k's) in equations (5.26) to (5.28).

While the above discussion and Fig. 5.2 refer to the transition amplitude $\langle n_\ell(I), n_s(\beta), f | U(\infty) | i, \beta, I \rangle$, the transition rate in formula (5.8) also contains the amplitude $\langle n_\ell(I), n_s(\beta), f | U(\infty) H_{int}(0)/i\hbar | i, \beta, I \rangle$. This latter amplitude is calculated from the same diagrams given in Fig. 5.2, but with a modified molecular Green's function, $G^{in'}$ defined by

$$G^{in}(y,t;f)' = \delta(t) G^{in}(y,t;f) \quad , \tag{5.29}$$

replacing G^{in} in (5.25) to (5.28) (see also equation (5.30) below). In this way, the $H_{int}(0)/i\hbar$ factor is taken into account.

The molecular Green's functions, G^{out}, G, and G^{in} are defined in coordinate space to be

$$G(y,y',t) = \langle I, \beta, 0 | T \psi_H(y,t) \psi_H^\dagger(y',0) | 0, \beta, I \rangle,$$

$$G^{out}(y,t;f) = \langle I, \beta, f | \psi_H^\dagger(y,t) | 0, \beta, I \rangle$$

and

$$G^{in}(y,t;i) = \langle I, \beta, 0 | \psi_H(y,t) | i, \beta, I \rangle, \tag{5.30}$$

where the Heisenberg field of the molecule, ψ_H, is related to interaction picture operator, ψ (2.9), by

$$\psi_H(y,t) = U^\dagger(t)\psi(y,t)U(t). \qquad (5.31)$$

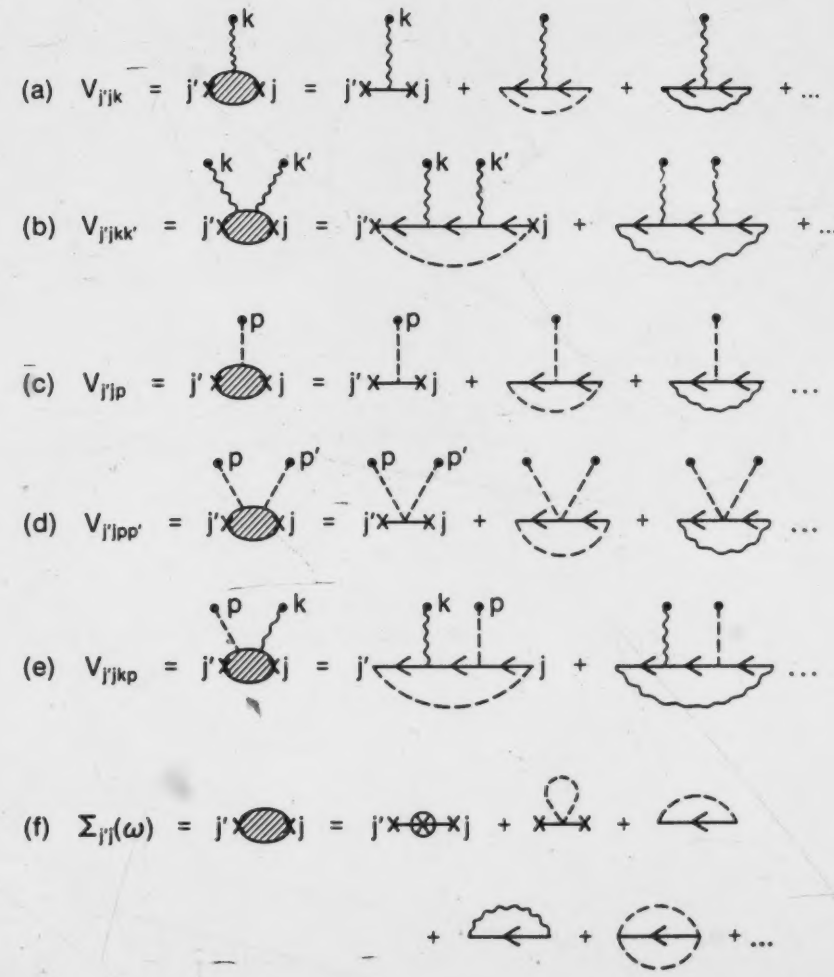

Fig.5.3. Irreducible vertices and the self energy insertion. One and two photon vertices are given in (a) and (b) respectively, while the one and two phonon are shown in (c) and (d). In (e), the one-photon plus one-phonon vertex is shown, and the molecule self energy is given (f).

The "Fourier" transformed propagators appearing in the amplitudes (5.25) to (5.28) are then defined as

$$G_{jj'}(\omega) = \int_{-\infty}^{\infty} dtdydy' \; \Phi_j^*(y)G(y,y',t)\Phi_{j'}(y')e^{i\omega t} \,, \tag{5.32a}$$

$$G_{fj}^{out}(\omega) = \int_{-\infty}^{\infty} dtdy \; G_{out}(y,t;f)\Phi_j(y)e^{i\omega t}, \tag{5.32b}$$

and

$$G_{jI}^{in}(\omega) = \int_{-\infty}^{\infty} dt \; dy \; \Phi_j(y)G_{in}(y,t;i)e^{i\omega t}, \tag{5.32c}$$

where $\Phi_j(y) = \phi_j(x)u_v(\xi)$ is the molecular wavefunction defined by (2.7). While the invariance of H_{int} under time translation make the Fourier transform from $t \to \omega$ useful, the spatial translational symmetry is broken by the surface potential, making the momentum representation unhelpful here. (Recall that our theory is one dimensional.) Instead, we transform from the space coordinate $y = (x,\xi)$ to the molecular state index $j = (j,v)$ above, using the kernel $\Phi_j(y)$.

Dyson's equations[101] are constructed to describe these full propagators in terms of the corresponding bare propagators and the molecular self-energy insertion, as shown in Fig. 5.4. The bare propagators, representing a non-interacting adsorbed molecule in the absence of phonons and photons, are defined by replacing ψ_H with ψ in (5.30),

leading to

$$S_{jj'}(\omega) = \delta_{jj'} \frac{i}{\omega-\varepsilon_j+i\gamma} = \delta_{jj'} S_j(\omega) \tag{5.33a}$$

$$S_{fj}^{out}(\omega) = 2\pi\delta_{fj}\,\delta(\omega+\varepsilon_f), \tag{5.33b}$$

$$S_{ji}^{in} = S_{ji}(\omega), \tag{5.33c}$$

and

$$S_{ji}^{in}(\omega)' = \delta_{ji}\,. \tag{5.33d}$$

In these equations, ε_j is the energy (divided by $\hbar$) of the j^{th} state of an adsorbed molecule, and γ is positive, real and infinitesimal. The energy delta function in (5.33b) removes the single integration over ω in the amplitudes $A_{fi}^{(n)}$ given in (5.25) to (5.28). Note that the bare propagators above are diagonal in the molecular state index j, whereas the full propagations in (5.32) have off-diagonal components. This is due to off-diagonal terms in the self-energy insertion, $\Sigma_{jj'}(\omega)$, which is expanded diagramatically in Fig.5.3(f). The Dyson equation represented by Fig.5.4(a) is

$$G_{jj'}(\omega) = S_{jj'}(\omega) + \sum_{j_1 j_2} S_{jj_1}(\omega)\,\Sigma_{j_1 j_2}(\omega) G_{j_2 j'}(\omega). \tag{5.34}$$

Replacing G and S here with G^{out} and S^{out} gives the corresponding

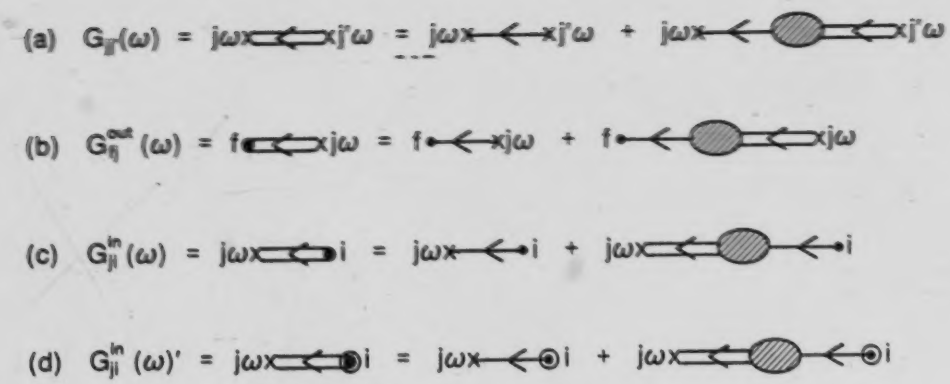

Fig.5.4. Green's functions for adsorbed molecule. Double (single) lines are full (bare) Green's functions, and the shaded oval is the self energy insertion shown in Fig.5.3(f).

equation for Fig.5.4(b), and so on.

For completeness, we define here the phonon propagator

$$D(t) = \langle \beta | Ta(t)a(0) | \beta \rangle. \tag{5.35}$$

in terms of the phonon-induced surface displacement a(t), and the photon propagator

$$E(t) = \langle I | TA(t)A(0) | I \rangle \tag{5.36}$$

These are both bare propagators for non-interacting Boson fields. The phonons and photons do not receive self-energy corrections because we

only consider their interaction with the adsorbed molecule. Since the molecule field does not contain antiparticle ("hole") states, molecule-loop diagrams are identically zero, leading to zero self-energy corrections to the phonon and photon propagators.

In principle, the transition rate calculation now amounts to: (i) evaluating the vertex functions and self-energy corrections as expanded in Fig.5.3 to the desired accuracy, (ii) solving the matrix equations (5.34) for the molecular propagators, and (iii) substituting these quantities into the formulae (5.25) to (5.27) for the transition amplitudes which lead directly to the transition rate R_{fi}. In practice, we calculate the vertex functions to lowest order, keeping only the first diagram in each line of Fig. 5.3a,c,d, and ignoring the two-photon and one-phonon plus one-photon vertices in Fig. 5.3 (b and e) altogether. The higher order terms in these expansions are expected to provide small, quantitative corrections to the vertex functions, but will not cause qualitative differences.

We do include self-energy corrections to the molecule propagator by evaluating the diagrams shown in Fig. 5.3f. To reduce the complexity of the calculation of $G_{jj'}$ in (5.34), off-diagonal terms, $j_1 \neq j_2$ in $\Sigma_{j_1 j_2}$ are ignored. The Dyson equation is then trivial to solve, leading to an approximate molecular propagator

$$G^{f}_{jj'}(\omega) = [1 - S_{jj'}(\omega)\Sigma_{j'}(\omega)]^{-1} S_{jj'}(\omega)$$

$$= \delta_{jj'} \frac{1}{\omega - \varepsilon_j - i\Sigma_j(\omega)}$$

$$= \delta_{jj'} G^{0}_{j}(\omega). \qquad (5.37)$$

The diagonal self-energy corrections, $\Sigma_j(\omega)$, are in general complex-valued, contributing both an energy shift and linewidth to the molecule states j. We will ignore the energy shift, assuming that it is, for a given temperature and laser intensity, already contained in the energy levels ε_j. (The laser-induced contributions to the self-energy are, in fact, negligible at typical intensities below the saturation region.) The line width contribution, due to the imaginary part of $i\Sigma_j(\omega)$, must be retained to prevent the two-quanta transition rates from diverging, as discussed in the next subsection. Broadening the lineshape of the bound state energies ε_i reflects the fact that these states are in actuality quasi-stable, and therefore not discrete.

The propagators G^{out}, G^{in}, and $G^{in'}$, corresponding to external lines in Fig.5.2, cannot be dressed as described above. If one solves a Dyson equation like (5.34) for the dressed external propagators, the resulting transition amplitude is zero. This fact is related to the time limit taken in (5.7) and to quasistability of the molecular states, and can be understood as follows. Note that the Dyson equation gives the molecular energy levels finite linewidths arising from decay and dephasing effects. We evaluate the transition rate for times long compared to the inverse linewidth, but still short compared to the relevant transient repopulation times. In this time limit, the transition amplitude has already decayed due to initial and final state linewidth effects. A meaningful, non-zero transition rate can only be obtained if the initial and final states are treated as sharp and long-lived. We therefore use bare propagators, S^{out}, S^{in}, and

$S^{in'}$, to represent the external lines ~~in Fig. 5.2.~~ Note that decay of the initial and final states for a given transition are included in the occupation functions, $n_j(t)$. (This is discussed further below.)

To make the approximation described above, we substitute (5.33b, c, and d) into the transition amplitudes (5.25) to (5.28). The integrals are done trivially by $S_{fj}^{out}(\omega)$, and substitution into (5.8) gives the rate formula

$$R_{fi} = \sum_{n_\beta(\beta)} \sum_{n_\ell(I)} \frac{2\pi}{\hbar^2} \times \left| \langle n_\ell(I), n_\beta(\beta), f | U(\infty) H_{int}(0) | 1, \beta, I \rangle \right|^2 \delta(\varepsilon_f - \varepsilon_i + \varepsilon_\ell + \varepsilon_\beta) \qquad (5.38)$$

The energy-conserving Delta function arises from the bare propagator $S_{ji}^{in}(\omega)$. The energies of the final photon and phonon states are given by $\hbar\varepsilon_\ell$ and $\hbar\varepsilon_\beta$, respectively. The derivation of (5.38), which is shown in general in Appendix D, is based on approximating the external molecule propagators in the amplitudes with their bare counterparts, and is discussed below.

In the approximations discussed above, the amplitudes given in Fig. 5.2 are now replaced by those relevant to (5.38), as shown in Fig. 5.5. The one-photon and one-phonon amplitudes (a and c) give precisely the transition rates previously calculated in Section 2.4. The two-quanta rates, as calculated from (5.38), will be described in Sections 5.3 - 5.5.

5.2.4 Bound state resonances in the two-quanta transition rates

It was noted above that the two phonon/photon transition rate calculation encounters divergences if the intermediate state molecular propagators are not dressed, so that the intermediate state energies are sharp. As a result, we derived approximate expressions for the transition amplitudes shown diagramattically in Fig. 5.5, which are made finite by the inclusion of intermediate state linewidths, as is physically reasonable. The resulting transition rate expression, given in (5.38), is equivalent to the usual "T-matrix" approach used in scattering theory, described, for example, by Messiah.[98] By symbolically defining the T-matrix

$$T = H_{int} + H_{int}\, G\, H_{int}, \tag{5.39}$$

the calculation of the transition probability per unit time is based on the formula

$$R_{fi} = \frac{2\pi}{\hbar} |\langle f|T|i\rangle|^2 \delta(E_f - E_i). \tag{5.40}$$

The first term in T in (5.39) will contribute to the first order transition rates involving one phonon/photon processes, while the second term gives higher order processes. By approximating $G = G^r$ in (5.39), the $H_{int}G^rH_{int}$ term describes the two-vertex transitions which we include by expanding U(=) in (5.38). Note that this procedure does not include the effect of decay of the initial or final states in the transition rates R_{fi} in (5.40). Similar results are derived in differ-

(a) $\frac{1}{i\hbar} < k, \beta, f \mid U(\infty)\, H(0) \mid i, \beta, I >$

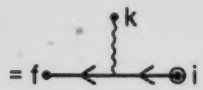

(b) $\frac{1}{i\hbar} < k, k', \beta, f \mid U(\infty)\, H(0) \mid i, \beta, I >$

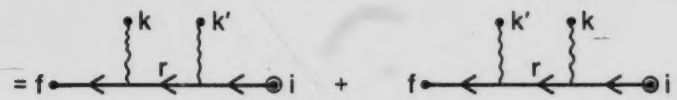

(c) $\frac{1}{i\hbar} < I, p, f \mid U(\infty)\, H(0) \mid i, \beta, I >$

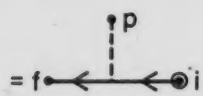

(d) $\frac{1}{i\hbar} < I, pp', f \mid U(\infty)\, H(0) \mid i, \beta, I >$

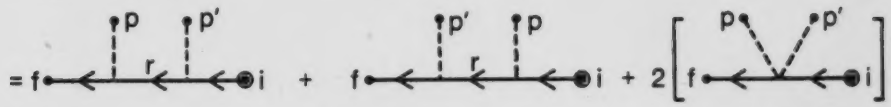

(e) $\frac{1}{i\hbar} < k, p, f \mid U(\infty)\, H(0) \mid i, \beta, I >$

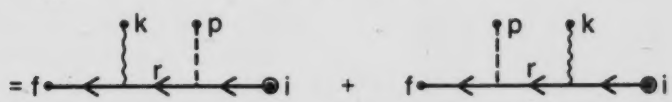

Fig.5.5, Approximate transition amplitudes. The intermediate-state propagators G^r are indicated by "r" above. Initial and final state lines are bare.

ent ways by Dirac[102] and Heitler[103], in which the intermediate "molecule" states energies are represented by a line shape function when treating the resonance conditions.

It must be emphasized, however, that the transition rates R_{fi} that enter the master equation are not physically observable quanti-

ties in themselves. Even if it were proposed to prepare an adsorbed molecule in a given state i and watch it decay into some other state f, one could only observe the decay of the combined quantity "$R_{fi}n_i$" as a function of time. That is, one measures the combined effect of single particle rate, R_{fi} in (5.40), and of the decay of the initial and finite states. When the system under consideration has only two states, or two sets of states, i and f, it is possible to calculate the combined quantity above which is physically observable and finite. This has been done by Gortel et al.[99] for thermal desorption from a single, discrete, bound state. The transition rate they calculate includes both the divergent two-vertex terms (c.f. Fig.5.5(d) but with G^r replaced by the bare propagator S), and also equally divergent initial and final state self-energy corrections. These divergences, which arise exclusively from treating the intermediate states as discrete, cancel, to yield a finite overall transition rate. This cancelation is a manifestation of the unitarity of the S-matrix, $U^\dagger(\infty)U(\infty)$.

However, in our case, we describe the system dynamics in terms of two quantities, R_{fi} and n_i, in constructing the master equation for an adsorption system with many bound states. As a result of cutting the coherence of the transition process in this way, R_{fi} can contain divergences if the intermediate states are discrete. The fact that the calculated intermediate state linewidths are larger than the inverse of the transient times of the system ensures that it is physically meaningful to broaden these states to give finite transition rates, R_{fi}. Note that this procedure includes the full linewidth (5.59) of the intermediate states in R_{fi}, while the decay of the initial and final states is included in $n_i(t)$ and $n_f(t)$. Only dephasing

effects on the initial and final states are not included in the formulation presented here. This is not anticipated to cause any qualitative errors in the desorption rate calculation. (Although these dephasing effects must be included in the coherent two-photon transition rates, these rates are shown to be negligible for typical photodesorption systems.) The unitary of the S-matrix that is, the conservation of admolecule probability, is preserved in our calculation, due to the relation

$$R_{ii} = -\sum_{f \neq i} R_{fi}, \tag{5.41}$$

which says that the decay rate of the i^{th} molecular state is equal to the sum of the transition rates into all other states. The physical meaning of the transition rates (5.38) based on the amplitudes shown in Fig. 5.5 has thus been established, in a master equation formalism.

The transition rates derived in this way are described in the next sections.

5.3 Coherent Two-Phonon Transitions

Molecular transition rates mediated by the coherent absorption and/or emission of two (real) phonons are now calculated. These processes are particularly important for adsorption systems where the lower energy states (ε_i) in the surface potential are separated by more than the maximum phonon energy. Furthermore, we will restrict our calculation to transitions between bound states only, and ignore two-phonon contributions to bound state-to-continuum transitions.

The two-phonon transition rate is given, according to (5.38), as

$$D_{fi} = \frac{1}{2} \sum_{pp'} 2\pi \left| (i\mathcal{H})^{n-1} \langle I, pp', f | U(\infty) H_{int}(0) | i, \beta, I \rangle \right|^2 \delta(\varepsilon_f - \varepsilon_i + \omega + \omega'). \quad (5.42)$$

The sum over thermal phonon final states p and p' runs over both particle and hole states; the factor of 1/2 prevents double counting due to the indistinguishability of permuted phonon states such as $|p,p'\rangle$ and $|p',p\rangle$. (We define $\omega = \omega_p$ and $\omega' = \omega_{p'}$ in (5.42).) According to Fig. 5.5, the transition amplitude is given by

$$(i\mathcal{H})^{n+1} \langle I, p, p', f | U(\infty) H_{int}(0) | i, \beta, I \rangle$$

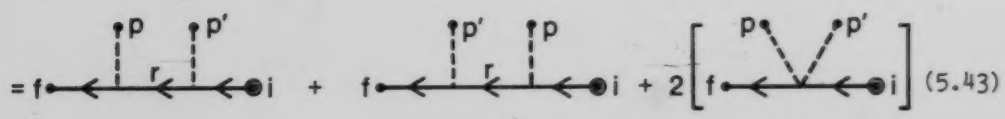

(5.43)

The terms above are calculated by using the explicit forms of the molecule propagators, $S^{in'}$, S^{out}, and G^r in (5.33) and (5.37) to simplify the amplitudes above to

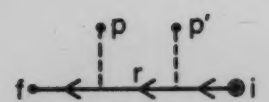

$$= \sum_j V_{fjp} \, G^r_j(\varepsilon_f + \omega_p) \, V_{jip'} \quad (5.44)$$

and

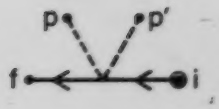

$= V_{fipp'}$, respectively. (5.45)

The bare one and two phonon vertices, V_{fip} and $V_{fipp'}$ respectively, correspond to first and second derivative terms in the phonon interaction (2.29), and are given explicitly in Appendix D.

Substituting (5.43) to (5.45) into (5.42) and manipulating the summation indices using the fact that V_{fip} and $V_{fipp'}$ are pure imaginary leads to the expansion for the transition rate,

$$D_{fi} = \frac{1}{2} \sum_{pp'} \Bigg[\sum_{jj'} * \Big[V_{fjp} V_{jip'} V^*_{fj'p} V^*_{j'ip} I^{(2)}_{jj'}(\omega,\omega) + V_{fjp} V_{jip'} V^*_{fj'p'} V^*_{j'ip} I^{(2)}_{jj'}(\omega,\omega') \Big] + 4 \sum_{j} V_{fjp} V_{jip'} V^*_{fipp'} I^{(1)}_{j}(\omega) + 4 V_{fipp'} V^*_{fipp'} I^{(0)} \Bigg] . \quad (5.46)$$

The functions $I^{(n)}$, containing the energy-conserving Delta function in (5.42) and the intermediate-state propagagors G^r, are given by

$$I^{(0)} = 2\pi\delta(\varepsilon_f - \varepsilon_i + \omega + \omega') \quad (5.47)$$

$$I^{(1)}_j(\omega) = [G^r_j(\varepsilon_f + \omega) + \text{c.c.}] I^{(0)} \quad (5.48)$$

$$I_{jj'}{}^{(2)}(\omega,\omega') = [G^r_j(\varepsilon_f + \omega) G^r_{j'}(\varepsilon_f + \omega')^* + \text{c.c.}] I^{(0)} . \quad (5.49)$$

The first two terms in D_{fi} above are due to the product of the two-vertex terms in (5.44) in (5.42), leading to the double sum over intermediate states j and j' in (5.46). The third term with the single j-sum arises from the product of a two-vertex amplitude with a single-vertex one, such as (5.44) x (5.45)*. The product of the single-vertex amplitudes, (5.45) in (5.42), gives the final term in the transition rate. This last term is equivalent to the Fermi Golden Rule transition rate formula, with the second derivative phonon interaction term in (2.29) providing the perturbation. The two-vertex terms, on the other hand, use the first derivative phonon interaction twice. It is found that all four terms in (5.46), including the cross-term, play an important role in the rate D_{fi}.

The physical meaning of the energy-functions, $I^{(n)}$, is clear. Overall energy conservation for the transition, i → f, is ensured by the delta function in $I^{(0)}$ in (5.47-9). The bracketed terms in $I^{(1)}$ and $I^{(2)}$ have energy dependences of pseudo-Lorentzian form that are resonant at $\varepsilon_f - \varepsilon_j + \omega = 0$ or $\varepsilon_f - \varepsilon_{j'} + \omega' = 0$. At these resonances, the intermediate molecule state (ε_j) is degenerate with a state composed of the final molecule state (ε_f) and a phonon excitation (ω).

The evaluation of the transition rate D_{fi} involves expanding the vertex functions V_{fip} and $V_{fipp'}$, as given in Appendix D in terms of the first and second-derivative matrix elements of the surface potential and including the phonon thermal occupation functions. As in equation (2.57), we treat the phonon wave vector as a continuous variable and sum trivially over phonon polarization. Explicit expressions for the surface potential matrix elements are given in Appendix B. Altogether, substitution into (5.46), converting to dimensionless vari-

ables (see (2.61-2)), and writing the double index j explicitly as (j,v), now gives the final formula for the two-phonon assisted transition rate from (j,v) to (j',v')

$$D^{j'v'}_{jv} = \omega_D A \frac{v_>!}{v_<!} a^{|v-v'|}[F_1 + F_2 + F_3] \tag{5.50}$$

where

$$A = 288\pi \frac{\sigma_0^6}{r^6} \frac{m^2}{M_S^2}, \quad a = \frac{m_2/m_1}{r\delta_v}, \tag{5.51}$$

$$F_1 = \frac{1}{8} \frac{r^2}{\sigma_0^4} [(v_> - v_<)!]^{-2} (I(v_> - v_< + 1, j', j))^2 J_1. \tag{5.52a}$$

$$F_2 = \frac{r}{\sigma_0^2} [(v_> - v_<)!]^{-1} I(v_> - v_< + 1, j', j) \sum_{j=0}^{j_{max}} \sum_{u=v_<}^{v_>} \frac{G_{j'v'iu} G_{iujv}}{(v_> - u)!(u - v_<)!} J_2, \tag{5.52b}$$

and

$$F_3 = \sum_{j,j'=0}^{j_{max}} \sum_{u,u'=v_<}^{v_>} \frac{G_{j'v'iu} G_{iujv} G_{j'v'i'u'} G_{i'u'jv}}{(v_> - u)!(u - v_<)!(v_> - u')!(u' - v_<)!} J_3. \tag{5.52c}$$

Here $v_>(v_<)$ is the greater (lesser) of v and v'. The terms F_1, F_2, and F_3 derive from the third, second, and first two terms in (5.46), respectively. To reduce the computational complexity somewhat, the sum

over intermediate states in (5.52b and c) is restricted to $v_< < u' < v_>$. This is a good approximation when $a << 1$, as is typically the case. The functions G and I above arise from the (Morse) surface potential matrix elements and are given by

$$G_{uvu'v'} = \begin{bmatrix} I(|v-v'|,i,i') \text{ if } (i,v) \neq (i',v') \\ \frac{a}{2}(2v+1)I(2,i,i) \text{ if } (i,v) = (i'v') \end{bmatrix} \tag{5.53}$$

and

$$I(\ell,i,i') = \frac{1}{\sigma_0}\left[\frac{i_>!\Gamma(2\sigma_0-i_>)}{i_<!\Gamma(2\sigma_0-i_<)}(\sigma_0-i-1/2)(\sigma_0-i'-1/2)\right]^{1/2}$$
$$*\left[2^{\ell}\frac{|i-i'|}{2\sigma_0}(2\sigma_0-i-i'-1)+2^{\ell-1}\right], \tag{5.54}$$

with $i_>(i_<)$ equal to the greater (lesser) of (i,i'). The integrals over (dimensionless) phonon frequency are

$$J_1 = \int_{-1}^{1} dx\, xn(x)[\theta(1-|y|)yn(y)]_{y=\varepsilon_j'-\varepsilon_j-x}, \tag{5.55}$$

$$J_2 = \int_{-1}^{1} dx\, \frac{\varepsilon_j'-\varepsilon_l-x}{(\varepsilon_j'-\varepsilon_l-x)^2+\sigma_{1u}^2}\, xn(x)[\theta(1-|y|)yn(y)]_{y=\varepsilon_j'-\varepsilon_j-x}, \tag{5.56}$$

$$J_3 = \int_{-1}^{1} dx \left[P_{iu,i'u'}[\varepsilon_j'-\varepsilon_l-x, \varepsilon_j'-\varepsilon_l'-x] + P_{iu,i'u'}[\varepsilon_j'-\varepsilon_l-x, \varepsilon_j-\varepsilon_l'+x]\right]$$

$$* \; xn(x)[\theta(1-|y|)yn(y)]_{y=\varepsilon_{j'}^{v'}-\varepsilon_j^v-x'} \tag{5.57}$$

where n(x) is the thermal phonon occupation function (2.60) and

$$P_{iv,i'v'}[x,y] = \frac{xy+\sigma_{iv}\sigma_{i'v'}}{(x^2+\sigma_{iv}^2)(y^2+\sigma_{i'v'}^2)} \; . \tag{5.58}$$

As in equation (2.64) for the one-phonon rates, the integration over negative x-values represents phonon emission, while the positive x-region accounts for phonon absorption in the integrals in (5.56).

The line widths σ_{iv} appearing in (5.58) and (5.56) are related to the self-energy correction $\Sigma_{iv}(\omega)$ that enters the intermediate molecular state propagator, G^r in (5.37). In units of the Debye frequency of the solid, σ_{iv} is given by

$$\sigma_{iv} = -\frac{1}{\omega_D} \mathrm{Re}\,[\Sigma_{iv}(\omega)]_{\omega=\varepsilon_i^v} \; . \tag{5.59a}$$

Here we have assumed that the ω-dependence of the self-energy function $\Sigma_{iv}(\omega)$ is slow, and made the replacement $\omega = \varepsilon_i^v$ in (5.56) and (5.58). Using this approximation, the line width σ_{iv} is then independent of frequency.

To evaluate the line width, the self-energy insertion $\Sigma_{iv}(\omega)$ is calculated according to the diagram-expansion given in Fig. 5.3, repeated below

$\Sigma_{iv}(\omega) =$ 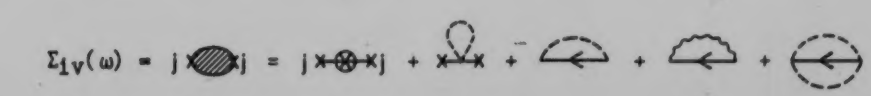 $+ \ldots$ (5.60)

where the index j on the right hand side stands for the pair (i,v). The first two terms above contain only a single vertex and give pure-imaginary contributions to Σ_{iv}; they do not contribute to the line width in (5.59a). Using the diagram rules in Appendix D, the last three terms in (5.60) are evaluated - this involves a single frequency integral in the third and fourth terms and a double integral in the fifth. The result is

$$\sigma_{iv} = \frac{1}{2\omega_D}\left[\sum_{i'=0}^{j_{max}}\sum_{v'=0}^{v_{max}}\left[P^{\gamma'}_{\gamma}\gamma + D^{\gamma'}_{\gamma}\gamma(1)\right] + \sum_{v'=0}^{v_{max}+1}\left[L^{v'v}+P^{\gamma'v}_{ci} + Q^{\gamma'v}_{ci}\right]\right] \tag{5.59b}$$

The line width given above is the sum of the transition rates out of the state (i,v) into other bound or continuum states. The laser-induced one-photon transition rate $L^{v'v}$ arises from the fourth term in (5.60). The third term contributes the one-phonon transitions $P^{\gamma'}_{\gamma}\gamma$ and $P^{\gamma'v}_{ci}$. The last term in (5.60) gives the two-phonon transition rate term $D^{\gamma'}_{\gamma}\gamma(1)$. This rate is precisely that part of the total two-phonon rate $D^{\gamma'}_{\gamma}\gamma$ which arises purely from the second derivative term in the phonon interaction; $D^{\gamma'}_{\gamma}\gamma(1)$ corresponds to the F_1-term in (5.50). The tunneling rate $Q^{\gamma'v}_{ci}$ is calculated from a self-energy diagram involving two residual Hamiltonian (H_{res}) vertices. Strictly speaking, this term does not belong in the irreducible self-energy correction, which actually contains off diagonal terms. However, after ignoring the off-diagonal part of $\Sigma_{iv}(\omega)$ in deriving (5.37), the inclusion of $Q^{\gamma'v}_{ci}$ in (5.59b) accounts for some of these neglected terms. (The contribution from $Q^{\gamma'v}_{ci}$ and $P^{\gamma'v}_{ci}$ to the line width σ_{iv} is in fact very small.)

Also included in the sums in (5.59b) are line width terms labelled $P^{\gamma\gamma}$ and $D^{\gamma\gamma}(1)$ arising from terms in (5.60) for which $(i',v') = (i,v)$. These diagonal terms, which do not appear as rates in the master equation, represent transitions in which the molecule remains in its initial state while the phonon system undergoes a change. Although these processes do not cause the molecular wave function to decay, they do interupt its phase coherence. This dephasing effect makes a contribution to the line width of the molecular states, in analogy with T_2'-lifetime included in a phenomenological approach (Bloch equations) to two level systems.[59] The two-phonon term, $D^{\gamma\gamma}(1)$ represents elastic scattering of a phonon off of the adsorbed molecule, which it sees as a point defect. Since the eigenstates of the molecule do not have well defined momenta, phonons can scatter elastically, changing wavevector but not energy. The line width term $P^{\gamma\gamma}$ represents absorption of a soft phonon ($\omega = 0$) by the adsorbed molecule. These two line width contributions are calculated using (5.60), and are identical in form to their off-diagonal counterparts, $P^{\gamma',\gamma}$ and $D^{\gamma',\gamma}$, given in (2.58) and (5.50) respectively. Explicit evaluation gives

$$D^{\gamma\gamma}(1) = \omega_D\, 36\pi \frac{m^2}{m_S^2} \frac{\sigma_0^4}{r^4} \left(\frac{\bar{\sigma}_0 - i - 1/2}{\sigma_0}\right)^2 \left[1 + 7a(2v+1) + \frac{49}{4}(2v+1)^2a^2\right] * \int_{-1}^{1} dx\, x^2 n(x)[1+n(x)] \tag{5.61}$$

and

$$P^{\gamma\gamma}_{11} = \omega_D \, 54\pi \, \frac{m}{M_s} \, \frac{T}{T_D} \, \frac{\sigma_o^2}{r^3} \, (\sigma_o - 1 - \frac{1}{2})^2 a^2 (2v+1)^2 \qquad (5.62)$$

where a is given in (5.51), and T_D is the Debye temperature. These dephasing processes can sometimes dominate in the line width σ_{ov} for the lowest surface bound state. However, for excited surface states, $j > 0$, σ_{jv} is usually dominated at low temperatures by phonon-emitting transitions given by $P^{\gamma\gamma}_{j'j}$ with $j'<j$. The laser-assisted rates, $L^{v'v}$, make negligible contributions to σ_{jv} at realistic intensities.

Computation of the transition rates $D^{\gamma',\gamma}_{j',j}$ in (5.50) is accomplished numerically. The coherent two-phonon transition processes appear in the master equation in parallel with the one-phonon transitions given by $P^{\gamma',\gamma}_{j',j}$, as well as contributing new transitions that are not otherwise possible. While the effect of two-phonon transitions in the master equation is illucidated in Section 5.6, a general discussion of the rates $D^{\gamma',\gamma}_{j',j}$ is now in order.

The fastest phonon-assisted transition rates entering the master equation are those that change only the surface bond state j while leaving the vibrational level v unaltered. For a deep surface potential, the lower states may be separated by greater than one phonon energy, that is $2\omega_D > \varepsilon^{\gamma}_{j+1} - \varepsilon^{\gamma}_{j} > \omega_D$. For these states $P^{\gamma\gamma}_{j\pm1,j}$ is zero, but $D^{\gamma\gamma}_{j\pm1,j}$ can still induce step-wise excitation in the surface potential. The two-phonon rate receives roughly comparable contributions from each of the three terms in (5.50) for these transitions. At slightly higher states in the surface potential, where one-phonon processes are also possible ($\omega_D \gtrsim \varepsilon^{\gamma+1}_{j} - \varepsilon^{\gamma}_{j}$), the two-phonon rate works in parallel, making contributions that are typically of the size

$D^{vv}_{j+1j} \approx 0.2P^{vv}_{j+1j}$. However, for j-states in the upper part of the surface potential, we find that two-phonon processes can dominate over one-phonon transitions, that is $D^{vv}_{j'j} > P^{vv}_{j'j}$. For these higher, more densely packed states, the energy level widths are calculated to be larger than the small energy level spacings; $\sigma_{jv} > \epsilon^{v}_{j+1} - \epsilon^{v}_{j}$. It is concluded that the perturbation theory used here for the phonon interaction is valid for transitions between the lower states in the surface well, but breaks down in the upper part. How this source of inaccuracy affects the desorption rates is discussed below.

The effect of two-phonon transitions between states in the upper part of the surface well can be determined by artificially cutting off the rate $D^{vv}_{j'j}$ for $j_{max} > j', j > j^*$. In practice, we determine by trial and error the cut-off level j^*, up to which it is necessary to include two-phonon transitions in the master equation. The cut-off level j^* is typically midway up the surface potential for $CH_3F/NaCl$ in (2.91), but depends on the specific adsorption system under consideration.

Vibrational state transitions can also be mediated by phonon-assisted processes. For example, the transition $(j,v) = (0,1) \rightarrow (j',0)$ via $P^{01}_{j'0}$ and $D^{01}_{j'0}$ de-excites the vibrational mode, while lifting the molecule to an excited state j' in the surface potential. For these transitions, it is often found that the two-phonon rate is faster than the one-phonon process. In addition, two-phonon emission allows for transition to a lower j' state than possible in the one-phonon case. The more favourable wavefunction overlap between $j = 0$ and this lower j' state makes $D^{01}_{j'0}$ very efficient. Large line widths for excited j-states in the mid-well region make many intermediate states accessible in the sums in (5.52b) and (5.52c). These effects combine to give

two-phonon contributions to vibrational damping that can be considerably larger than the one-phonon rates $P^{01}_{J'0}$! In the master equation, this leads to less efficient photo-excitation of higher vibrational levels, but increased excitation of j states. Depending on the adsorption system, the desorption rates can either increase or decrease, due to these two-phonon transitions. As a consequence, the model results presented in Section 5.6 must be restricted to a study of qualitative features of the photodesorption kinetics. A non-perturbative treatment of the phonon-assisted interactions discussed above is clearly essential if quantitative predictions are desired. To this end, time-resolved experiments to determine the vibrational lifetime would certainly be helpful in checking the accuracy of the calculated transition rates.[104]

5.4 Coherent Two-Photon Transitions

Molecular vibrational transitions induced by the coherent absorption and/or emission of two photons are now considered. These processes allow direct vibrational transitions $v \to v' = v \pm 2$ with a rate proportional to laser intensity squared.[105] Two-photon transitions parallel incoherent, stepwise, single-photon transition sequences such as $v \to v+1 \to v+2$ in the excitation of higher vibrational levels. In this section, we make an order-of-magnitude estimate of the size of the coherent two-photon transition rates, and show that they are usually much less efficient than the one-photon rate $L^{v'v}$ in stimulating photodesorption.

The two-photon transition rate, as given by (5.38), is

$$C_{fi} = \frac{1}{2} \sum_{k_1 k_2} \frac{2\pi}{\hbar^2} \left| \langle k_1 k_2, \beta, f | U(\infty) H_{int}(0) | i, \beta, I \rangle \right|^2 \delta(\varepsilon_f - \varepsilon_i + \Omega_1 + \Omega_2) \quad , \tag{5.63}$$

where Fig.5.5b gives

$$(i\hbar)^{-1} \langle k_1 k_2, \beta, f | U(\infty) H_{int}(0) | i, \beta, I \rangle$$

$$= \sum_j \left[V_{fjk_1} G^0_j(\varepsilon_f + \Omega_1) V_{jik_2} + V_{fjk_2} G^0_j(\varepsilon_f + \Omega_2) V_{jik_1} \right], \tag{5.64}$$

with $\Omega_1 = \Omega_{k_1}$ and $\Omega_2 = \Omega_{k_2}$. Combining (5.63) and (5.64) gives

$$C_{fi} = \frac{1}{2} \sum_{k_1 k_2} \sum_{jj'} [V_{fjk_1} V_{jik_2} V^*_{fj'k_1} V^*_{j'ik_2} I^{(2)}_{jj'}(\Omega_1, \Omega_1) + V_{fjk_1} V_{jik_2} V^*_{fj'k_2} V^*_{j'ik_1} I^{(2)}_{jj'}(\Omega_1, \Omega_2)] \tag{5.65}$$

where $I^{(2)}$ is defined in (5.49). Note that two-photon terms in the interaction Hamiltonian are not included here. Since the infrared radiation wavelength is many orders larger than atomic dimensions, the dipole approximation represented by the one-photon vertex is anticipated to be sufficient.

To evaluate the rate term C_{fi} we write V_{fik} in terms of the dipole matrix elements of the harmonic vibrational potential as given in (B.5), and treat the photon wavevector k as a continuouous variable as

in deriving (2.49), to get

$$C_{\gamma\gamma}^{2,v} = C_{\gamma_1,v+2}$$

$$= C_0\,(v+2)(v+1)\int_0^\infty d\Omega_1 d\Omega_2\,\frac{g(\Omega_1)g(\Omega_2)}{\Omega_1^2\Omega_2^2}\,\delta(2\Omega-\Omega_1-\Omega_2)$$

$$*[P_{iv+1}[\Omega-\Omega_1,\Omega-\Omega_1] + P_{iv+1}[\Omega-\Omega_1,\Omega-\Omega_2]] \qquad (5.66)$$

where

$$P_{iv}[x,y] = \frac{xy+\omega_D^2\sigma_{iv}^2}{(x^2+\omega_D^2\sigma_{iv}^2)(y^2+\omega_D^2\sigma_{iv}^2)} \qquad (5.67)$$

and $C_0 = \frac{\pi}{2}(\Omega^2Q^2F(\theta)^2/\epsilon_0^2\hbar^2c^2\mu^2)I^2$ for p-polarized radiation. (All other transition rates $C_{\gamma}^{\gamma'\gamma}$ are zero.) Note that only the most significant intermediate states are included in (5.66). Here, $g(\Omega)$ is the laser line shape given in (2.52), with width, $\Gamma_\ell < 1\ cm^{-1}$, much less than the molecular line widths. In this limit, the integral in (5.66) is inadequate to describe two-photon absorption, because our T-matrix formalism has neglected line broadening of the initial and final molecular states. This shortcoming is remedied here by broadening the energy conserving delta function in (5.66) into a Lorentzian with width Γ. A more rigorous formulation may be found in ref. 105. For $\Omega_\ell = \Omega$ in the on-resonant case, and taking all molecular line widths to be of the order of Γ leads to

$$C_I^{\gamma+2,\gamma} = 4\left(\frac{Q^2}{\varepsilon_0 c\hbar}\right)^2 \frac{F(\theta)^2(\nu+2)(\nu+1)}{\mu^2\Omega^2\Gamma^3} I^2 \qquad (5.68)$$

in the limit $\Gamma >> \Gamma_\ell$, with $F(\theta)$ given by (2.50).

At the upper limit of typical laser intensities used in resonant photodesorption experiments, $I = 1 MW/cm^2$, and for the $CH_3F/NaCl$ adsorption system parmeters used previously in Section 2.6, (5.68) gives

$$C_{ii}^{20} = 7\cdot10^3\ s^{-1} \text{ compared to } L^{10} = 6\cdot10^7\ s^{-1}. \qquad (5.69)$$

To compare the efficiency of the two-photon transitions with one-photon processes, an incoherent sequence of one-photon transitions must first be modeled. To do so, we note that one-photon absorption processes occupy the first excited vibrational level with population

$$n_i^1 = \frac{L^{10}}{\gamma} n_i^0,$$

as shown in equation (2.90) in Section 2.5 for intensities below saturation. Here γ is the vibrational damping rate due to transitions P_i, I^{01} and $D_i {}^0_i{}^1$. Absorption of a second photon with transition rate L^{21} then gives the rate of population of the $v = 2$ state as (take $i = 0$ for simplicity)

$$L^{21} n^1 = \frac{L^{21} L^{10}}{\gamma} n^0.$$

This is to be compared with the coherent two-photon rate,

C_{00}^{20} n°.

Using (5.68) and (2.49) gives

$$\frac{C_{00}^{20}}{L^{21}L^{10}\gamma^{-1}} = \frac{\gamma}{\Gamma} \approx 10^{-3}. \tag{5.70}$$

For the CH_3F/NaCl system, the coherent two-photon process is insignificant in exciting the v = 2 level compared to incoherent sequences of one-photon transitions.

It is therefore concluded that coherent two-photon transitions are of negligible effect on the adsorbate dynamics, provided the vibrational damping constant γ is much smaller than the homogeneous vibrational width Γ. This is just the rapid dephasing limit (where Γ = dephasing rate), for which Fain and Lin predict that the one-photon rates should dominate.[36,37] We therefore do not include coherent two-photon transition rates $C_{11}^{\nu'\nu}$ in the master equation.

It must be noted that the rapid dephasing limit ($\gamma \ll \Gamma$) may not be valid for all adsorption systems. For example, it is believed, for the CO/Cu(100) system, that $\gamma \approx \Gamma$.[76] In this case, coherent multiphoton absorption processes are just as effective as incoherent one-photon sequences of transitions in initiating photodesorption. In addition, the vibrational line width Γ becomes dependent on the vibrational levels involved, so modification of the one-photon transition rate formula (2.49) is then necessary too.

Finally, we observe that for neither case discussed above are "high field" effects such as power broadening or Rabi sidebands to be

expected.[39] The large line width of adsorbed molecules makes these features undetectable at all typical laser intensities. The "high field" regime sets in for $L^{10} \gtrsim \Gamma$, corresponding to laser intensities of the order of $I \sim 10^{10} W/cm^2$!

5.5 Coherent One-Photon plus One-Phonon Transitions

In this section, coherent absorption and emission processes involving one photon and one phonon are considered. It will be shown in Section 6 that these transitions can lead to an asymmetric photodesorption line shape. This asymmetry arises from the vibrational excitation process involving coherent absorption of a photon and phonon that works in a near parallel with the single-photon transition, $L^{v'v}$ in the master equation. We now calculate these rates for bound state-bound state transitions, given in (5.38) as

$$B_{fi} = \sum_{kp} \frac{2\pi}{\hbar^2} |\langle k,p,f|U(\infty)H_{int}(0)|i,\beta,I\rangle|^2 \delta(\varepsilon_f - \varepsilon_i + \Omega_k + \omega_p) \quad . \tag{5.71}$$

The transition amplitudes, as given in Fig. 5.5(e) and using (5.33), (5.37) and (D.5), are

$$(i\hbar)^{-1}\langle k,p,f|U(\infty)H_{int}(0)|i,\beta,I\rangle$$

$$= \sum_j [V_{fjk}\, G_j^+(\varepsilon_f + \Omega_k) V_{jip} + V_{fjp}\, G_j^+(\varepsilon_f + \omega_p) V_{jik}\,]. \tag{5.72}$$

Each term in the transition amplitude above contains both a one-photon

vertex V_{jik} describing dipole coupling to the laser radiation, and a one-phonon vertex resulting from the first derivative term in the phonon coupling (2.29).

To compute the transition rate given in (5.71), we employ (5.72), writing the vertices explictly as given in Appendix D and treating the phonon and photon spectra in a continuuum approximation as before. The integral over phonon energies is done trivially by using the Delta function in (5.71), while the integral over photon frequencies disappears in the limit of small laser line widths. (Since the laser line width is an order of magnitude smaller than the molecular level widths contained in G^r, the photon frequency distribution can be taken as sharp. This means taking $g(\Omega) = \delta(\Omega-\Omega_\ell)$ in (2.52).

These operations give the one-photon plus one-phonon transition rate, which, after some straightforward simplifications, becomes

$$B^{j'}_{j} = B_0 \sum_{\delta=\pm\delta_\ell} [\theta(1-|x|)xn(x)]_{x=\varepsilon^{j'}_{j'}-\varepsilon^{j}_{j}+\delta}$$

$$* \sum_{u,u'=0}^{v_{max}+1} \Big[H^{(1)}_{jj'uu'} P_{j'uj'u'}[(v'-u)\delta_v+\delta,(v'-u')\delta_v+\delta]$$

$$+ H^{(2)}_{jjuu'} P_{juju'}[(v-u)\delta_v-\delta,(v-u')\delta_v-\delta]$$

$$+ H^{(3)}_{jj'uu'} P_{j'uju'}[(v'-u)\delta_v+\delta,(v-u')\delta_v-\delta]\Big] , \qquad (5.73)$$

where $B_0 = 6\pi\sigma_0 r^{-3} m M_S^{-1} \delta_v \delta_\ell^{-2} F(\theta) Q^2(\varepsilon_0 \mu c \hbar \omega_D^2)^{-1} I$, and we define $\delta_\ell = \Omega_\ell/\omega_D$, $\delta_v = \Omega_v/\omega_D$, and $F(\theta)$ is given in (2.50). The Lorenzian-like

resonance functions $P_{juj'u'}(x,y)$ are defined in (5.58). The functions $H^{(n)}_{juj'u'}$ contain two single-phonon and two single-photon matrix elements each - one from each of the two amplitudes multiplied in (5.71). The squared magnitudes of the first and second amplitude terms in (5.72) give $H^{(1)}$ and $H^{(2)}$ respectively, while $H^{(3)}$ contains the cross-terms. Note that the sums over intermediate surface bond states in (5.72) have been removed in (5.73) by the one-photon vertex which is diagonal with respect to the j-states. Only sums over intermediate vibrational states, u and u', remain in (5.73). These sums are further restricted by the (one-photon) dipole selection rules contained explicitly in $H^{(n)}_{juj'u'}$, which is shown in detail in Appendix E.

Some main features of the coherent one-photon plus one-phonon transition rate, $B^{\gamma'}_{\gamma}$, are now discussed. The photon interaction contributes a linear laser-intensity dependence to the rate, while the phonon coupling gives the transition rate a temperature dependence via the thermal occupation function n(x). The theta function in (5.73) restricts transitions $(j,v) \to (j',v')$ to those for which

$$-\omega_D < (\varepsilon_j^{\gamma'} - \varepsilon_j^{\gamma})\omega_D \pm \Omega_\ell < \omega_D. \tag{5.74}$$

The + or - sign above refers to photon emission or absorption, respectively. The rate $B^{\gamma'}_{\gamma}$ contributes to transitions where initial and final states are separated by the total energy of one photon Ω_ℓ and one phonon ($-\omega_D$ to ω_D). For example, the purely vibrational transition $(j,v) = (0,0) \to (0,1)$ already accessible by the one-photon rate L^{10} also receives a contribution from B^{10}_{00}. Typically, we find $B^{10} < 0.1\ L^{10}$ for $\Omega_\ell = \Omega$, so B^{10} represents only a small correction here. However,

the transition $(j,v) = (0,0) \rightarrow (1,1)$ is accessible via B^{10}_{10} if $\varepsilon^0_1 - \varepsilon^0_0 < 1$, while the one-photon rate L cannot contribute here. Coherent one-photon plus one-phonon processes thus contribute new rates to the master equation between states previously inaccessible directly, as well as providing a small correction term to the one-photon-assisted vibrational transitions, $v \rightarrow v \pm 1$.

The main effect of these rates $B^{\gamma',\gamma}_{\gamma'',\gamma}$ on desorption phenomena is seen in the line shape of the photodesorption yield described in Section 6. Note that the thermal phonon occupation factor "xn(x)" in (5.73) favours spontaneous phonon emission over thermal phonon absorption at low temperatures. This favours detuning of the laser frequency to the high side of the molecular transition energy $\varepsilon^{\gamma'}_{\gamma''} - \varepsilon^{\gamma}_{\gamma}$, over detuning to the low side. As a result, the coherent one-photon plus one-phonon rates have asymmetric frequency spectra, and can affect the photodesorption line shape in a similar way.

5.6 Effect of Coherent Two-Quanta Processes on Desorption Kinetics

By incorporating the coherent two-quanta transition rates described in Sections 5.3-5.5 into the master equation, the effect of these higher order processes on the photodesorption kinetics is studied. The intensity dependence of the desorption rate is considered here, while the laser-frequency spectrum of the desorption yields is discussed in detail in Section 6.

The calculation of the desorption rate (proportional to the desorption yield) is based on the master equation (2.1), as described in Section 2. However, the lowest order transition rates calculated there

are now joined by the coherent two phonon/photon rate terms so that the molecular transition rate from state (j,v) to (j,'v') is now given by

$$R^{v'}_{j',j} = L^{v'}_{j',j} + P^{v'}_{j',j} + B^{v'}_{j',j} + C^{v'}_{j',j} + D^{v'}_{j',j}. \tag{5.75}$$

Here, L and P represent the one-photon and one-phonon transition processes considered previously in Section 2. Added to them in (5.75) are additional bound state-bound state transition rate terms, B, C, and D, calculated in Sections 5.3-5.5. The coherent absorption/emission of one photon and one phonon, given by $B^{v'}_{j',j}$ in (5.73), and the coherent two-phonon processes contained in $D^{v'}_{j',j}$ in (5.50) make important contributions to the overall transition rate, $R^{v'}_{j',j}$. On the other hand, the coherent two-photon transitions given by $C^{v'}_{j',j}$ were shown in Section 5.4 to be unimportant for the photodesorption systems considered here, and are therefore neglected.

The transitions to the continuum (gas phase) states are still described by the one-phonon and direct tunneling rates calculated in lowest order in Section 2, so that

$$R^{v'v}_{cj} = P^{v'v}_{cj} + Q^{v'v}_{cj}. \tag{2.68}$$

The master equation (2.1) with transition rates given by (5.75) and (2.68) is solved by matrix diagonalization, as described previously. The physically observable desorption kinetics is again governed by the slowest eigenvalue of the matrix, which is equal to the desorption rate per adsorbed molecule, r_d.

The photodesorption kinetics of the model CH_3F/NaCl system considered previously in Section 2.6 are now re-examined, with two-quanta transitions included. The desorption rate, which depends also on temperature, is calculated as a function of laser intensity using the adsorption system parameters given in (2.91) except as noted. These theoretical results are shown graphically in Fig. 5.6. For a temperature of T = 100 K, desorption rates r_d are determined for three different values of the surface potential well depth, V_o = 22.5, 33, and 46 kJ/mole and for a potential range, γ^{-1} = 0.37 Å. These choices of V_o span the range of experimental measurements of the isoteric heat of adsorption at varying coverages and for different adsorption sites.[69]

For V_o = 22.5 kJ/mole, the desorption rate previously predicted by the single phonon/photon theory is included as the dashed line in Fig. 5.6. A comparison with the full two-quanta graph shows that the inclusion of coherent higher order transition processes shifts the desorption rate constant to higher laser intensities. This shift is due to efficient two phonon rates which reinforce single phonon transitions within the surface well via $D^{j',j}$ and significantly increase vibrational damping due to coupling between vibrational and surface bond states by, for example, aiding transitions such as (j=0, v=1) to (j=5, v=0). Consequently, saturation occurs at higher intensities and with higher desorption rates. However, it was found in Section 5.3 that the crucial vibrational damping rates cannot be accurately determined by perturbation theory due to the strength of the phonon coupling. It is therefore not possible to precisely determine the absolute lateral positions of the desorption rate graphs in Fig. 5.6. Con-

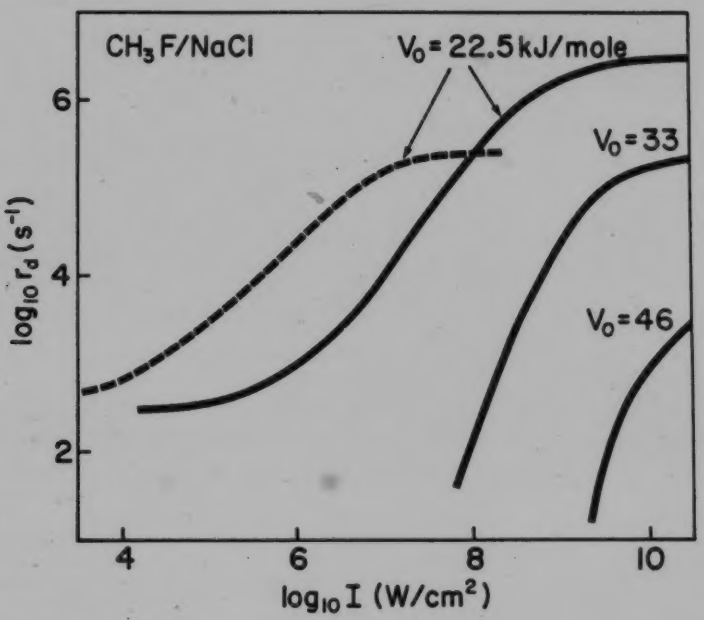

Fig.5.6. Photodesorption rate versus laser intensity for $CH_3F/NaCl$ for different adsorption energies, V_o. Dashed line is without coherent two-quanta processes. T=100K; $\Gamma=24cm^{-1}$; $\gamma^{-1}=0.37Å$.

sidering also the experimental uncertainty in the absolute infrared absorption intensities per molecule discussed in Section 2.6, a quantitative comparison with existing experimentally measured desorption yields remains unavailable.

In spite of this reservation, the dependence of the photodesorption kinetics on the heat of adsorption can be deduced qualitatively from Fig. 5.6. As V_o is increased, the desorption rate is shifted to higher intensities and becomes increasingly non-linear in intensity. Specifically, the power law dependence, $r_d \propto I^{\alpha}$, is approximately obeyed at moderate intensities and at fixed temperature.[37] The exponent α is generally less than the level of vibrational excitation v^* required to

bring the surface ground state (j=0) into degeneracy with the continuum of gas phase states. This is due to the occupation of higher j-states with $v < v^*$ under quasi-stationary conditions from which desorption is already possible. See Fig. 5.7 where energy level diagrams for the adsorbed CH_3F molecule are shown for each surface potential well depth, V_o = 22.5, 33, and 46 kJ/mole, defining the values for v^* = 2, 3, and 4, respectively. The maximum slopes of the three solid curves in Fig.5.6 give exponents α = 1.4, 2.6, and 3.7, which are somewhat less than the corresponding values of v^* = 2, 3, and 4. These differences indicate that thermal (phonon-assisted) population of excited surface bond states can, in fact, play a role in the photodesorption process.

Note also in Fig.5.6 that the desorption rate r_d at a given intensity decreases by orders of magnitude as the depth of the surface potential is increased from V_o = 22.5 to 46 kJ/mole. Rapid phonon-mediated vibrational damping makes laser-induced step-wise excitation of the higher vibrational levels in Fig.5.7 a relatively inefficient process. By narrowing the range of the surface potential well to γ^{-1} = 0.25 Å, the phonon coupling is increased and vibrational damping rates increase by an order of magnitude. The resulting desorption kinetics are shown in Fig. 5.8, with the CH_3F/NaCl system parameters otherwise unchanged from those used for Fig. 5.6. The desorption rate graphs show saturation (levelling off) at much higher intensities in Fig. 5.8 for this more strongly coupled system, due to the faster vibrational damping rates. On the other hand, at moderate intensities the curves for the two systems, γ^{-1} = 0.25 and 0.37 Å, agree to within a factor of two. This is so because the transitions such as (j=0, v=1) → (j>0,

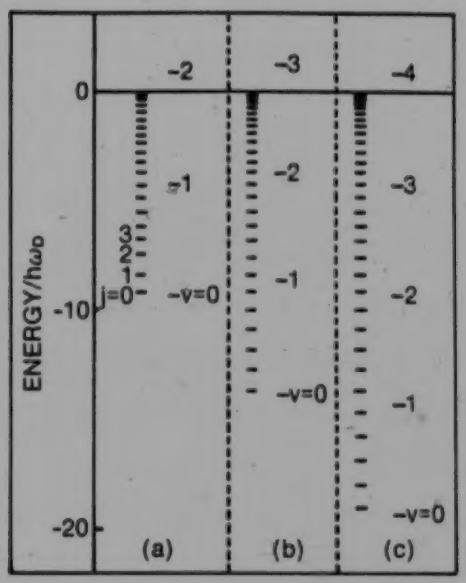

Fig.5.7. Bound state energy levels for adsorbed $CH_3F/NaCl$ for surface potential well depths (a) V_0=22.5kJ/mole, (b) V_0=33kJ/mole, and (c) V_0=46kJ/mole. j states of the surface potential and vibrational (v) levels are included.

v=0) that cause vibrational damping are at the same time responsible for populating excited surface bond states (j>0); this is a necessary step in the desorption process.

In summary, we note that, by inclusion of coherent two-phonon absorption and emission processes, model systems with larger heats of adsorption can be studied. (Only for the V_0 = 22.5 kJ/mole, γ^{-1} = 0.37Å system in Fig. 5.6 are step-wise single phonon transitions possible between all neighbouring surface bond states.) The dependence of the desorption rate on laser intensity becomes increasingly non-linear as the heat of adsorption is increased. In fact, for V_0 = 33 kJ/mole, the experimentally observed dependence,[81] $r_d \propto I^{2.8}$, is reproduced very

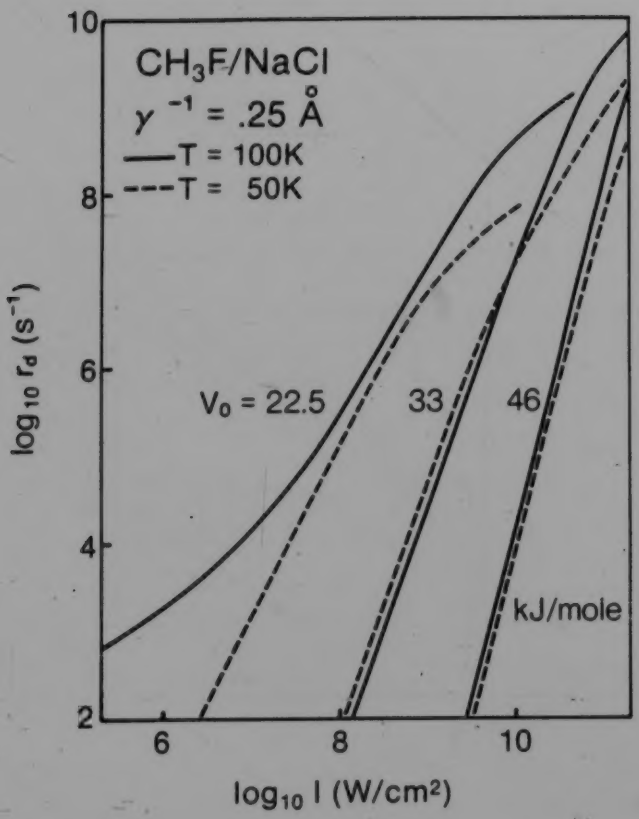

Fig.5.8. Photodesorption rate as a function of laser intensity for different adsorption energies, at T=50 and 100K. The surface potential range has been reduced to γ^{-1}=0.25Å.

well, although at considerably higher laser intensities. The coherent one-phonon plus one-photon processes, $B^{\gamma'}_{\gamma}$, do not cause any major effects in the results shown here; their importance will become apparent in the next section, where the photodesorption line shape is discussed.

6. Theory of the Photodesorption Line Shape

6.1 Introduction

Since the photodesorption mechanism we consider is initiated by resonant vibrational excitation, the resulting desorption yield must also exhibit a resonant spectral line shape. In previous chapters the dependence of the desorption kinetics on laser intensity was studied by using a laser tuned precisely to the molecular vibrational frequency, i.e. $\Omega_\ell = \Omega$. We now study the photodesorption spectrum obtained by detuning the laser frequency at a fixed intensity. The predicted desorption line shape can differ significantly from the infrared absorption spectrum associated with vibrational excitation as discussed also by Wu et al.[37] and Casassa et al.[35]. Detailed comparison of these spectra yields information on the photodesorption mechanism and on microscopic vibrational interaction processes at the surface.

The internal vibrational levels of an adsorbed molecule are, in general, broadened due to coupling to phonon and electronic excitations in the substrate[74-77,106] and due to frustrated rotational and translational modes of the adsorbate.[62] These interactions induce both elastic and inelastic transition processes corresponding to dephasing and decay, respectively, of the molecular vibrational mode.[91] The vibrational energy levels receive a homogeneous line width contribution Γ_V, due to these effects. In the theory of photodesorption from a homogeneous adsorbate, the vibrational line shape is approximated phenomenologically in the vibrational excitation rate $L^{v'v}$ (2.49) by a Lorentzian (2.52) with width $\Gamma = \Gamma_V + \Gamma_\ell$. Note that the laser line

width $\Gamma_\ell < 1\ cm^{-1}$ is typically much smaller than the vibrational level width, $\Gamma_v \approx 5\text{-}30\ cm^{-1}$, and is therefore ignored so that we can equate $\Gamma = \Gamma_v$. The desorption yield spectrum is then obtained by computing the desorption rate $r_d(\Omega_\ell)$ as a function of laser frequency.

In Section 6.2, the desorption line shape is studied, using the procedure outlined above, for a homogeneous adsorbate with a harmonic vibrational mode. The effect of coherent one-photon plus one-phonon transitions is included here.[97] Vibrational anharmonicity and V-V coupling effects are shown, in Section 6.3, to influence the desorption spectrum markedly. The theory is then extended to treat photodesorption from an inhomogeneous adsorbate, in Section 6.4. Finally, in Section 6.5, we discuss experimental results in light of these theories, and suggest how to use this comparison to help pin down the dominant photodesorption mechanism.

6.2 Homogeneous Adsorbate

In this section, as done previously, we treat a homogeneous adsorbate at low coverage. In Sections 2.6 and 5.6, it was found useful to parametrize the desorption rate by a power law

$$r_d(\Omega,\Omega_\ell,I) = C(\Omega)\, g(\Omega_\ell \to \Omega)^\alpha\, I^\alpha \tag{6.1}$$

for a given temperature and a specified range of (moderate) intensities. The desorption rate depends on the α-th power of the intensity I, determined from the graphs of r_d versus I in Figs. 2.7, 5.6, and 5.8. Since the laser intensity and the vibrational line shape function $g(\Omega_\ell \to \Omega)$ enter the master equation together in the rate $L^{v'v}$,

the desorption rate depends on the α-th power of g too. The constant of proportionality $C(\Omega)$, which is independent of Ω_ℓ and I, contains the complex microscopic dynamics of the phonon-assisted transition rates in the master equation.

For a homogeneous adsorbate in the harmonic approximation, all molecules have the single vibrational frequency, Ω. Equation (6.1) then shows that the desorption line shape is given by the α-th power of the infrared absorption spectrum, $g(\Omega_\ell - \Omega)$. For $\alpha>1$, the desorption line shape is narrower than the infrared absorption line, while for $\alpha<1$, the reverse is true. Only for the linear case, $\alpha=1$ in (6.1), are the photodesorption and infrared absorption line widths predicted to be equal. The width (FWHM) of the desorption line is given, according to (6.1) and (2.52), by $(2^{1/\alpha}-1)^{1/2}$ times the infrared absorption line width, Γ. This point has been made previously by Wu et al.[37] using a reduced master equation; it is demonstrated in detail below.

For the $CH_3F/NaCl$ adsorption system, the desorption rate was shown in Fig. 2.7 to increase nonlinearly with laser intensity. The desorption line shape for this system is obtained by varying the laser frequency Ω_ℓ entering $L^{v'v}$ in the master equation with the transition rates given by (2.67) and (2.68); it is shown in Fig.6.1. Note that the coherent two-quanta transition rates discussed in Section 5 are not included here. At an intermediate intensity of I=0.1 MW/cm^2, Fig. 6.1 shows a narrowing of the desorption line shape which is very nearly equal to the vibrational line shape function taken to the power $\alpha=1.9$, where this value of α is given by the slope of log r_d versus log I in Fig. 2.7 for T=50 K. The width is thus reduced by a factor 0.7. However, it is emphasized that the exponent α relating the in-

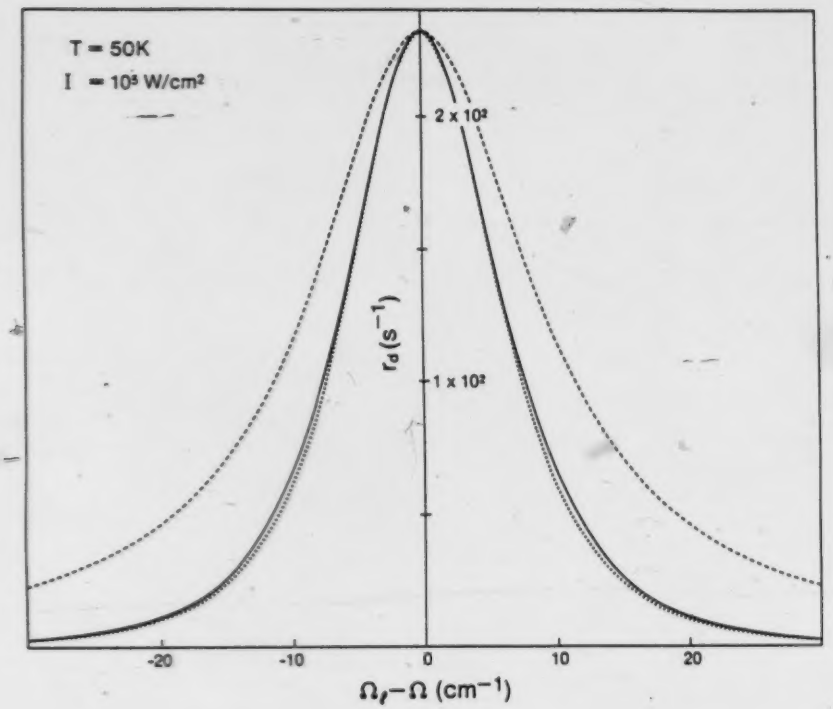

Fig.6.1 Photodesorption rate as a function of laser frequency for $CH_3F/NaCl$ at sub-saturation intensity. Dashed line is IR absorption spectrum $g(\Omega_\ell - \Omega)$ which, taken to the power $\alpha=1.9$, gives the dotted curve. System parameters are given in (2.91), except that $\gamma^{-1}=0.37$Å. Homogeneous vibrational line width is $\Gamma=20cm^{-1}$.

frared absorption and photodesorption line shapes depends on both the intensity and the temperature.

At higher intensities, the slopes of the $r_d(I)$ curves in Fig. 2.7 decrease eventually to zero as saturation sets in. For example, at T=50 K and I>10 MW/cm², $\alpha<1$ and the photodesorption line shape is therefore wider than the infrared absorption spectrum. We now include coherent two-quanta transition processes in the master equation, as outlined in Section 5.6, to calculate the photodesorption spectrum given in Fig. 6.2. At a saturation intensity of 10^3MW/cm² the desorp-

tion line width is now increased to 60 cm^{-1}, compared to the infrared absorption line width Γ=24 cm^{-1}. This broadening of the photodesorption spectrum arises because detuning the laser frequency does not diminish the desorption yield appreciably until the photon (and one-photon plus one-phonon) transition rates are reduced below the saturation level. Thus, the tails of these transition rates at large detunings affect the desorption line shape markedly at saturation.

The asymmetry and slight blue-shift of the photodesorption linshape in Fig. 6.2 are caused by coherent one-photon plus one-phonon transitions which favour spontaneous phonon emission ($\Omega_\ell - \Omega > 0$) at low temperatures, as discussed in Section 5.5. Since the asymmetry of these transition rates, $B_{j'j}^{v'v}$, occurs on the frequency scale with which the phonon thermal occupation function varies, i.e., $\Delta\nu = k_BT/h$ = 45 cm^{-1} at T = 65 K, asymmetric desorption yields may be expected when the desorption line width is of the order of the temperature T. At saturation, this condition can be fulfilled even while the infrared absorption width is smaller than k_BT/h. It is shown in the next section that vibrational anharmonicity can cause a broad desorption line shape at low intensities as well.

In addition, the tails of the infrared absorption spectrum itself become asymmetric at large detunings because the frequency dependence of the vibrational line width and line shift must then be taken into account. This second effect, although not taken into account in Fig. 6.2, is anticipated to contribute to the asymmetry of the desorption line shape in a manner similar to that of the one-photon plus one-phonon rates considered above.

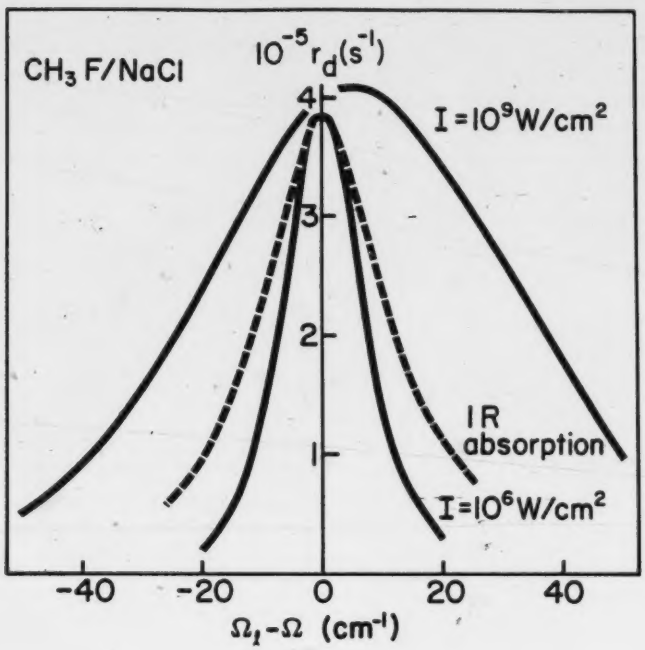

Fig.6.2 Photodesorption line shape calculated with coherent two-quanta processes included. Dashed line represents IR absorption spectrum, while solid lines are desorption rates at intensities I=1 and 10^9MW/cm^2 and T=65K for CH_3F/NaCl with the same model parameters as in Fig.6.1

In summary, it has been shown that the nonlinear relationship between r_d and I results in a photodesorption line shape which can be either narrower or broader than the vibrational spectrum. For large desorption line widths or low temperatures, an asymmetric spectrum is to be expected.

6.3 Effect of vibrational anharmonicity

The influence of vibrational anharmonicity on the photodesorption spectrum is now addressed. Up to this point, the internal vibrational mode of the molecule has been assumed to be harmonic, with a constant

energy level spacing given by $\hbar\Omega$. However, the vibrational potential of a diatomic, and even more so of a polyatomic, molecule is in reality somewhat anharmonic, leading to energy level separations approximated by

$$E_{v+1} - E_v = \hbar(\Omega - v\Delta) \tag{6.2}$$

for small v, as noted earlier in Section 4.1. The anharmonic energy defect, Δ, is of roughly the same order as the vibrational line width, Γ, of adsorbed molecules. As a result, anharmonic effects may be expected to appear in the photodesorption line shape. For an adsorption system such as CH_3F on NaCl, excitation of both the $v = 0 \rightarrow 1$ and $v = 1 \rightarrow 2$ transitions is necessary to induce desorption. A laser tuned to the lowest energy spacing, i.e., $\Omega_\ell = \Omega$, will be slightly off resonance with respect to the higher transitions. Photodesorption may be most efficient at some intermediate frequency. In this way the desorption kinetics may serve as a probe of higher vibrational energy levels.

Vibrational anharmonicity makes its main contribution to the desorption kinetics via its effect on the photon absorption rates $L^{v'v}$, as noted by Jedrzejek.[107] The vibrational level separations given by (6.2) enter into the line shape function in $L^{v'v}$ to give

$$g(\Omega - v_< \Delta) = \frac{1}{\pi} \frac{\Gamma/2}{(\Omega - v_< \Delta - \Omega_\ell)^2 + (\Gamma/2)^2} \tag{6.3}$$

where $v_<$ is the smaller of v and v'. By using $g(\Omega - v_< \Delta)$ instead of

$g(\Omega)$ in the vibrational excitation rate $L^{v'v}$ (2.49), Jedrzejek studied the intensity dependence of the desorption kinetics. Here, we will concentrate on the desorption line shape as predicted by solving the master equation of Section 2, including one-photon and one-phonon processes. Note that phonon-assisted vibrational transitions, $P_{i'i}^{v'\neq v}$, also depend individually on the vibrational energy levels and hence on the anharmonic defect, Δ. However, the overall effect on the desorption kinetics is not expected to be dramatic, and is therefore neglected here.

The desorption kinetics of the $CH_3F/NaCl$ system is displayed in Figs.6.3 to 6.5. While the vibrational line width of adsorbed CH_3F is taken to be 20 cm^{-1} from infrared absorption data,[88] one obtains for the anharmonic defect Δ=16cm^{-1} from gas phase and matrix isolation measurements.[95,96] Comparing the graphs of desorption rate versus laser intensity in Figs. 6.3(a) and (b) for Δ=0 and Δ=8 cm^{-1}, respectively, corroborates Jedrzejek's observation that anharmonicity shifts desorption to higher intensities and delays the onset of saturation.[107] In Fig.6.4, the desorption spectrum is plotted for a laser intensity of I=1 MW/cm^2, for which $r_d \propto I^{1.9}$ in Fig.6.3. The desorption line is shifted to the red of the harmonic case, and is also broadened as the anharmonicity is increased. These features result from the dependence of the desorption rate on the vibrational excitation rates of both the v=0→1 and v=1→2 transitions. The product of the line shapes of these two transitions, $g(\Omega)g(\Omega-\Delta)$, is found to agree well with the desorption spectrum.

For comparison, we now examine a model adsorption system in which the anharmonic defect is larger than the vibrational line width.

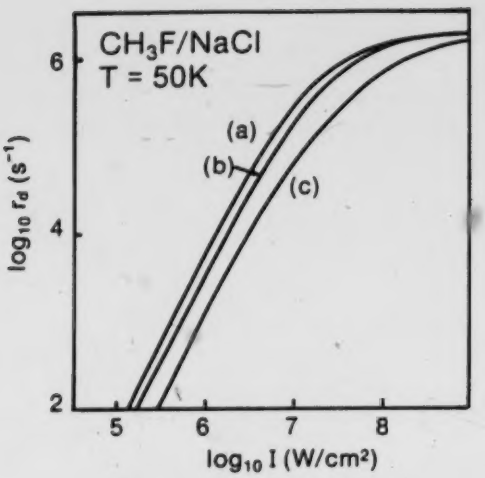

Fig.6.3 Desorption rate versus laser intensity for the $CH_3F/NaCl$ system defined in (2.91) for the following vibrational line widths (Γ) and anharmonicities (Δ):
(a) $\Gamma = 20cm^{-1}$; $\Delta = 0$;
(b) $\Gamma = 20cm^{-1}$; $\Delta = 8cm^{-1}$;
(c) $\Gamma = 10cm^{-1}$; $\Delta = 20cm^{-1}$.

Infrared absorption measurements on CO adsorbed on NaCl(100) give $\Delta=24\ cm^{-1}$ and $\Gamma=14\ cm^{-1}$.[94] However, the v=1→2 transition is not expected to contribute significantly to desorption for this system, since the adsorption well depth $V_0=2177$ K is less than the vibrational energy $\hbar\Omega=3100$ K, permitting desorption directly from the v=1 level. To study the $\Delta>\Gamma$ case, we therefore modify the $CH_3F/NaCl$ system by choosing $\Delta=20\ cm^{-1}$ and $\Gamma=10\ cm^{-1}$. The desorption spectrum for this hypothetical system is shown in Fig.6.5 to be double peaked. The desorption rate is maximized by tuning the laser near either the v=0→1 or v=1→2 transition frequency. The peaks are of roughly equal height because both transitions contribute equally to the desorption process; see Fig.6.3(c) which shows that $r_d \propto I^{1.9}$ at $I = 1MW/cm^2$. This spectrum is in sharp contrast to the infrared absorption line shape which

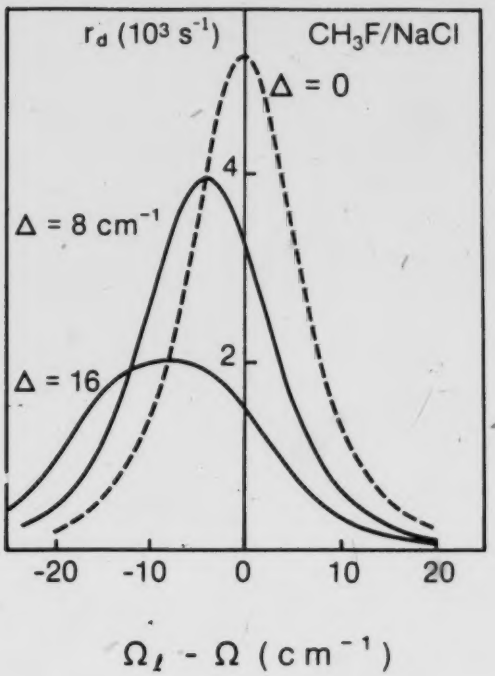

Fig.6.4. Photodesorption line shape for the CH_3F/NaCℓ model system considered in Fig.6.3. Solid lines are for vibrational anharmonicity Δ = 8 and 16cm^{-1}; harmonic case Δ = 0 is given as dashed line. Also Γ = 20cm^{-1} and laser intensity is I = 1MW/cm^2.

sees only the v=0→1 transition. The possibility of using photodesorption measurements as a spectroscopy of higher vibrational transitions depends on the efficiency of competing effects as discussed below and in Section 6.5.

Vibrational coupling between neighbouring adsorbed molecules should be included in the theory of photodesorption when anharmonic effects are significant. While this has not been done here, we expect that V-V coupling will cause a reduction on the redshift in Fig.6.4 and may

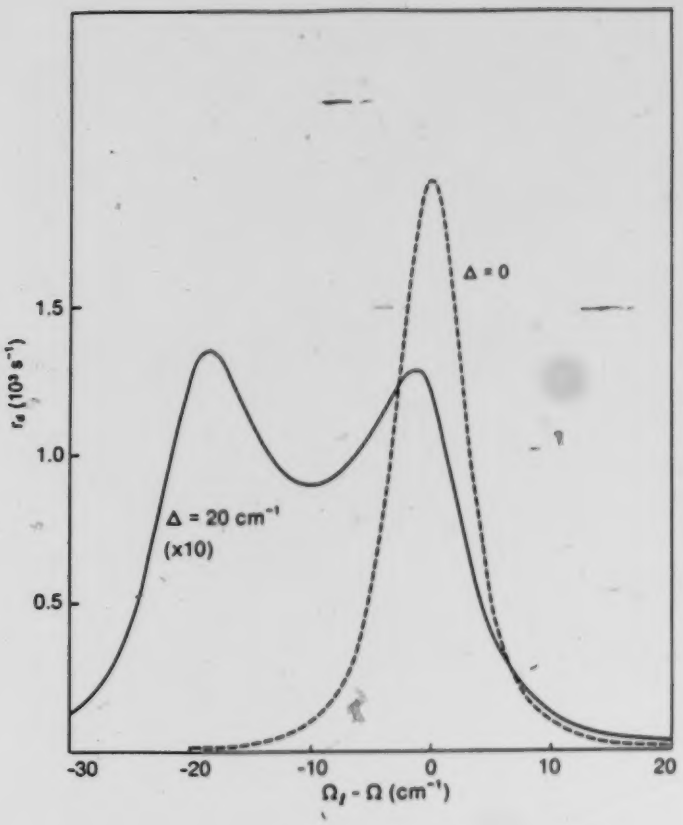

Fig.6.5. Photodesorption line shape for a modified $CH_3F/NaCl$ system. Vibrational mode parameters are $\Gamma = 10cm^{-1}$, $\Delta = 0$ (dashed line), and $\Gamma = 10cm^{-1}$, $\Delta = 20cm^{-1}$ (solid line); other parameters as in (2.91). $I = 1MW/cm^2$.

eliminate the lower frequency peak in Fig.6.5. This effect can be understood qualitatively as follows for a three-level vibrational system. At $\Omega_l=\Omega$, desorption is enhanced by V-V transfer processes, as shown in Fig.4.4, since laser excitation from $v=1\rightarrow2$ is slower than from $v=0\rightarrow1$. On the other hand, at a detuning of $-\Delta/2$, $L^{21}=2L^{10}$ and V-V coupling has no effect because condition (4.22) is satisfied. In this way, V-V coupling reduces the redshift induced by vibrational anhar-

monicity in the photodesorption spectrum. It is concluded that direct laser-excitation of the v=1→2 transition is taken over by rapid V-V transfer processes as proposed by Rain and Lin[38] and discussed in Section 4.1. Note that anharmonic effects in the desorption line shape may still be observable for systems with slow V-V transfer, or fast vibrational damping rates, such as CO/Cu(100) for which $D_{01} = Y$ as shown in Table 4.1.

6.4 Inhomogeneous adsorbate

While all previous work has concentrated on desorption from a homogeneous adsorbate, we now study the kinetics of photodesorption in the inhomogeneous case.[108] The vibrational line shape of the adsorbate is in general broadened by both (i) homogeneous decay and dephasing processes as noted previously, and (ii) by inhomogeneity in the adsorbate. Inhomogeneous broadening of the vibrational line shape is caused by heterogeneity due to different adsorption sites and due to imperfections in the underlying substrate. Also, random partial coverage leads to a statistical distribution of vibrational frequencies due to varying molecular environments. Resulting line width contibutions of the order of 10 cm^{-1} are possible, in addition to the homogeneous vibrational width.[61] While the homogeneous vibrational line shape was included in the laser-assisted transition rates, $L^{v'v}$, in the master equation, heterogeneous effects must be included seperately.

To model an inhomogeneous adsorbate, we assume that the vibrational frequencies of the adsorbed molecules are statistically distributed about some mean frequency, $\bar{\Omega}$. The experimentally measurable photodesorption rate constant, R_d^{IH}, is obtained by averaging the con-

tributions to desorption from adsorbed molecules with different vibrational frequencies Ω to get

$$R_d^{IH}(\bar{\Omega},\Omega_\ell,I) = \int_0^\infty d\Omega\, r_d(\Omega,\Omega_\ell,I) f(\Omega-\bar{\Omega}) \tag{6.4}$$

Here, we assume that the inhomogeneous spectrum of vibrational frequencies, $f(\Omega-\bar{\Omega})$, is Gaussian with line width $\Gamma_s \ll \bar{\Omega}$. Note that the homogeneous vibrational line width Γ, the vibrational anharmonicity Δ, and the photon frequency Ω_ℓ enter R_d^{IH} via the rates r_d, while the inhomogeneous line width Γ_s enters through $f(\Omega-\bar{\Omega})$.

The intensity dependence of the desorption rate R_d^{IH} is similar to that of the homogeneous case, r_d, considered in Section 2. However, the inclusion of inhomogeneous broadening of the vibrational levels makes photon absorption less efficient, causing a shift to slightly higher intensities as shown in ref.108. For large inhomogeneous broadening, the laser light resonantly excites only a fraction of about $\Gamma/\Gamma_s < 1$ of the adsorbate. Furthermore, at high intensities, saturation occurs more slowly in the inhomogeneous case because the molecules which are out of resonance with the laser light saturate at higher intensities than those in resonance.

Of main interest here is the photodesorption line shape, as plotted in Fig.6.6 for the $CH_3F/NaCl$ system. We assume here that the observed infrared absorption line shape is predominantly inhomogeneously broadened and take $\Gamma_s = 20\ cm^{-1}$ and $\Gamma = 1\ cm^{-1}$. In this situation, $\Gamma_s \gg \Gamma$ and (6.4) reduces to

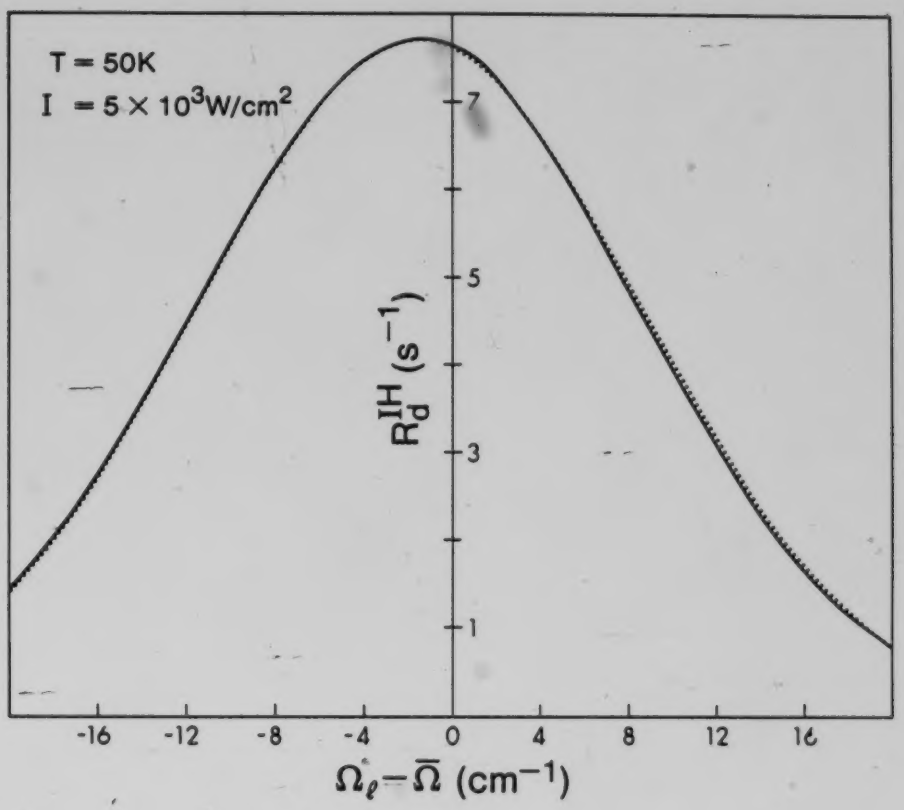

Fig.6.6. Photodesorption rate versus laser frequency for $CH_3F/NaCl$ in inhomogeneous case. The dotted line represents a Gaussian with width Γ_s and height adjusted to that of R_d^{IH}. Surface potential depth and range are V_o = 22.14kJ/mole and γ^{-1} = 0.36Å.

$$R_d^{IH}(\bar{\Omega},\Omega_\ell,I) = f(\bar{\Omega}-\Omega_\ell)\int_0^\infty d\Omega\, r_d(\Omega,\Omega_\ell,I) \quad . \tag{6.5}$$

The photodesorption line shape is therefore given by the Gaussian frequency distribution $f(\bar{\Omega}-\Omega_\ell)$, provided the integral in (6.5) varies

slowly with Ω_ℓ. The infrared absorption and photodesorption line shapes are in this case nearly the same. Fig. 6.6 shows an example of this situation.

These results are to be compared with the homogeneous case shown in Fig.6.1 where we took Γ=20 cm^{-1} and Γ_s = 0, and in contrast found a narrower desorption line shape. It is necessary to consider both these extreme line width choices until the relative contributions from heterogeneous and homogeneous sources to the infrared absorption spectrum are known.

Additional structure in the inhomogeneous photodesorption line shape is also possible.[108] By making a minor adjustment to the depth of the surface potential of the adsorption system studied in Fig.6.6, the desorption spectrum changes dramatically, as shown in Fig.6.7. Although the small increase in V_o between Figs.6.6 and 6.7 is below experimental accuracy, the theoretical appearance of a double peaked photodesorption line shape is easily explained. Desorption occurs predominantly from the j=6,v=1 state at the temperature and intensity given, via transition rates $Q_{C6}^{01}+P_{C6}^{01}$. The elastic tunneling rate, Q_{C6}^{01}, is cut off when $\varepsilon_6^1<0$, which corresponds to $\Omega<\tilde{\Omega}+12$ cm^{-1}. At lower laser frequencies Ω_ℓ, the molecules with lower vibrational frequency $\Omega=\Omega_\ell$ desorb preferentially in (6.5), via the rate P_{C6}^{01} and other transitions. However, for $\Omega_\ell>\tilde{\Omega}+12$ cm^{-1}, the laser selectively excites molecules with $\Omega=\Omega_\ell$ for which the additional tunneling transition Q_{C6}^{01} is operative. As a result, the overall desorption rate is suddenly enhanced, leading to a double peaked spectrum. The infrared absorption line shape, on the other hand, is simply given by the Gaussian vibrational frequency distribution $f(\tilde{\Omega}-\Omega_\ell)$.

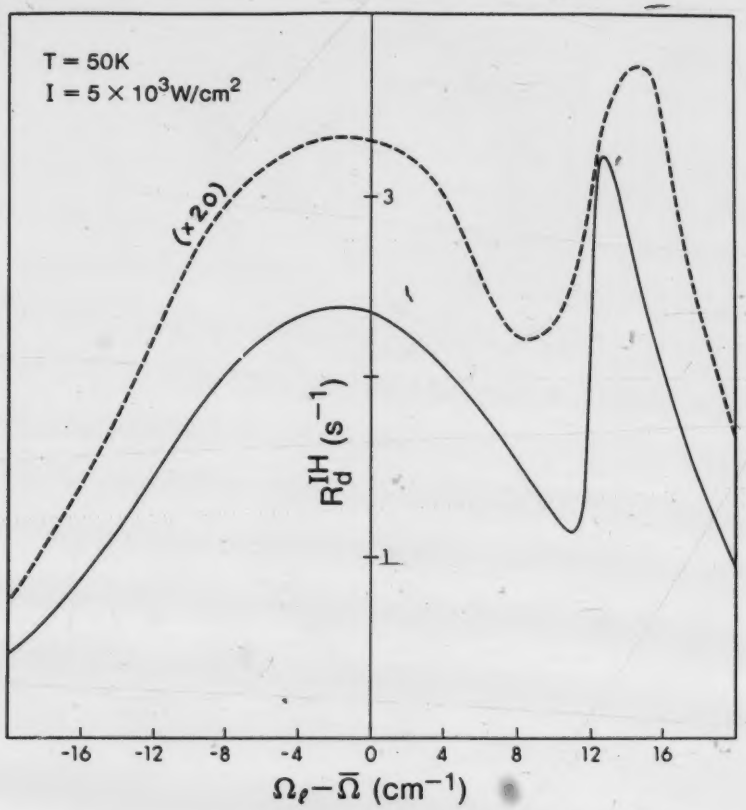

Fig.6.7. Photodesorption line shape as for Fig.6.6, but with slightly deeper surface potential V_0 = 23.05kJ/mole and γ^{-1} = 0.364Å. Solid and dashed lines are for Γ = 1cm^{-1} and Γ = 10cm^{-1}, respectively.

The double peak in the photodesorption spectrum occurs in the presence of larger homogeneous vibrational line widths too. This is shown by the dashed line in Fig. 6.7, corresponding to Γ=10 cm^{-1} and Γ_s=20 cm^{-1}. Note, however, that the widths of the surface bond energy levels, ε_j, have not been included here.

In summary, we find that the photodesorption spectrum from an adsorbate with predominantly inhomogeneously broadened vibrational levels should, in most cases, resemble the infrared absorption spec-

trum. However, striking differences can show up, such as a strong asymmetry of the photodesorption spectrum or even a double peak structure. These effects can be traced to the sudden switching off of effective elastic tunneling channels to desorption as the laser is detuned.

6.5 Discussion

The theoretical results presented in this section are now summarized, and experimental photodesorption and infrared absorption line shape measurements are then compared. For a homogeneous adsorbate with a harmonic vibrational mode, narrowing of the desorption spectrum is predicted, provided the intensity dependence of the desorption yield increases nonlinearly. This is typically the case when v^*, defined in Section 5.6 to be the lowest vibrational level degenerate with the gas phase continuum, is greater than one. An asymmetric desorption line shape may be expected for low temperatures of the order of the line width.

Vibrational anharmonicity alters the photodesorption spectrum markedly if $v^*>1$. If the anharmonic energy defect is less than the vibrational line width, $\Delta<\Gamma$, a redshifted and broadened desorption line shape is predicted. The redshift has a magnitude less than or equal to $(v^*-1)\Delta/2$. As shown in Fig.6.4, the broadening encountered here can cancel the narrowing effect noted above. However, for stronger anharmonicity or a narrower vibrational line, i.e. $\Delta>\Gamma$, a multiple peak photodesorption spectrum is found. The number of peaks will in general be less than or equal to v^*. These features result from the dependence of the desorption kinetics on higher vibrational excitations

$v \rightarrow v+1$ stimulated by the laser. Heterogeneity in the adsorbate is expected to round off this peak structure only slightly, unless desorption from distinctly different surface sites is observed simultaneously.

In contrast, photon-stimulated processes that probe only the lowest vibrational transition do not show the shifted or multiple peaked line shapes described above. Such processes include

(i) infrared absorption, which probes transitions $v=0 \rightarrow v'$ at low temperatures ($k_BT \ll \hbar\Omega$) and low intensity,

(ii) photodesorption by resonant heating, which depends mainly on the $v=0 \rightarrow 1$ transition, and has a frequency spectrum that is centred on the vibrational line, although different in shape,

(iii) photodesorption enhanced by rapid V-V coupling, where the laser need only excite the $v=0 \rightarrow 1$ step directly,[38]

and

(iv) photodesorption of weakly bound adsorbates with $v^*=1$.

The redshift or multiple peak structure of the desorption line shape appears to be a signature of the basic photodesorption mechanism proposed in Section 2 for adsorption systems where $v^*>1$. It is most likely to be observed at low temperatures where resonant heating effects are minimized and at very low coverages for which V-V coupling is weak.

In experiments by Heidberg et al.[22] on the $CH_3F/NaCl$ system, the width and peak position of the photodesorption line shape agree with that of the vibrational spectrum to within the experimental error (see Fig.1.2 and note that we must decompose the IR absorption from several adsorption sites[68]). For this adsorption system, a redshift of

$8cm^{-1}$ and a very slight (10%) overall broadening of the desorption spectrum is predicted in Fig.6.4 when a vibrational anharmonicity of $\Delta = 16cm^{-1}$ is accounted for. With V-V transfer processes included, as is realistic for multilayer coverage,the redshift of the desorption spectrum is reduced. Both these results are consistent with the experimental data. A conclusive determination of the specific photodesorption mechanism is not possible from the line shape arguments given here.

Photodesorption[27] and infrared absorption[94] have been recently measured for the CO/NaCℓ system as well. In this case V_o=0.7MΩ, so photodesorption involves only the $\bar{v}=0\rightarrow1$ transition. All photodesorption mechanisms discussed here predict that the photodesorption and infrared absorption spectra will coincide at moderate intensities for CO on NaCℓ. This is in fact observed experimentally.[27] Discussion of other photodesorption systems is included in the next Section.

7. Discussion and Outlook

7.1 Selective photodesorption versus resonant heating

In this paper, we have concentrated mainly on describing a selective, resonant photodesorption mechanism, applied extensively to the $CH_3F/NaCl$ adsorption system. Non-selective photodesorption, induced by resonant surface heating, has been discussed for the NH_3/Cu system too. Although only qualitative agreement between theory and experiment can be expected, it is illuminating to compare the selective and non-selective desorption channels above for other adsorption systems. The possibilities for observing selective photodesorption (of isotopes, for example) may then be better defined.

Resonant photodesorption has also been observed from the adsorption systems pyridine/KCl and CO/NaCl. The desorption rates for these systems, due to the selective mechanism described in Section 2, are calculated using the analytic approximation procedure described in Section 2.5.2. However, coherent two-phonon transition rates are included in the master equation and vibrational anharmonicity is taken into account in the laser-assisted transitions. Two-phonon rates $D_{j',j}$ are inserted in parallel with the one-phonon terms $P_{j',j}$ in equations (2.78), (2.83), (2.87), and (2.88). Note that including vibrational anharmonicity, described by the lineshape function (6.3) in the photon-assisted transition rate $L^{v'v}$, does not permit the simple substitution $L^{vv-1} = vL^{10}$ used previously. The full rate $L^{v'v}$ is easily incorporated into (2.87) and (2.88) in the calculation of the desorption rate.

The desorption kinetics calculated in this way for the pyridine/KCl system are shown in Fig.7.1, with V-V coupling neglected. Solid lines give the dependence of desorption rate on laser intensity in (i) the harmonic approximation $\Delta = 0$, and (ii) with an anharmonic shift $\Delta = 25\ cm^{-1}$ included. Since photodesorption for this system requires population of the third excited vibrational level $v = 3$, increased anharmonicity leads to considerably decreased desorption rates. However, lateral vibrational energy transfer may counteract this effect somewhat, as discussed in Section 4. At a laser intensity $I = 1 MW/cm^2$, the $\Delta = 0$ graph has a slope of 1.7, in close agreement with the non-linear intensity dependence $r_d \propto I^{1.8}$, observed by Chuang at this intensity.[24] However, it must be cautioned that the analogous desorption rate calculation based on only single phonon/photon transitions is shifted to considerably higher intensities, as shown by the broken line in Fig. 7.1. This clearly shows once again the importance of coherent multi-phonon transitions in the photodesorption process; this fact restricts us to a qualitative discussion of the kinetics.

The theoretical path to desorption for the pyridine/KCl system is quite complex. Except at very low intensities where thermal desorption dominates, photodesorption is initiated by incoherent, stepwise vibrational excitation to the $v = 3$ level. Phonon-assisted tunneling between bound states, i.e. $(i=0,v=3) \rightarrow (i,v=2) \rightarrow (i',v=1) \rightarrow (i'',v=0)$ where $0 < i < i' < i''$, gives up vibrational quanta to populate successively higher levels of translational motion in the surface bond. In fact, photodesorption occurs here from the very top levels (i") of the surface potential with the molecule in its vibrational ground state $v = 0$. These upper surface bond states are excited to population levels

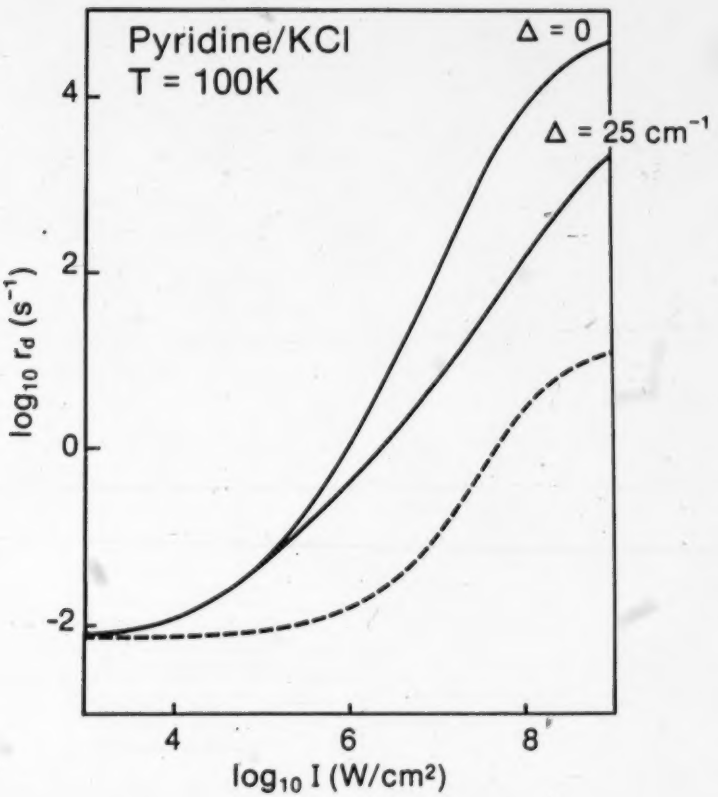

Fig.7.1. Desorption rate versus laser intensity for pyridine on KCl, for different choices of vibrational anharmonicity, Δ. The broken line is obtained by omitting coherent two-phonon transition processes. System parameters are listed in Table 7.1.

that are many orders of magnitude greater than their thermal equilibrium occupations, leading to the photodesorption effect.

Strongly non-linear desorption behaviour is predicted in Fig. 7.2 for CO from Cu(100). This adsorption system has both heat of adsorption and vibrational frequency given by roughly double that for pyridine on KCl. As a result, the desorption pathway described above applies here too. Note that coherent multiphoton effects have been ignored here, although they are not negligible for this system, as

Table 7.1. Adsorption system parameters. The effective charge defined in (2.92) is assumed to be Q = 1e for all systems below.

	$CH_3F/NaCl$[21,69]	NH_3/Cu[26]	Pyridine/KCl[24]	CO/NaCl[27]
$\Omega[cm^{-1}]$	970	3370	1032	2160
$E_d[K]$	2720	4090	3900	1960
$\Gamma[cm^{-1}]$	20	40	10	14
coverage	2	3.4	2	1
$t_L[nsec]$	200	6	100	160
$10^4 \cdot \sqrt{V_m/C_V\lambda}$ $[Km^2s^{1/2}J^{-1}]$	4	3	4	5.5
$\gamma^{-1}[Å]$	0.3	0.35	0.3	0.3

discussed in Section 5.4. Coherent effects are not expected to alter the power law intensity dependence of desorption on Fig.7.2, although an enhancement of the rates is anticipated. The lack of thermal effects in Fig.7.2 at 100K is due to the large heat of adsorption (≈ 0.7 eV) for this system. Furthermore, the theory predicts a triple-peaked photodesorption spectrum due to anharmonicity. The peaks are detuned to the red of the infrared absorption line by 0, 25, and 50cm^{-1}, corresponding to the transitions v=0 → 1, v=1 → 2, and v=2 → 3, respectively. Note that lateral vibrational energy transfer may affect this spectrum somewhat. Desorption experiments have not been carried out for CO on Cu, although the theory predicts (small) desorption yields comparable with those for the pyridine/KCl system.

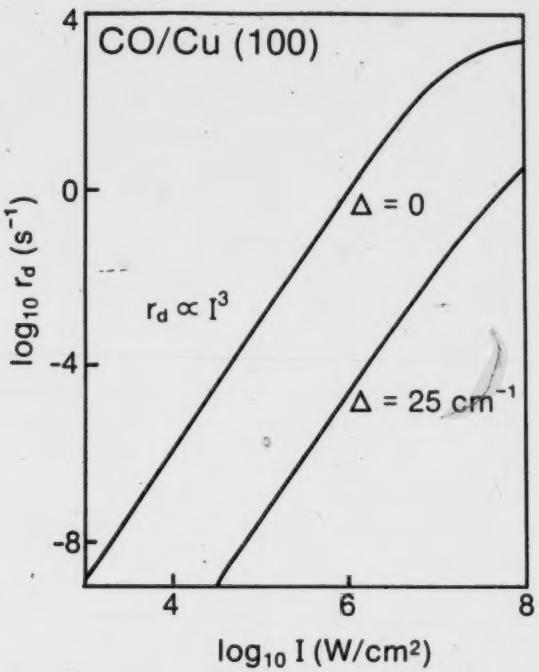

Fig.7.2. Desorption rate versus laser intensity for CO on Cu(100) at T = 100K. System parameters are V_0 = 8350K, γ^{-1} = 0.34Å, Ω = 2010cm^{-1}, Q= 0.5e, Γ = 5cm^{-1}.

Finally, we present calculations of the photodesorption kinetics of ^{13}CO from NaCl. For this weakly bound adsorption system the internal C-O vibrational frequency is larger than the adsorption energy, so population of the first excited vibrational level is sufficient to stimulate photodesorption by tunneling to the gas phase. However, vibrational relaxation by coupling to bound surface bond states of frustrated translational motion is cut off because of the large energy difference. In this situation, the one dimensional, single admolecule model used here cannot describe the dominant vibrational damping channel. An additional, phenomenological damping constant γ has been included in the calculations to represent vibrational coupling to librational/bending modes, to optical phonons, and to other adsorbed molec-

ules. In Fig.7.3, the desorption kinetics is shown for three possible values of the vibrational damping constant. In each case the desorp-

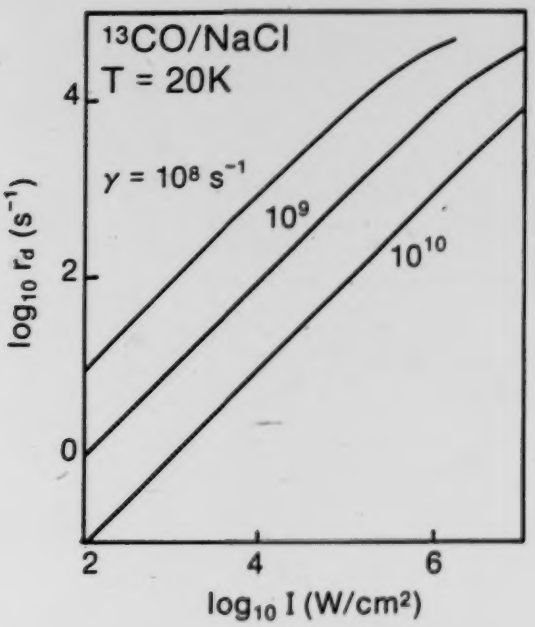

Fig.7.3. Desorption rate versus laser intensity for CO on NaCl, for different vibrational damping rates γ. System parameters are given in Table 7.1.

tion rate increases linearly with laser intensity.

We now compare the selective photodesorption mechanism with desorption by resonant surface heating, for the four experimentally studied adsorption systems CH_3F/NaCl, NH_3/Cu, pyridine/KCl, and CO/NaCl. (These systems are characterized by the parameters listed in Table 7.1) Specifically, the increase in surface temperature due to resonant heating during a laser pulse is calculated using equation (3.31) for sub-saturation conditions ($L \ll R$), as described in Section 3. The resulting elevated surface temperatures T_s are listed in Table 7.2 for laser intensities I = 1, 5, and 10 MW/cm^2.

Table 7.2. Selective photodesorption versus heating for the adsorption systems described in Table 7.1. Elevated surface temperatures T_s and enhanced thermal desorption rate $R_d(T_s)$ calculated for I = 1,5,and 10MW/cm², as explained in Section 3.2.2. Initial temperature is T_o. The ratio of selective to resonant-heating-induced desorption rates is $r_d/R_d(T_s)$.

	$CH_3F/NaCl$[21,69]	NH_3/Cu[26]	Pyridine/KCl[24]	CO/NaCl[27]
T_d[K]	75	90	95	20
I = 1MW/cm²				
T_s[K]	80	100	96	26
$R_d(T_s)$[s^{-1}]	$7\cdot10^{-1}$	$8\cdot10^{-4}$	$2\cdot10^{-13}$	<<1
$r_d/R_d(T_s)$	$9\cdot10^{3}$	$2\cdot10^{4}$	$6\cdot10^{2}$	>>1
I = 5MW/cm²				
T_s[K]	100	141	100	52
$R_d(T_s)$[s^{-1}]	$4\cdot10^{2}$	$6\cdot10^{1}$	$8\cdot10^{-3}$	3
$r_d/R_d(T_s)$	$3\cdot10^{2}$	1	$3\cdot10^{3}$	$1\cdot10^{4}$
I = 10MW/cm²				
T_s[K]	126	192	105	84
$R_d(T_s)$[s^{-1}]	$9\cdot10^{4}$	$9\cdot10^{4}$	$5\cdot10^{-2}$	$4\cdot10^{5}$
$r_d/R_d(T_s)$	4	$2\cdot10^{-3}$	$2\cdot10^{3}$	$1\cdot10^{-1}$

The thermal desorption rates $R_d(T_s)$ are thus enhanced, as calculated using a usual Arrhenius formula as given by (3.30). These rates may be compared with the rate of photodesorption r_d, due to the selective mechanism described in Section 2 and calculated at the initial substrate temperature.

In Table 7.2 the rate ratio $r_d/R_d(T_s)$ is listed. Large values indicate that selective desorption is predicted, while values less than

one show that resonant surface heating and enhanced (non-selective) thermal desorption dominates. By looking across the rows in Table 7.2, it is seen that the selective photodesorption mechanism is most dominant at lower intensity and especially in the $CH_3F/NaCl$ and pyridine/KCl systems, while resonant heating effects are most important in the NH_3/Cu case for $I \geq 5 MW/cm^2$. (This is to be compared with the lack of isotopic selectivity observed by Chuang et al.[26] in desorption yields of NH_3 and ND_3 from Cu.) Note that, at the higher intensities, NH_3 desorbs predominantly thermally after resonant heating, even though it is the most strongly bound adsorbate considered here. A high initial coverage and high initial temperature contribute to this effect.

As noted earlier, in Section 3, it is anticipated that the selective photodesorption mechanism and the resonant surface heating process may play very different roles in different adsorption systems. Due to theoretical limitations and poorly known experimental parameters (such as the dynamic dipole moment, the coverage, and the surface potential) accurate predictions on the selectivity of photodesorption are not yet available. However, we expect selectivity to be maximized at low coverage and low temperature on a dielectric substrate.

7.2 Conclusions

In summary, theories of resonant photodesorption have been presented, including (i) a selective desorption mechanism whereby vibrational energy tunnels directly into the frustrated translational mode of the adsorbed molecule, (ii) the effects of lateral vibrational energy

transfer in the adsorbate, and (iii) non-selective, enhanced thermal desorption due to resonant surface heating. The dependence of the desorption kinetics on laser intensity has been studied extensively. The selective desorption mechanism predicts that desorption rates follow a power law $r_d \propto I^{\alpha}$ which is often non-linear, in general agreement with experimental results. The degree of non-linearity depends both on the energetics of the system, i.e. the ratio of adsorption energy to the vibrational frequency, and on the efficiency of intramolecular coupling that pumps the molecular translational mode.

The photodesorption lineshape has also been studied theoretically in an effort to characterize the selective desorption mechanism. Narrowing of the desorption spectral shape is predicted at moderate intensities due to the non-linear power law behaviour noted above. An asymmetric spectrum may be expected at very low temperatures or for broad lines. Anharmonicity of the vibrational mode can cause either a red shift and line broadening or a multiple-peak spectrum, although strong V-V coupling is expected to wash out these effects. Inhomogeneous vibrational line broadening may also contribute additional structure to the photodesorption lineshape. Currently, experimental observations are consistent with, but unable to distinguish between these features. A major problem in comparing multi-layer photodesorption and infrared absorption lineshapes is that several different adsorption sites typically contribute to the infrared absorption signal even though desorption may occur predominantly from just one site.

Several notable theoretical problems remain as topics for further work, in an effort to make more accurate predictions of the desorption kinetics. Note that the theory developed here is restricted to pro-

viding qualitative predictions, mainly because (i) it is basically one dimensional, (ii) the perturbation theory for the phonon-assisted transitions does not appear to be converging, and (iii) the motion of the substrate surface atoms is assumed to be in thermal equilibrium at all times. To relax these shortcomings, a more detailed theory of photodesorption is required.

Specifically it would be desirable to consider a fully three-dimensional model of the adsorbed molecules; including librational, bending, and lateral translational motion would provide extra pathways for the conversion of vibrational energy to translational motion. Furthermore, the perturbation approach to the coupling between molecular motion and the motion of the surface atoms must also be reconsidered. By allowing the adsorbate-surface interaction to coherently induce nonequilibrium motion among the surface atoms[109] as well as in the adsorbate as considered thus far, (de)excitation of the adsorbate may be more accurately determined. Many body transitions in the adsorbate may also be important, particularly when unimolecular relaxation processes are inefficient. Finally, an explicit calculation of nonresonant V-V coupling processes involving both the translational and vibrational motion of a pair of adsorbed molecules and the surface motion of the substrate, remains missing from the discussion in Section 4. Such processes may reduce the selectivity of the photodesorption process somewhat. There are clearly many areas of theoretical work open for development.

A related field in which one can apply the kind of theoretical work discussed in this paper is the study of infrared absorption lineshapes,[61] which were treated phenomenologically here. The infrared

absorption spectrum is influenced by the same intra- and inter-molecular couplings and adsorbate-substrate interactions as those involved in the photodesorption process. The couplings noted above lead to both decay and pure dephasing processes, as included in the self-energy terms calculated in Section 5. In fact, insight gained from infrared absorption and photodesorption experiments may be combined to improve our understanding of these basic interactions.

The experimental aspects of photodesorption phenomena remain an active subject. For a theorist, an experimental determination of the absolute desorption yields as a function of coverage would be advantageous. (Such measurements are currently available for only the $CH_3F/NaCl$ system.) For example, in situ infrared absorption measurements before and after photodesorption would be helpful in this respect. While the heat of adsorption can be determined from equilibrium measurements, the range γ^{-1} of the surface potential is less easily obtained, and it is not known for most photodesorption systems. Vibrational spectroscopy of the molecule-surface bond by EELS or IR spectroscopy is one possibility. Alternatively, both the surface potential range and energy may be determined from flash thermal desorption measurements taken at different heating rates. To check the important vibrational damping rates calculated theoretically, recent picosecond relaxation measurements by Casassa, Heilweil, Stephenson, and Cavanagh[104] are valuable. With observed lifetimes of the order of 100 psec, they are promisingly in the same ball park as our calculations. Finally, photodesorption experiments involving co-adsorbates such as isotopes or including a thermal monitor molecule (i.e. a molecule which physisorbs with heat of adsorption less than or equal

to that of the infrared-active species) provide direct evidence on the selectivity of the desorption mechanism. (This has been done in reference 26.)

It is clear that the kinetics of photodesorption can show considerable structure which depends on the microscopic transition rate scales operative in the adsorbate. Although the underlying desorption mechanism is not yet precisely understood, selective and non-selective processes are expected to compete. Which mechanisms dominate in a given adsorption system remains the object of future studies.

References

1. (a) A. Clark, The Theory of Adsorption and Catalysis, Academic Press, New York, 1970.
   (b) A. M. Bradshaw, Surf. Sci. 80, 215 (1979).
2. T. J. Chuang, Surf. Sci. Reports 3, 1 (1983); J. Vac. Sci. Technol. 21, 798 (1982).
3. J.-t. Lin, W. C. Murphy, and T. F. George, I&EC Product Research & Development 23, 334 (1984).
4. H. J. Kreuzer and Z. W. Gortel, Physisorption Kinetics, Springer-Verlag, Berlin, 1986.
5. L. W. Bruch, Surf. Sci. 125, 194 (1983).
6. J. R. Smith, ed., Theory of Chemisorption, Springer-Verlag, Berlin, 1980.
7. D. Menzel in R. Vanselow, ed., Chemistry and Physics of Solid Surfaces IV, Springer-Verlag, Berlin, 1982, p. 389; and in R. Gomer, ed., Interactions on Metal Surfaces, Springer-Verlag, Berlin, 1975, p. 101.
8. S. Glasstone, K. J. Laider and H. Eyring, The Theory of Rate Processes, McGraw-Hill, New York, 1941; Ch. 4.
9. Examples of classical theories are:
   (a) P. J. Pagni and J. C. Keck, J. Chem. Phys. 58, 1162 (1973); P. J. Pagni, J. Chem. Phys. 58, 2940 (1973).
   (b) A. Redondo, Y. Zeiri, and W. A. Goddard III, Surf. Sci. 136, 41 (1984).
   (c) J. Czarniecki and M. Jaroniec, Surf. Sci. Reports 3, 301 (1983).
10. (a) J. E. Lennard-Jones and C. Strachan, Proc. Roy. Soc. (London) A 150, 422 (1935).
    (b) C. Strachan, Proc. Roy. Soc. (London) A 150, 456 (1935).
    (c) J. E. Lennard-Jones and A. F. Devonshire, Proc. Roy. Soc. (London) A 156, 29 (1936).
11. B. J. Garrison, D. J. Diestler, and S. A. Adelman, J. Chem. Phys. 67, 4317 (1977).

12. (a) B. Bendow and S.-C. Ying, Phys. Rev. B **7**, 622 (1973).
(b) S.-C. Ying and B. Bendow, Phys. Rev. B **7**, 637 (1973).

13. (a) S. Efrima, K. F. Freed, C. Jedrzejek, and H. Metiu, Chem. Phys. Letters **74**, 43 (1980).
(b) C. Jedrzejek, K. F. Freed, S. Efrima, and H. Metiu, Chem. Phys. Letters **79**, 227 (1981).
(c) S. Efrima, C. Jedrzejek, K. F. Freed, E. Hood, and H. Metiu, J. Chem. Phys. **79**, 2436 (1983).

14. Z. W. Gortel, H. J. Kreuzer, and R. Teshima, Phys. Rev. B **22**, 5655 (1980). (References to a series of earlier papers are given here.)

15. (a) D. Menzel, J. Vac. Sci. Technol. **20**, 538 (1982).
(b) D. Lichtman and Y. Shapira, CRC Critical Rev. Solid State Mater. Sci. **8**, 93 (1978).

16. This process has been modeled theoretically by R. R. Lucchese and J. C. Tully, J. Chem. Phys. **81**, 6313 (1984).

17. (a) G. Wedler and H. Ruhmann, Surf. Sci. **121**, 464 (1982).
(b) R. Viswanathan, D. R. Burgess, Jr., P. C. Stair, and E. Weitz, J. Vac. Sci. Technol. **20**, 605 (1982).
(c) J. Hussla and R. Viswanathan, preprint.

18. (a) J.-t. Lin and T. F. George, Chem. Phys. Letters **66**, 5 (1979).
(b) A. C. Beri and T. F. George, J. Chem. Phys. **78**, 4288 (1983).
(c) A. C. Beri and T. F. George, J. Chem. Phys. **83**, 2482 (1985).

19. (a) C. Jedrzejek, K. F. Freed, S. Efrima, and H. Metiu, Surf. Sci. **109**, 191 (1981).
(b) D. J. Diestler and M. E. Riley, Surf. Sci. **150**, L101 (1985).

20. R. V. Ambartzumian and V. S. Letokhov, in C. B. Moore, ed., Chemical and Biochemical Applications of Lasers, Vol. 3, Academic Press, 1977, p. 167.

21. J. Heidberg, H. Stein, E. Riehl, and A. Nestmann, Z. Phys. Chem. Neue Folge **121**, 145 (1980).

22. J. Heidberg, H. Stein, and E. Riehl, Phys. Rev. Lett. **49**, 666 (1982).

23. T. J. Chuang and H. Seki, Phys. Rev. Lett. **49**, 382 (1982).

24. T. J. Chuang, J. Chem. Phys. **76**, 3828 (1982).

25. H. Seki and T. J. Chuang, Solid State Commun. **44**, 473 (1982).
26. T. J. Chuang, H. Seki, and I. Hussla, Surf. Sci. **158**, 525 (1985).
27. J. Heidberg, H. Stein, and H. Weiss, preprint.
28. J. S. Mercier, Ph.D. Thesis, Cornell University, Ithaca, N.Y., 1983.
29. M. Mashni and P. Hess, Chem. Phys. Letters **77**, 541 (1981).
30. H. J. Kreuzer and D. N. Lowy, Chem. Phys. Letters **78**, 50 (1981).
31. (a) D. Lucas and G. E. Ewing, Chem. Phys. **58**, 385 (1981).
(b) G. E. Ewing, J. Chem. Phys. **72**, 2096 (1980).
32. T. F. George, J. Lin, A. C. Beri, and W. C. Murphy, Prog. Surf. Sci. **16**, 139 (1984).
33. (a) J.-t. Lin and T. F. George, J. Phys. Chem. **84**, 2957 (1980).
(b) J.-t. Lin and T. F. George, J. Chem. Phys. **78**, 5197 (1983).
(c) J.-t. Lin and T. F. George, Phys. Rev. B **28**, 76 (1983).
34. X.-Y. Huang, T. F. George, J.-M. Yuan, and L. M. Narducci, J. Phys. Chem. **88**, 5772 (1984).
35. (a) M. P. Casassa, F. G. Celii, K. C. Janda, J. Chem. Phys. **76**, 5295 (1982).
(b) F. G. Celii, M. P. Casassa, and K. C. Janda, Surf. Sci. **141**, 169 (1984).
36. B. Fain and S. H. Lin, Surf. Sci. **147**, 497 (1984).
37. G. S. Wu, B. Fain, A. R. Ziv, and S. H. Lin, Surf. Sci. **147**, 537 (1984).
38. B. Fain and. S. H. Lin, Chem. Phys. Letters **114**, 497 (1985).
39. Z. W. Gortel, H. J. Kreuzer, P. Piercy, and R. Teshima, Phys. Rev. B **27**, 5066 (1983).
40. E. Goldys, Z. W. Gortel, and H. J. Kreuzer, Surf. Sci. **116**, 33 (1982).
41. J. D. Jackson, Classical Electrodynamics (2nd ed.), John Wiley, New York, 1975.
42. P. J. Feibelman, Progr. Surf. Sci. **12**, 287 (1982).
43. K. L. Kliewer, Surf. Sci. **101**, 57 (1980).
44. J. R. Schrieffer, Theory of Superconductivity, W. A. Benjamin, New York, 1964, p. 206.
45. T. Maniv and H. Metiu, Phys. Rev. B **22**, 4731 (1980).
46. T. Maniv and H. Metiu, J. Chem. Phys. **76**, 2697 (1982).

47. A. Hartstein, J. R. Kirtley,and J. C. Tsang, Phys. Rev. Lett. 45, 201 (1980).

48. (a) A. Nitzan and L. E. Brus, J. Chem. Phys. 74, 5321 (1981); J. Chem. Phys. 75, 2205 (1981).
(b) H. Ueba and S. Ichimura, Phys. Stat. Solid (b) 101, K161 (1982); Surf. Sci. 118, L273 (1982).
(c) H. Metiu and P. Das, Ann. Rev. Phys. Chem. 35, 507 (1984).

49. S. L. Adler, Phys. Rev. 126, 413 (1962).

50. H. Haken, Quantum Field Theory of Solids, North-Holland, Amsterdam, 1976.

51. H. Ezawa, Ann. Phys. 67, 438 (1971).

52. See ref. 4; also, L. Dobrzynski and B. Djafari-Rouhani in R. Candano, J.-M. Gilles, and A. A. Lucas, ed., Vibrations at Surfaces, Plenum Press, New York, 1982, p. 1.

53. In ref. 40, an effective Debye temperature is deduced that is about 0.65 to 0.8 times the bulk Debye temperature.

54. H. Landes, G. Wedler, Z. W. Gortel, and H. J. Kreuzer, Phys. Rev. B 33 (March 15, 1986).

55. H. J. Kreuzer, Nonequilibrium Thermodynamics and Its Statistical Foundations, Clarendon Press, Oxford, 1981. See Ch. 10.

56. B. Fain, Theory of Rate Processes in Condensed Media, Springer-Verlag, Berlin, 1980.

57. W. H. Louisell, Quantum Statistical Properties of Radiation, John Wiley & Sons, New York, 1973.

58. A. L. Fetter and J. D. Walecka, Quantum Theory of Many-Particle Systems, McGraw-Hill, New York, 1971, Ch. 3.

59. M. Sargent III, M. O. Scully, and W. E. Lamb, Jr., Laser Physics , Addison-Wesley, Reading, MA, 1974.

60. P. Piercy, M.Sc. Thesis, University of Alberta, Edmonton, Alberta, 1983.

61. (a) F. M. Hoffmann, Surf. Sci. Reports 3, 107 (1983).
(b) P. Hollins and J. Pritchard, Prog. Surf. Sci. 19, 275 (1985).

62. (a) B. J. J. Persson and R. Ryberg, Phys. Rev. Lett. 54, 2119 (1985).

(b) J. C. Tully, Y. J. Chabal, K. Raghavachari, J. M. Bowman, and R. R. Lucchese, Phys. Rev. B 31, 1184 (1985).

63. Z. W. Gortel, H. J. Kreuzer, R. Teshima, and L. A. Turski, Phys. Rev. B 24, 4456 (1981).

64. H. J. Kreuzer and Z. W. Gortel, Phys. Rev. B 29, 6926 (1984).

65. In this case, one must still solve a master equation for $n_j(t)$; see ref. 64.

66. T. L. Hill, Thermodynamics for Chemists and Biologists, Addison-Wesley, Reading, MA, 1968.

67. T. L. Hill, J. Theoret. Biol. 10, 442 (1966).

68. J. Heidberg, I. Hussla, and Z. Szilagyi, J. El. Spectr. Rel. Phenom. 30, 53 (1983).

69. J. Heidberg, H. Stein, Z. Szilagyi, and H. Weiss, Surf. Sci. 158, 553 (1985).

70. T. J. Chuang, H. Coufal, and F. Träger, J. Vac. Sci. Technol. A1, 1236 (1983).

71. P. Dumas, R. G. Tobin, and P. L. Richards, preprint.

72. Z. W. Gortel, H. J. Kreuzer, P. Piercy, and R. Teshima, Phys. Rev. B 28, 2119 (1983).

73. I. Hussla, H. Seki, T. J. Chuang, Z. W. Gortel, H. J. Kreuzer, and P. Piercy, Phys. Rev. B 32, 3489 (1985).

74. B. N. J. Persson and M. Persson, Surf. Sci. 97, 609 (1980).

75. L. E. Brus, J. Chem. Phys. 73, 940 (1980).

76. B. N. J. Persson and M. Persson, Solid State Commun. 36, 175 (1980).

77. R. Ryberg, Phys. Rev. B 32, 2671 (1985).

78. H. S. Carslaw, Mathematical Theory of the Conduction of Heat in Solids, MacMillan, London, 1921.

79. A. N. Tikhonov and A. A. Samarkii, Equations of Mathematical Physics, Pergamon, New York, 1963.

80. Y. S. Touloukian et. al., ed., Thermophysical Properties of Matter, Plenum, New York, 1970.

81. (a) F. Legay in C. B. Moore, ed., Chemical and Biochemical Applications of Lasers, Vol. 2, Academic Press, New York, 1977, p. 43.

(b) V. E. Bondybey and L. E. Brus, Adv. Chem. Phys. **41**, 269 (1980).

82. H. Dubost and R. Charneau, Chem. Phys. **12**, 407 (1976).
83. N. Legay-Sommaire and F. Legay, IEEE J. Quantum El. **16**, 308 (1980).
84. J. Manz, Chem. Phys. **24**, 51 (1977).
85. A. Blumen, S. H. Lin, and J. Manz, J. Chem. Phys. **69**, 881 (1978).
86. Enhanced vibrational excitation in the gas phase was predicted earlier: C. E. Trainor, J. W. Rich, and R. G. Rehm, J. Chem. Phys. **48**, 1798 (1968).
87. G. D. Mahan and A. A. Lucas, J. Chem. Phys. **68**, 1344 (1978).
88. B. N. J. Persson and R. Ryberg, Phys. Rev. B **24**, 6954 (1981).
89. J. Heidberg, H. Stein, and E. Reihl, in R. Caudano, J.-M. Gilles, and A. A. Lucas, ed., Vibrations at Surfaces, Plenum Press, New York, 1982, p. 17.
90. A. Messiah, Quantum Mechanics, John Wiley & Sons, New York, 1963, Vol. 2, Ch. 17.4.
91. J. W. Gadzuk and A. C. Luntz, Surf. Sci. **144**, 429 (1984).
92. N. G. van Kampen, Stochastic Processes in Physics and Chemistry, North-Holland, Amsterdam, 1981. See Ch. 6.
93. J. Callaway, Quantum Theory of the Solid State, Academic Press, New York, 1974.
94. J. Heidberg, H. Stein, and I. Hussla, Surf. Sci. **162**, 470 (1985).
95. V. A. Apkarian and E. Weitz, J. Chem. Phys. **76**, 5796 (1982).
96. (a) S. M. Freuend et. al., J. Mol. Spectrosc. **52**, 38 (1974).
(b) S. Stokes and A. B. F. Duncan, J. Amer. Chem. Soc. **80**, 6177 (1958).
97. Z. W. Gortel, H. J. Kreuzer, P. Piercy, and R. Teshima, Surf. Sci. **166**, L119 (1986).
98. See ref. 90, Ch. 19.
99. Z. W. Gortel, H. J. Kreuzer, and R. Teshima, Phys. Rev. B **22**, 512 (1980).
100. H. Umezawa, H. Matsumoto, and M. Tachiki, Thermo Field Dynamics and Condensed States, North-Holland, Amsterdam, 1982.
101. See ref.58, Ch. 7.
102. P. A. M. Dirac, Principles of Quantum Mechanics, Clarendon Press,

Oxford, 1930.

103. W. Heitler, Quantum Theory of Radiation, 3rd ed., Clarendon Press, Oxford, 1954.

104. M. P. Casassa, E. J. Heilweil, J. C. Stephensen, and R. R. Cavanagh, J. Vac. Sci. Technol. A **3**, 1655 (1985).

105. S. H. Lin, Y. Fujimura, H. J. Neusser, and E. W. Schlag, Multiphoton Spectroscopy of Molecules, Academic Press, London, 1984. See Ch. 2,5.

106. (a) D. C. Langreth, Phys. Rev. Lett. **54**, 126 (1985).
(b) H. Metiu and W. E. Palke, J. Chem. Phys. **69**, 2574 (1978).

107. C. Jedrzejek, J. Vac. Sci. Technol. (in press).

108. Z. W. Gortel, P. Piercy, R. Teshima, and H. J. Kreuzer, Surf. Sci. **165**, L12 (1986).

109. (a) B. Fain and. S. H. Lin, Physica A **128**, 164 (1984).
(b) B. Fain, Chem. Phys. Letters **118**, 283 (1985).

Appendix A - Normal Modes of the Radiation Field

The normal modes of the electromagnetic field in the presence of a semi-infinite dielectric ($z < 0$) are given by

$$U_{k\beta}(x) = \frac{1}{2\pi}\, e^{iK\cdot R}\, f_{K\zeta}{}^{\beta}(x) \tag{A.1}$$

where

$$f_{K\zeta}{}^{s}(R,z) = N^{s}\, n\times\hat{K} \begin{cases} \left[e^{i\zeta z} + \frac{1-n_r a}{1+n_r a}\, e^{-i\zeta z}\right]; & z > 0 \\ \frac{2}{(1+n_r a)}\, e^{-ibz}; & z < 0 \end{cases} \tag{A.2}$$

and

$$f_{K\zeta}{}^{p}(R,z) = N^{p} \begin{cases} Kn\left[e^{i\zeta z} + \frac{n_r a}{n_r + a}\, e^{-i\zeta z}\right] - \zeta\hat{K}\left[e^{i\zeta z} - \frac{n_r - a}{n_r + a}\, e^{-i\zeta z}\right]; & z>0 \\ \frac{2}{n_r(n_r+a)}\,(Kn+b\hat{K})e^{ibz}; & z<0 \end{cases} \tag{A.3}$$

for polarizations β = s and p, respectively. Here $x=R+zn$ and $k=K+\zeta n$ with $K = K\hat{K}$ and R parallel to the surface, and n a unit normal vector pointing outwards. Note that $\zeta < 0$ to describe laser radiation incident from the vacuum side. Furthermore, we define

$$a = -\frac{1}{\zeta}\sqrt{K^2(1-n_r^{-2})+\zeta^2} \text{ and } b = \sqrt{K^2(n_r^2-1)+n_r^2\zeta^2} \quad .$$

The normalization constants, N^S and N^P, are determined by the orthogonality condition (2.20).

Appendix B – Morse Potential Matrix Elements

Formula (2.55) may be evaluated, to a good approximation, by keeping just the lowest non-zero term in the sum over ℓ. This term corresponds to $\ell = |v'-v|$, except when $j' = j$ and $v' = v$; in the latter case, the $\ell = 2$ term is required. In this approximation, straightforward evaluation of the matrix elements of the Morse surface potential and harmonic vibrational mode leads to[60]

$$V_{j'v',jv}^{(1)} = -2V_0\gamma \left[\frac{v_>!}{v_<!}\right]^{1/2} \frac{a^{|v-v'|/2}}{|v-v'|!}\, G_{j'v',jv} \qquad (B.1)$$

where

$$G_{j'v',jv} = \begin{cases} I(|v-v'|,j',j) \; ; \; j'v' \neq jv \\ \frac{1}{2}\, a(2v+1)I(2,j,j) \; ; \; j'v' = jv \end{cases} . \qquad (B.2)$$

Here, we define

$$a = \frac{m_2/m_1}{r\delta_v} \qquad (B.3)$$

and let $v_>(v_<)$ be the maximum (minimum) of v,v'. The function $I(\ell,j',j)$ in (B.2) is given explicitly in equation (5.54).

In Chapter 5, the matrix element of the second derivative of the Morse potential is needed. In fact, the n^{th} derivative matrix element is given, for $n \geq 2$, by

$$V_{j'v'jv}^{(n)} = 2V_o(-\gamma)^n \left[\frac{v_>!}{v_<!}\right]^{1/2} \frac{a^{|v-v'|/2}}{|v-v'|!} I(|v-v'|+n-1,j',j) \ . \qquad (B.4)$$

For completeness, we also define below the derivative-coupling matrix element of the interaction of the laser with molecular vibrations as

$$\xi_{jv,j'v'} = \langle jv \left| \frac{\partial}{\partial \xi} \right| j'v' \rangle$$

$$= \left(\frac{\mu\Omega}{2\hbar}\right)^{1/2} \delta_{jj'}(\sqrt{v+1}\ \delta_{v',v+1} - \sqrt{v}\ \delta_{v',v-1}) \ . \qquad (B.5)$$

Appendix C - V-V Coupling Rate Matrix Terms

The many-body master equation (4.11) for a monolayer adsorbate has off-diagonal transition rate elements (4.12) given by

$$R(i,v,i',v') = \sum_{n=1}^{N} \delta_{i_1 i_1'} \delta_{v_1 v_1'} \cdots R_{i_n i_n'}{}^{v_n v_n'} \cdots \delta_{i_N i_N'} \delta_{v_N v_N'} \tag{C.1}$$

and

$$V(i,v,i',v') = \delta_{ii'} \sum_{m \neq n} \delta_{v_1 v_1'} \cdots V_{v_n v_n'}{}^{v_m v_m'} \cdots \delta_{v_N v_N'} \tag{C.2}$$

for $i,v \neq i',v'$. The quantities between the dots above replace the delta-functions of the respective indices. The rates in (C.1) include single-molecule transitions, $(i_n,v_n) \to (i_n',v_n')$ for the n^{th} molecule, which occurs independently of the state of the rest of the adsorbate as described in Chapter 2. The transition rate given in (C.2) describes vibrational transfer between pairs of molecules. The transition rate for a given pair (m,n) is given by

$$V_{v_n v_n'}{}^{v_m v_m'}(r_m - r_n) = \delta_{v_m, v_m'+1}\, \delta_{v_n, v_n'-1}\, D_{v_m' v_n'}$$

$$+ \delta_{v_m, v_m'-1}\, \delta_{v_n, v_n'+1}\, D_{v_n' v_m'} \tag{C.4}$$

where $D_{vv'}$ is given by (4.5) with $a_o = |r_m - r_n|$.

The diagonal elements of the rate matrix (4.11) are defined by the condition

$$0 = \sum_{iv} \dot{n}(iv,t) \qquad (C.5)$$

which describes overall conservation of molecules in the gas and adsorbed phases. Combining equations (C.1) to (C.5), it is checked that the diagonal terms are correctly included by making the replacements

$$R_{ii'}^{vv'} \rightarrow R_{ii'}^{vv'} - \delta_{ii'}\,\delta_{vv'} \sum_{j\neq i} \sum_{u\neq v} R_{ji}^{uv} \qquad (C.6)$$

and

$$V_{uu'}^{vv'}(r-r') \rightarrow V_{uu'}^{vv'}(r-r') - \delta_{vv'}\,\delta_{uu'} \sum_{v''\neq v} \sum_{u''\neq u} V_{u''u}^{v''v}(r-r') \qquad (C.7)$$

in (C.1) and (C.2), respectively. This defines the rate terms appearing in equations (4.11)and (4.14).

Appendix D - Diagram rules and Derivation of (5.38)

The diagram rules for evaluation of amplitudes (5.21) and (5.22), based on the expansion (2.35), are[58]

1. Draw all distinct connected diagrams from the internal and external lines and vertices discussed below. Count a factor of 2! for each two-phonon vertex. Note that no molecule-line loops are permitted. Vertices of the types listed in Fig. 5.1 are allowed. External and internal molecule, photon, and phonon lines are included. Molecular lines are labelled $i\omega$, while external photon and phonon lines are labelled k and p, respectively. Internal photon and phonon lines are labelled by frequency ω only. (The label i is the double index jv for a molecular state while k and p include both wavevector and polarization.)
2. External molecular lines are assigned the propagator

$$\frac{1}{2\pi} S_i^{in/out}(\omega) .$$

Note that equation (5.33c) is used in the amplitude (5.21), while (5.33d) is used in calculating (5.22). For internal molecular lines, use the propagator (5.33a) instead in the above.

3. External photon and phonon lines contribute the functions

$$f_k = \left(\frac{N}{2\epsilon_0}\right)^{1/2} \Omega_k^{-1/2}\, \mathbf{n}\cdot\overline{U_k(0)}\, (1+n_k^{\ell})^{1/2} \qquad (D.1)$$

and

$$f_p = \left(\frac{\mathcal{N}}{2M_S N_S}\right)^{1/2} \frac{\varepsilon_p}{\omega_p^{1/2}} \left(1+n_p^S\right)^{1/2} , \tag{D.2}$$

respectively, to the transition amplitude. For the corresponding tilded particles, $\tilde{R}$ and $\tilde{\beta}$, one simply drops the 1 in the brackets. Internal photon and phonon lines contribute $\frac{1}{2\pi} E(\omega)$ and $\frac{1}{2\pi} D(\omega)$, respectively, where

$$D(\omega) = 2i \frac{\mathcal{N}}{2M_S N_S} \sum_p \varepsilon_p^2 \left[\frac{1+n_p^S}{\omega^2-\omega_p^2+i\gamma} + \frac{n_p^S}{\omega^2-\omega_p^2+i\gamma}\right] \tag{D.3}$$

and

$$E(\omega) = 2i \frac{\mathcal{N}}{2\varepsilon_0} \sum_k \left|n\cdot U_k(0)\right|^2 \left[\frac{1+n_k^\ell}{\omega^2-\Omega_k^2-i\gamma} + \frac{n_k^\ell}{\omega^2-\Omega_k^2+i\gamma}\right] . \tag{D.4}$$

4. Each vertex contributes

$$\frac{1}{i\mathcal{N}} \langle i_1|\theta(y)|i_2\rangle \, 2\pi\delta(\omega_1 + \ldots - \omega_2 - \ldots) ,$$

where the frequencies of incoming lines are negative and those of outgoing lines are positive. Here, the indices of the incoming and outgoing molecule lines are i_2 and i_1, respectively. The interaction functions $\theta(y)$ are listed below in Table D.1.

5. Sum over all internal molecular line indices (i) and integrate

Table D.1. Interaction Hamiltonian

Vertex	Interaction Hamiltonian	$\theta(y)$
one-photon	H_ℓ	$-i\mathcal{M}\frac{Q}{\mu}\frac{\partial}{\partial \xi}$
n-phonon	$H^{(n)}$	$\frac{(-1)^n}{n!}\frac{\partial^n}{\partial x^n} V(x = \frac{\mu}{m_1}\xi)$
residual	H_{res}	$V(x = \frac{\mu}{m_1}\xi) - V(x - \frac{\mu}{m_1}\xi^\circ)$

over the frequencies (ω) of all internal lines and all external molecular lines, noting that the number of integrations is given by the number of internal lines minus the number of vertices plus one.

Using these diagram rules to construct Dyson's equations, approximating full internal molecular propagators by (5.37), and taking external molecule lines to be bare (5.33) leads to the general transition amplitudes arising from n irreducible vertices

$$A'_{fi}{}^{(n)} = \sum_{j_1 \cdots j_{n-1}} V_{fj_1\omega_1}\, G_{j_1}{}^r(\varepsilon_f+\omega_1) V_{j_1 j_2 \omega_2}\, G_{j_2}{}^r(\varepsilon_f+\omega_1+\omega_2) \cdots V_{j_{n-1} i \omega_n}\,, \tag{D.5}$$

and

$$A_{fi}^{(n)} = A'_{fi}^{(n)}\, S_i(\varepsilon_f+\omega_1+\ldots+\omega_n) \qquad (D.6)$$

contributing to equations (5.22) and (5.21), respectively. Here, molecular indices are $f, j_1, \ldots j_{n-1}, i$ and $\hbar\omega_\alpha$ is the energy given up by the molecule at the α^{th} vertex by phonon or photon absorption/emission. The irreducible vertex functions $V_{jj'\omega}$ are approximated by their bare

Table D.2. Vertex Functions

Vertex	Vertex Function
One-photon emission	$V_{ijk} = -\frac{Q}{\mu}\left(\frac{\hbar}{2\varepsilon_0}\right)^{1/2} \xi_{ij}\, \Omega_k^{\omega_1/2}\, \mathbf{n}\cdot\mathbf{U}_k(0)\, (1+n_k^{\ell})^{1/2}$
One-phonon emission	$V_{ijp} = -\frac{1}{i\hbar}\, V_{ij}^{(1)}\left(\frac{\hbar}{2M_S N_S}\right)^{1/2} \frac{\varepsilon_p}{\omega_p^{1/2}}\, (1+n_p^{s})^{1/2}$
Two-phonon emission	$V_{ijp_1p_2} = \frac{1}{2i\hbar}\, V_{ij}^{(2)}\, \frac{\hbar}{2M_S N_S}\, \frac{\varepsilon_{p_1}\varepsilon_{p_2}}{(\omega_{p_1}\omega_{p_2})^{1/2}} (1+n_{p_1}^{s})^{1/2}\, (1+n_{p_2}^{s})^{1/2}$
Residual	$V_{ij} = \frac{1}{i\hbar} \langle i \left\| V(x - \frac{\mu}{m_1}\xi) - V(x - \frac{\mu}{m_1}\xi^0) \right\| j\rangle$

counterparts given in Table D.2.

The matrix elements $V_{ij}^{(1)}$, $V_{ij}^{(2)}$, and ξ_{ij} are given by equations (B.1), (B.4), and (B.5), respectively. Phonon/photon absorption is obtained by replacing the appropriate $(1+n)^{1/2}$ factor with $n^{1/2}$ above, and including the corresponding negative frequency contribution in (D.5) and (D.6).

To derive the rate formula given in (5.38), note that using equations (D.5) and (D.6) in (5.22) and (5.21) implies that

$$\text{equation (5.21)} = \text{equation (5.22)} * S_i(\varepsilon_f + \omega_1 + \ldots + \omega_n) \ . \qquad \text{(D.7)}$$

Substituting (D.7) into (5.8) and using (5.33a) gives (5.38).

Appendix E – Components of Equation (5.73).

The matrix elements of the Morse surface potential and harmonic vibrational oscillator are contained in the functions $H^{(n)}$ that appear in (5.73) and are defined below.

$$H_{j'uj'u'}(1) = \binom{u}{v}^{1/2} \binom{u'}{v}^{1/2} \frac{a^{(|u-v|+|u'-v|)/2}}{|u-v|!|u'-v|!} G_{j'ujv} G_{j'u'jv}$$
$$*(\sqrt{v'+1}\,\delta_{u,v'+1} - \sqrt{v'}\,\delta_{u,v'-1})(\sqrt{v'+1}\,\delta_{u',v'+1} - \sqrt{v'}\,\delta_{u',v'-1})$$

$$H_{ju'u'}(2) = \binom{u}{v'}^{1/2} \binom{u'}{v'}^{1/2} \frac{a^{(|v'-u|+|v'-u'|)/2}}{|v'-u|!|v'-u'|!} G_{j'v'ju} G_{j'v'ju'}$$
$$* (\sqrt{v+1}\,\delta_{u,v+1} - \sqrt{v}\,\delta_{u,v-1})(\sqrt{v+1}\,\delta_{u',v+1} - \sqrt{v}\,\delta_{u',v-1})$$

$$H_{j'uju'}(3) = -2\binom{u}{v}^{1/2} \binom{u'}{v'}^{1/2} \frac{a^{(|u-v|+|v'-u'|)/2}}{|u-v|!|v'-u'|!} G_{j'ujv} G_{j'v'ju'}$$
$$* (\sqrt{v'+1}\,\delta_{u,v'+1} - \sqrt{v'}\,\delta_{u,v'-1})(\sqrt{v+1}\,\delta_{u',v+1} - \sqrt{v}\,\delta_{u',v-1})$$

where

$$\binom{v}{v'} = \frac{v_>!}{v_<!}$$

with $v_>(v_<)$ equal to the maximum (minimum) of (v,v'). $G_{jvj'v'}$ is given in (B.2).